2015-10-02

Wind Flow over Small Buildings for Renewable Energy Applications

REZA, MD. SHAMIM

UNIVERSITY OF CALGARY

Wind Flow over Small Buildings for Renewable Energy Applications

by

Md Shamim Reza

A THESIS

SUBMITTED TO THE FACULTY OF GRADUATE STUDIES

IN PARTIAL FULFILMENT OF THE REQUIREMENTS FOR THE

DEGREE OF MASTER OF SCIENCE

GRADUATE PROGRAM IN MECHANICAL AND MANUFACTURING ENGINEERING

CALGARY, ALBERTA

SEPTEMBER, 2015

Abstract

The wind flow over three buildings is simulated and presented for different wind directions using the standard $k-\varepsilon$ turbulence model. The main purposes are, first, to predict the minimum wind load regions on roof mounted photovoltaic modules for reducing the cost of installing them on a mono-slope roof building. Secondly, to predict the flow fields along the gable of a tent roof building for analysis of the performance of a transverse axis wind turbine along the gable. The results for the cube simulation are compared with the experimental and other CFD results for validating the CFD. The present research provides the best locations for roof mounted PV modules. These results were significantly lower in magnitude than the NBCC values. The flow fields over the tent roof building were predicted and consistent with the field data. The flow over buildings was highly dependent on the building orientation and geometry.

Acknowledgements

It is not possible to acknowledge everyone who has contributed to this research, but here I acknowledge several in particular. I would like to give my sincere thanks to my supervisor, Dr. David Howe Wood, for his consistent support and suggestions and also for his patient guideline when I was writing this thesis. I would also like to give my sincere thanks to Dr. Ali Tarokh and CFD group (Mohammad Arif, RC Adhikari, Hsu Lee, E Jieh, Marcel, Ripon, Ovi, Nowshad, Mahmud) at University of Calgary.

I am grateful to my mother, father, brother and sister for their unending support. Without their support I would not able to submit this thesis.

Table of Contents

Abstract ii

Acknowledgements iii

Table of Contents iv

List of Tables vii

List of Figures and Illustrations viii

CHAPTER ONE: INTRODUCTION 1

1.1 Background 1

1.2 Research Purpose 6

CHAPTER TWO: LITERATURE REVIEW 7

2.1 Introduction 7

2.2 Description of Previous Work 8

2.3 Verification of the Present Computational Fluid Dynamics 13

CHAPTER THREE: COMPUTATIONAL FLUID DYNAMICS MODEL 14

3.1 Introduction 14

3.2 Governing Equations of Fluid Flow 15

3.2.1 Reynolds-averaged Navier-Stokes (RANS) Equations 15

3.2.2 The Standard $\kappa - \varepsilon$ Turbulence Model 16

3.3 Finite Volume Method 17

3.4 SIMPLE Algorithm 20

3.5 Wind Flow around a Cube Building 20

3.5.1 Boundary and Initial Conditions 21

3.5.2 Numerical Setup 23
3.5.3 Computational Domain 23
3.5.4 Mesh Independence 27
3.6 Results and Comparison 31
3.7 Conclusion 35

CHAPTER FOUR: KAROLEENA BUILDING SIMULATION 37
4.1 Introduction 37
4.2 Wind Flow over the Karoleena Building 38
4.2.1 Boundary and Initial Conditions 38
4.2.2 Numerical Methodology 39
4.2.3 Computational Domain 39
4.2.4 Mesh Independence 40
4.3 Results and Discussion 42
4.3.1 Wind Normal to the Karoleena Building Face (0º) 42
4.3.2 Wind at 45º and 90º 47
4.3.3 Comparison between the NBCC Specifications and Present results 54
4.4 Conclusion 57

CHAPTER FIVE: SPRUNG BUILDING SIMULATION 58
5.1 Introduction 58
5.2 Wind Flow over the Sprung Building 59
5.2.1 Numerical Methodology 59
5.2.2 Computational Domain 59
5.2.3 Mesh Independence 61

5.3 Results and Discussion 62

5.3.1 Comparison between the Present results and Experimental data 70

5.4 Conclusion 73

CHAPTER SIX: CONCLUSIONS AND RECOMMENDATIONS 75

REFERENCES 78

List of Tables

Table 3.1: Model constants for the k-ε turbulence model (Jones and Launder (1972)) 17

Table 3.2: Velocities at different heights (z) from the ground (Richards and Hoxey (2001)) 22

Table 3.3: Total number of cells for all cases 25

Table 3.4: Grid Convergence Index for three integration variables. Subscripts 3, 2 and 1 represent Case-VII, Case-VIII and Case-IX. 29

Table 4.1: Karoleena building cases 40

Table 4.2: NBCC Design pressure coefficients and the present pressure coefficients 55

Table 4.3: Pressure coefficients for possible locations 56

Table 5.1: Sprung building cases 61

List of Figures and Illustrations

Figure 1.1: Cladding failure caused by wind induced pressure [Cook (1985)] 1

Figure 1.2: Karoleena (left) and Sprung (right) buildings 5

Figure 2.1: Vertical central section mean pressure coefficients with wind normal to one face (0º) [15 wind tunnel tests, wind tunnel average indicated by WT Ave and the full scale Silsoe full scale (F-S) Institute experiment from (Richards and Hoxey (2001), Richards et al. (2000))] 9

Figure 2.2: Pressure coefficients along the centreline of the windward facade, roof and leeward facade [15 wind tunnel tests, wind tunnel average indicated by WT Ave, Silsoe full scale (F-S) data and CFD results from Abohela et al. (2013) indicated as CFD] 12

Figure 3.1: Control volumes and nodal points (Versteeg and Malalasekera (2007)) 18

Figure 3.2: Simple computational domain with boundary conditions 22

Figure 3.3: Computational domain with the cube (Case-I) 24

Figure 3.4: Computational domain with the cube (Case-II) 24

Figure 3.5: Computational domain with the cube (Case-III) 24

Figure 3.6: Computational domain with the cube (Case-IV) 25

Figure 3.7: Computational domain with the cube (Case-V) 25

Figure 3.8: Pressure contour along the central section of the computation domain parallel to the wind direction for Case-I (Black arrow shows the wind direction) 26

Figure 3.9: Pressure coefficient along the windward centreline over the cube (Indicated by the red line) 27

Figure 3.10: Mesh resolution around the cube for Case-VII 28

Figure 3.11: Pressure coefficient along the windward centreline over the cube building (Indicated by the red line) 30
Figure 3.12: Velocity profiles at the indicated position (the centreline of the cube building) 30
Figure 3.13: Streamlines over the cube (The central section of the cube parallel to the wind direction and blue arrow shows the wind direction) 31
Figure 3.14: Pressure coefficient (C_p) over the cube at a mid-vertical section of the cube. The blue line is the present value, the green dotted line is the Silsoe Institute data (Richards and Hoxey (2001)), the red and black dotted lines are the CFD results-Fluent and the averaged wind tunnel data (Abohela et al. (2013)) [Black arrow shows the wind direction] 32
Figure 3.15: Pressure coefficient (C_p) around a cube at a mid-horizontal section of the cube. The blue line is the present value, the black dotted line is the Silsoe Institute data (Richards and Hoxey (2001)) and the red dotted line is the wind tunnel data of Castro and Robins (1977) [Black arrow shows the wind direction] 33
Figure 3.16: Pressure coefficient contour on the cube roof (White arrow shows the wind direction) 34
Figure 3.17: Turbulent kinetic energy contour though the vertical central plane of the computational domain (White arrow shows the wind direction) 35
Figure 4.1: The computational domain with the Karoleena building (left) and detailed view of the Karoleena building (right) with major dimensions 40
Figure 4.2: Velocity profiles along the indicated black line [Central section of the building (or computational domain) parallel to the wind direction] 41
Figure 4.3: Pressure coefficient along the centreline over the Karoleena building 41

Figure 4.4: Karoleena building with wind directions 42

Figure 4.5: Streamlines passing through the vertical central plane (0° wind flow)..... 43

Figure 4.6: Pressure coefficient along the indicated line (The centreline section of the Karoleena building parallel to the wind direction) (0° flow)..... 43

Figure 4.7: Pressure coefficient contour on the roof (White arrow shows the wind direction and black circle indicates zoom of roof's corner) (0° wind flow)..... 44

Figure 4.8a: Velocity profiles at the indicated locations for 0° flow [The origin for Y at -40 m and 180 m is different to the other locations and U_0 is the reference velocity $(30\mathrm{m/s})$. $\mathrm{U(-40), U(33.9) \ldots . and\ U(180)}$ are the velocities (U_x) along the vertical lines at the indicated locations $(-40, 33.9, \ldots . \text{and } 180)$.]..... 45

Figure 4.9: Turbulent kinetic energy contour k/U_0^2 (Oval indicates the second region of higher k and the x axis is the flow direction)..... 46

Figure 4.10: Streamlines passing through the vertical central section parallel to the wind direction (45º flow direction)..... 47

Figure 4.11: Streamlines passing through the vertical central section parallel to the wind direction (90º flow direction)..... 47

Figure 4.12: Pressure coefficient along the windward line over the Karoleena building (45º flow)..... 48

Figure 4.13: Pressure coefficient along the indicated line over the Karoleena building (90º flow)..... 49

Figure 4.14: Pressure coefficient contour on the roof (White arrow shows the wind direction and black arrow shows the region of the roof's corner for expanded contour on the left) (45º flow) 49

Figure 4.15: Pressure coefficient contour on the roof (White arrow shows the wind direction, black arrow shows zoom of roof's windward edge and circle shows highest lower C_p) (90º flow) 50

Figure 4.16a: Wind velocity (U_x) along indicated lines (45º) [The origin for Y at -40 m and 180 m is different to the other locations). $U(-40), U(33.9) \ldots .\text{and } U(180)$ are the velocities (U_x) along the vertical lines at the indicated locations $(-40, 33.9, \ldots .\text{and } 180)$.] 51

Figure 4.17a: Wind velocity profiles at indicated lines (90º) [The origin for Y at -40 m and 180 m is different to the other locations). $U(-40), U(33.9) \ldots .\text{and } U(180)$ are the velocities (U_x) along the vertical lines at the indicated locations $(-40, 33.9, \ldots .\text{and } 180)$.] 52

Figure 4.18: A cross-section view of the Karoleena building and the ground (90°) 53

Figure 4.19: Turbulent kinetic energy contour k/U_0^2 (45º flow) 53

Figure 4.20: Turbulent kinetic energy contour k/U_0^2 (90º flow) 53

Figure 4.21: Critical regions on the roof (z = 1 m, is end-zone width and θ is 4.7º) 54

Figure 4.22: Hand drawing of the NBCC building with mono-slope roof $[3° < \theta \leq 10°]$ 55

Figure 4.23: Possible locations of six PV modules on the Karoleena roof indicated by numbers. The red line indicates the boundary of critical regions. 56

Figure 5.1: Sprung building with major dimensions (Left) and a picture of the wind turbine (right) [Photo provided by Ron Hockin, Sprung Instant Structures Ltd.] 60

Figure 5.2: Mesh resolution of a computational domain (Sprung-1) 60

Figure 5.3: Wind velocity profile along the indicated white line 61

Figure 5.4: Pressure coefficient along the centreline over the Sprung building 62

Figure 5.5: Investigated wind directions (Top view of the building) 63

Figure 5.6: Streamlines around the Sprung building (along the central section of the building parallel to the wind direction (left) and bottom view (right)) for 0° flow 63
Figure 5.7: Streamlines around the Sprung building for 45° flow (Bottom view) 64
Figure 5.8: Streamlines around the Sprung building for 90° flow (Bottom view) 64
Figure 5.9: Velocity profiles along the indicated white lines (0° flow) [The central ($z = 0$) section of the building parallel to the wind direction. U-1, U-2, …. and U-6 are the velocities (U_x) along the vertical lines at those indicated locations.]..... 65
Figure 5.10: Velocity profiles along the indicated white lines (45° flow) 66
Figure 5.11: Velocity profiles along the indicated white lines (90° flow) 66
Figure 5.12: Velocity fields along the gable of the roof for all wind directions..... 67
Figure 5.13: Velocity field around the building for 0° case 68
Figure 5.14: Turbulent kinetic energy contour along the gable of the roof for all cases..... 68
Figure 5.15: Velocity profiles above the gable at different height (0^o wind flow)..... 69
Figure 5.16: Pressure coefficients over the Sprung building for all wind directions [Parallel to the wind direction] 70
Figure 5.17: Locations of the anemometer (left) and the top view of the experimental building (right) [Photo provided by Ron Hockin, Sprung Instant Structures Ltd.] 71
Figure 5.18: Measured wind directions (varies from -4° to 56.5°) 71
Figure 5.19: Comparison between the present results and field data 72
Figure 5.20: Time series of velocity fluctuation at west and south locations..... 72

Chapter One: **INTRODUCTION**

1.1 Background

Wind engineering is a multidisciplinary subject which is concerned with the effect of wind loads on the natural environment, buildings and built environment. Extreme wind loads on buildings can cause significant damage to the building roof, structure elements, excessive building motion, movement of air, water and dust through openings and cracks and undesirable opening of doors due to low pressure (Cermak (1975)). Cook (1985) examined the failure of a building structure caused by wind induced pressure. Figure 1.1 shows a typical cladding failure caused by wind induced pressure.

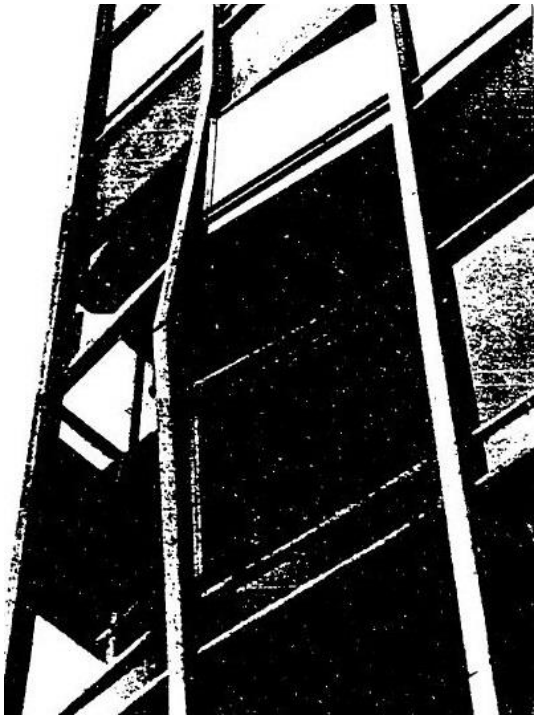

Figure 1.1: Cladding failure caused by wind induced pressure [Cook (1985)]

In order to minimize wind damage, the National Building Code of Canada (NBCC (2010)) has specified detailed regulations for designing and constructing buildings and/or building roofs usually in terms of extreme loads caused by, typically, a one in fifty years wind speed. The building code is continually updated for the better performance of buildings and roofs by absorbing research on the wind effects on scaled buildings and full scale buildings.

In addition, there has been a keen interest in using photovoltaic (PV) modules as a renewable source of energy (Kopp et al. (2012); Zhou and Zhang (2010); Stathopoulos et al. (2013)). A cost-effective and safe design for the installation of roof-mounted PV modules requires accurate information of the wind flow characteristics and other factors. These can affect significantly the cost of the structures and influence the project cost. Wind flow generally produces the highest suction pressure on the roof, where this suction pressure may damage the building cladding, structures and other components, Cook (1985). Similarly, Due to the wind, a large suction pressure may occur on the roof in some zones such as windward edges, ridges, corners, etc. Hence, the resulting pressure difference between top and bottom surfaces may cause the roof to fail and or the PV modules to detach. Various researches have been conducted on the wind loads on roof-mounted PV modules (Aly and Bitsuamlak (2014); Stathopoulos et al. (2013); Ming et al. (2010); Kopp et al. (2002)). The existing literature has limited information for calculating the extreme wind loads on roof mounted PV modules, especially for mono-slope roof buildings. There have also been limited full scale investigations for different types of roof shapes and roof angles in the literature.

Conventionally, there have been two ways of examining the flow over buildings: (i) experiments on full scale buildings and (ii) wind tunnel experiments simulating with the natural wind characteristics. In an open exposed position, Richards and Hoxey (2001) examined the natural

wind flow effects around a cube building ($6 \times 6 \times 6\ m^3$) at the Silsoe Institute, UK. They reported that the roof and leeward wall pressures appear to be sensitive to Reynolds number, which is the ratio of inertial forces to viscous forces. Field experiments are very expensive and time consuming. Extensive wind tunnel experiments have been done for scaled building models including those by (Jing and Li (2013), Richards and Hoxey (2006), and Castro and Robins (1977)) who have compared their results with Silsoe Institute experimental data. A detailed literature review can be found in chapter two in this thesis. Natural wind conditions are simulated by adopting the turbulent boundary layer type airflow in wind tunnels. The Reynolds numbers in wind tunnel tests based on scaled building models are usually much smaller than for real buildings, and also the boundary effects of the wind tunnel are usually unavoidable (Zhou (1995)). Although wind tunnel experiments are widely used to examine the wind effects around the buildings, they are expensive, time consuming and costly.

CFD is more efficient for the investigation of wind loads on buildings than the two methods discussed above and the only available methodology at the design stage. Hence, it is more feasible to use CFD in analyzing the building shapes and locations. As explained in Chapter two, it has already achieved popularity for designing buildings and selecting the locations for PV installations. CFD can overcome the boundary effects of wind tunnel and also the limitation of the Reynolds number. It was not until the end of the 20th century that CFD became feasible due to the increase in the computer speed and memory capacities. Recently, wind tunnel experiments have been partly replaced by CFD methods because some limitations that are posed by experimental methods such as the testing of a full scale building, boundary effects and the limitation of Reynolds number. And there is a necessity to build a model for testing.

Karoleena Homes is a company designing and constructing buildings or homes in Calgary, AB, Canada. The unusual feature is that Karoleena build prefabricated homes so it is possible to integrate directly PV modules to the roof. To minimize the cost of installing roof-mounted PV modules, they are interested in finding more information for the extreme loads over the building especially on roof-mounted PV modules as defined by the NBCC (2010) (Section 4.3.3). Sprung instant structures, which is a major Canadian company, builds homes, recreation buildings, industrial plants, and many other buildings. They use tent technology (tent structural buildings) to construct industrial, military, mining buildings etc. The tent structural building is a quickly erected, reliable shelter designed for a comfortable interior, and to withstand extreme wind speeds and snow loads. Currently, they are investigating the performance of a transverse axis wind turbine (see Figure 5.1) located along the gable of the roof for their future buildings. To analyze and optimize the wind turbine performance, they need more information for wind flow over the gable of the roof. Karoleena Homes is interested in extreme wind flow over its buildings to minimize the structural cost of the roof. Sprung instant structures is interested in the typical wind flow over the building to assess the performance of a wind turbine. The present research objectives are listed in the next section. In addition, the Karoleena building has a mono-slope roof (Figure 1.2). This was designed for uneven ground and has PV modules in the middle of the roof. On the other hand, the Sprung building is a tent roof building on flat ground and with a wind turbine along the gable of the roof (Figure 1.2). The wind turbine is not included in this building simulation. The detailed building geometries and simulation results are discussed in Chapter four (Karoleena) and Chapter five (Sprung). As explained in Chapter two, there are insufficient information for the wind loads over Karoleena and Sprung type buildings in the literature (Stathopoulos and Mohammadian (1985), Franke et al. (2007), WINEUR (2007), Abohela et al. (2013)). It should be noted that there

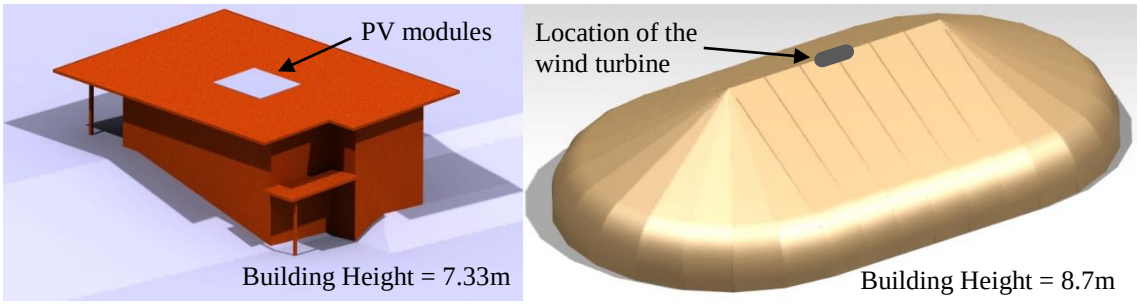

Figure 1.2: Karoleena (left) and Sprung (right) buildings

is no wind provision for Sprung type building in NBCC (2010), but there is limited information for general mono-slope building (Figure 4.22).

In this present research, the wind loads on small buildings have been simulated using the standard $k-\varepsilon$ turbulence model (Jones and Launder (1972)) [see Section 3.2.2]. The model is used to obtain the mean pressure on building roofs and mean velocity fields around buildings. This turbulence model is one of the simplest models and is used commonly for wind flow over buildings (Versteeg and Malalasekera (2007)). Therefore, the standard $k-\varepsilon$ turbulence model is preferred for these building simulations. More details can be found in Chapter three.

OpenFOAM is a free, open source CFD software package that is being used extensively in research and development. It has an extensive toolbox to solve complex fluid flows including turbulence, heat transfer etc (OpenFOAM (2014)). Rakai and Kristóf (2010) simulated the flow over an urban setting using OpenFOAM CFD. They reported that OpenFOAM CFD has an efficient toolbox for modeling urban atmospheric flows. Franke et al. (2012) investigated the flow over several building cases using the standard $k-\varepsilon$ turbulence model also using OpenFOAM CFD. They described OpenFOAM CFD in detail and found a good agreement between the numerical results and experimental data for velocity fields. In Chapter three (CFD Model), OpenFOAM CFD is

explained in detail and CFD tools, choice of boundary conditions and numerical setup are validated by comparing with the published experimental data and ANSYS Fluent (CFD toolbox) results. The wind effects on buildings (Karoleena and Sprung) are estimated by using similar validated CFD model (Chapters four and five). The general discussion, conclusions and recommendations are given in Chapter six.

1.2 Research Purpose

The following are the aims for the studies of wind flow over Karoleena and Sprung buildings.

- Validate the CFD simulations by comparison to the pressure and flow field measurements over the Silsoe cube building
- Investigate the extreme wind loads on PV modules attached to low-rise mono-slope building for different wind directions
- Analyze the wind induced pressures and velocity fields on the Karoleena building
- Predict the best location (s) of minimum wind load (minimum structural cost) for Karoleena roof-mounted PV modules
- Analyze and predict the velocity fields around the gable of the roof for the future analysis of a transverse wind turbine on the Sprung building

Chapter Two: **LITERATURE REVIEW**

2.1 Introduction

Computational Fluid Dynamics numerically solves the partial differential equations of fluid flow. Thus, it can be used to investigate the effect of wind flow over buildings or obstacles of complex shape. In CFD, the computational domain is discretized into a small volume mesh where the numerical methods, such as Finite Volume Method (FVM), Finite Differential Method (FDM) or Finite Element Method (FEM), are applied to solve the Navier-Stokes equations as a set of algebraic equations. After applying the proper boundary conditions, the algebraic equations are solved numerically to predict the effect of wind flow over or around the building (s).

The application of CFD to Wind Engineering problems began in the 1960s (Fromm and Harlow (1963)). Patankar et al. (1974) successfully solved the governing equations of fluid flow using FVM. Many companies have developed CFD software such as ANSYS-Fluent, AEA Technology, and the OpenFOAM Foundation. In CFD, full scale buildings can be simulated to estimate the flow effects of wind load on buildings. It has been established and validated by many researchers and practicing engineers by comparing computations with published wind tunnel experimental and full size data for different buildings (Frank (1996), Gadilhe et al. (1993), Hanson et al. (1986), Launder and Spalding (1974)). In wind tunnel tests, there are limitations in simulating large buildings, and the details of the atmospheric boundary layer, but CFD can overcome most of these problems at the cost of possibly introducing errors due mainly to the turbulence modeling. These are explained in detail in the next section which describes the previous research on the wind flow around different roof shape buildings. The disadvantage of CFD is the turbulence models that must

be validated. Hence the next section describes research on the flow over a generic building that has been extensively used for validation.

2.2 Description of Previous Work

Castro and Robins (1977) examined the detailed mean pressure distribution and velocity fields around a cube building in a simulated atmospheric boundary layer in a wind tunnel. They observed that the decay of the velocity deficits in the wake is a function of the turbulent intensity, which is the root mean square of the velocity fluctuations divided by a reference mean velocity, by comparing with previous work. The flow was dominated by strong vortices from the top edges of the cube when the flow approaches the cube at 45^{o} to the main axis of the building or roof. In order to examine the natural wind effects on a small cube building, Richards et al. (2000) constructed a $6 \times 6 \times 6\ m^3$ building in an open exposed location at the Silsoe Research Institute. They measured the mean velocity and pressure around the cube building. Then, they measured the pressure on the surface of the cube building (Richards and Hoxey (2001)) for comparison with wind tunnel data of Castro and Robins (1977) and other wind tunnel tests. Figure 2.1 taken from Richards and Hoxey (2001) compares the results of 15 wind tunnel tests, the average of those data and Silsoe results. The distance over the cube is the distance along the indicated lines (0-1, 1-2 and 2-3) defined in the inset to the figure, which are at equal distance (6 m), for a cubic building. They also observed that most of the experimental results agreed with the location of maximum pressure (stagnation point) on the windward wall. The stagnation point, determined as the point of the maximum pressure coefficient, occurred at about three-quarters of cube height on windward wall,

but the pressure coefficient is less than 1.0. All the pressure results are calculated and plotted non-dimensionally in the form of a pressure coefficient, C_p, defined by

$$C_p = \frac{p - p_0}{\frac{1}{2}\rho U_0^2} \tag{2.1}$$

where p and p_0 are the surface static pressure and reference pressure, ρ is the density of air and U_0 is the reference velocity.

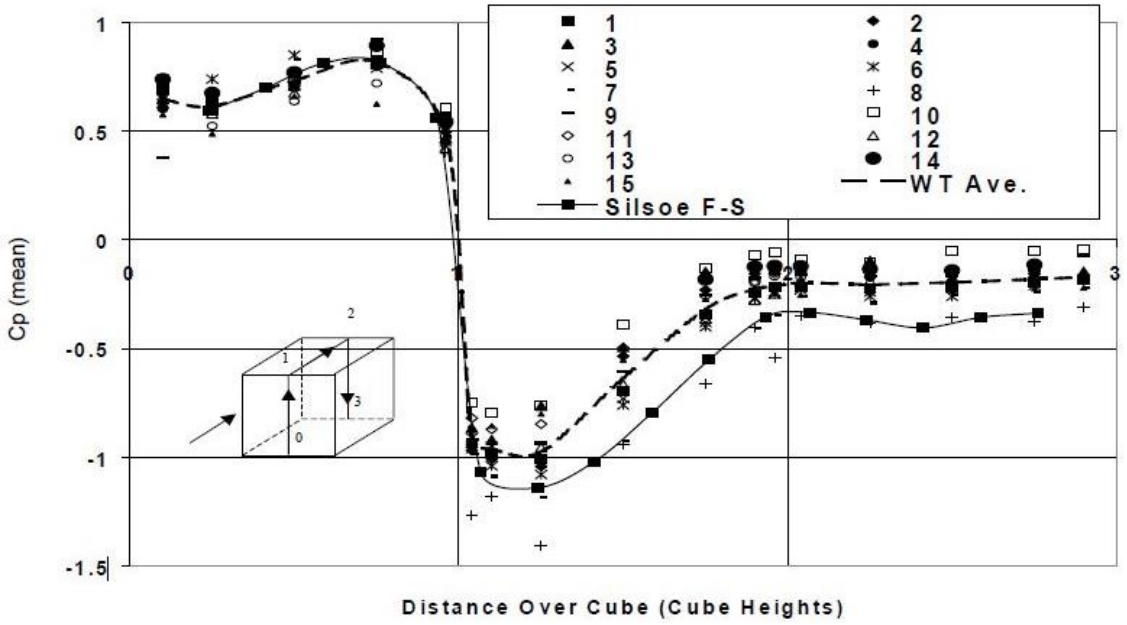

Figure 2.1: Vertical central section mean pressure coefficients with wind normal to one face (0º) [15 wind tunnel tests, wind tunnel average indicated by WT Ave and the full scale Silsoe full scale (F-S) Institute experiment from (Richards and Hoxey (2001), Richards et al. (2000))]

Some significant differences between the pressure measured in the wind tunnel tests and Silsoe experiment were found at the roof and leeward wall of cube because of the effect of Reynolds number and the roughness (Richards and Hoxey (2001)). They mentioned that the Reynolds number may affect the results on the roof of the cube building. Paterson and Apelt (1989)

numerically simulated the wind flow around a cube to calculate the mean pressure coefficient and velocity fields using the standard $k-\varepsilon$ turbulence model and compared these results with wind tunnel experimental results of Castro and Robins (1977). The overall agreement was good with simulated mean pressures and velocities having errors of approximately $5-10\%$. Sousa and Pereira (2004) examined the vorticity around a surface mounted cube with and without gable roof in a wind tunnel. The maximum value of the mean vorticity was approximately the same for both geometries. The maximum vorticity occurred over the roof after flow separation, which happens when wind flowing past a building separates from the roof and forms a region of recirculating flow. They also reported that the maximum value of C_p was very similar for flat and gable roofs. For flat roofs, they found a good agreement in a comparison between their results and wind tunnel experimental results of Castro and Robins (1977).

There is only limited information on the wind loads on full scale low-rise buildings with mono-slope roofs. Most researchers examined scaled cube models for the approximation of the wind loads on roof-mounted PV modules including Stathopoulos and Mohammadian (1985), Cui (2007), Kopp et al. (2012), Aly and Bitsuamlak (2013), Stathopoulos et al. (2013). In a wind tunnel, Stathopoulos and Mohammadian (1985) examined the wind load on a mono-slope roof building for different building heights. They observed that the suction pressure on the roof was higher in magnitude than the suction pressure on flat and gable roofs. This may depend on wind direction. The experimental results also show some dependence on height, particularly for corner points, where the suction increased significantly with increasing building height. Cui (2007) examined the extreme wind loads over a scaled building model to determine the mean pressure coefficients on the roof with different angles of the roof in a wind tunnel. He found some

differences between the mean pressure coefficients and that the values in the NBCC (2010) which provides pressure coefficients for different generalized roof shapes (flat roof, gable roof, mono-slope roof etc) for design purposes.

CFD simulation was employed to determine the wind loads on PV modules for different wind directions and validated with the experimental results of Shademan and Hangan (2009). They calculated the lift and drag forces on PV modules and reported that CFD simulations appeared to be an efficient tool for design purpose. For detailed analysis of the wind loads on roof-mounted PV modules, Kopp et al. (2012) studied scale models of the building and the modules in a large wind tunnel. They found that a large PV array (a set of PV modules) increased the turbulence level and the net wind loads for higher tilt angles of the modules. The net wind loads decrease for lower angles due to the pressure equalization. They also reported that the wind directions are very important for roof-mounted PV modules building.

The wind loads on ground-mounted PV modules were examined in a wind tunnel (Aly et al. (2013)). The mean pressure loads were not significantly affected by the test model size. They mentioned that very small size PV modules may have different mean pressure loads. They also examined the minimum and maximum pressure locations on the roof and recommended that PV modules should not be mounted near the roof edge, ridge and corners because higher suction occurs at those locations. The comparison of the wind loads on front and back (or near the windward and leeward faces) PV modules were carried out by Stathopoulos et al. (2013). They observed that the pressure coefficients were affected by the module inclination for the critical wind direction.

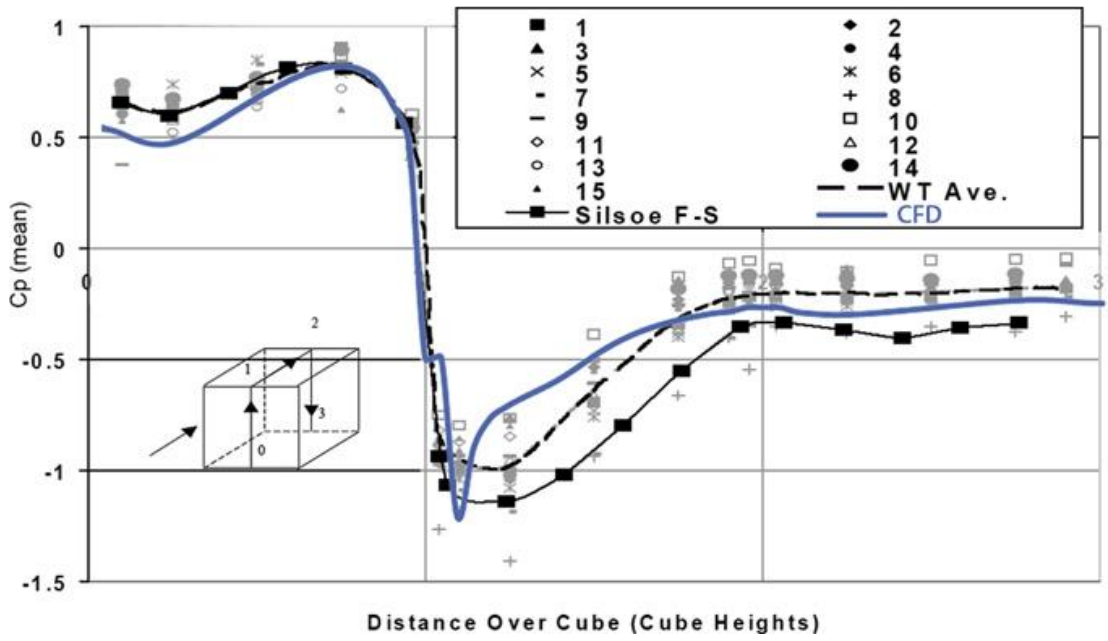

Figure 2.2: Pressure coefficients along the centreline of the windward facade, roof and leeward facade [15 wind tunnel tests, wind tunnel average indicated by WT Ave, Silsoe full scale (F-S) data and CFD results from Abohela et al. (2013) indicated as CFD]

In this research, the Sprung (tent roof) building has also been numerically examined to predict the flow fields along the gable of the roof as noted in the list of objectives (chapter one). The geometry of this building is discussed in detail in chapter five. Of relevance to this building simulation, a number of studies estimated the velocity field along the gable of the roof (Cook (1985), Franke et al. (2007), WINEUR (2007), Tominaga et al. (2008), Wood (2011), Abohela et al. (2013)). Most researchers observed that simulated velocity fields around a building are generally more accurate than simulated pressure fields by comparing with experimental data. But there is very little information on the flow fields near the gable of the roof for buildings similar to the tent one. Note that Sprung Company chose to mount the wind turbine (s) along the gable. Abohela et al. (2013) examined the wind flow over various roof shaped buildings (scaled models) for different wind

directions. They suggested that the wind turbine produces 56.1% more electricity for the barrel vaulted roof compared to other roof shapes. They also found good agreement by comparing the calculated mean pressure coefficient results with the experimental results (Richards and Hoxey (2001)) for cube building (Figure 2.2). It is noted that there is no specific wind provision for the Sprung type building in the NBCC (2010).

2.3 Verification of the Present Computational Fluid Dynamics

To assess the accuracy of CFD simulations, it is necessary to compare with recognized experimental data. In this research, the steady state Reynolds averaged Navier-Stokes equations and the standard $k-\varepsilon$ turbulence model are used to estimate the wind flow over the building with the well-known SIMPLE (Semi-Implicit Methods for Pressure Linked Equations) method (Patankar (1980)) in OpenFOAM CFD. To follow a systematic investigation of wind loads around buildings, the wind flow around a cube building is compared with the experimental data for validation. The validation of boundary conditions, which are explained in the next chapter, are very important to ensure the accuracy of the simulations. Therefore, the cube simulation included an investigation of the boundary conditions. After validation, a similar CFD model is applied for Karoleena and Sprung building simulations to obtain consistent numerical results.

Chapter Three: **COMPUTATIONAL FLUID DYNAMICS MODEL**

3.1 Introduction

In this chapter, wind loads around a cube building (the Silsoe full scale cube building) are simulated using the standard $k-\varepsilon$ turbulence model and compared to the measurements for validation. The cube simulation is very popular for validating the numerical setup and the choice of boundary conditions (Section 3.5.1) before solving the wind flow around more complex building geometries. First, the governing equations, turbulence model, numerical methods are explained in detail. Then, boundary effects and the dependence on grid are checked in OpenFOAM CFD, which are discussed in detail later in this Chapter. The cube results are compared with previous wind tunnel data, Silsoe field data and results from the commercial CFD software Fluent. The main purpose of this cube simulation is to assess CFD software OpenFOAM, which will be applied to the Karoleena and Sprung buildings.

The objective of the cube simulation are

- Investigate wind flow effects around a cube building ($6 \times 6 \times 6\ m^3$)
- Determine mean pressure distribution on the roof of the cube building and velocity fields around the cube building
- Validate OpenFOAM CFD results by comparing with the previous experimental data and CFD results

3.2 Governing Equations of Fluid Flow

In this section, the governing equations of fluid flow are described briefly. From Versteeg and Malalasekera (2007), the mass and momentum conservation equations in three dimensional Cartesian co-ordinates are given below for steady incompressible flow.

The conservation of mass is

$$div\ (\tilde{u}) = 0 \tag{3.01}$$

In Equation (3.01), $\tilde{u}$ is the velocity vector.

The conservation of momentum is given by

$$div(u\tilde{u}) = -\frac{1}{\rho}\frac{\partial p}{\partial x} + div\big(\nu\ grad(u)\big) \tag{3.02}$$

$$div(v\tilde{u}) = -\frac{1}{\rho}\frac{\partial p}{\partial y} + div\big(\nu\ grad(v)\big) \tag{3.03}$$

$$div(w\tilde{u}) = -\frac{1}{\rho}\frac{\partial p}{\partial z} + div\big(\nu\ grad(w)\big) \tag{3.04}$$

where ρ is the density of the fluid, p is the pressure and ν is the kinematic viscosity of the fluid.

3.2.1 Reynolds-averaged Navier-Stokes (RANS) Equations

From Versteeg and Malalasekera (2007), the final equations of RANS for steady incompressible flow are given by

$$div\big(U\widetilde{U}\big) = -\frac{1}{\rho}\frac{\partial P}{\partial x} + div\big(\nu\ grad(U)\big) - \left[\frac{\partial(\overline{u'^2})}{\partial \mathrm{x}} + \frac{\partial(\overline{u'v'})}{\partial y} + \frac{\partial(\overline{u'w'})}{\partial z}\right] \tag{3.05}$$

$$div\big(V\widetilde{U}\big) = -\frac{1}{\rho}\frac{\partial P}{\partial y} + div\big(\nu\ grad(V)\big) - \left[\frac{\partial(\overline{u'v'})}{\partial \mathrm{x}} + \frac{\partial(\overline{v'^2})}{\partial y} + \frac{\partial(\overline{v'w'})}{\partial z}\right] \tag{3.06}$$

$$div(W\widetilde{U}) = -\frac{1}{\rho}\frac{\partial P}{\partial z} + div(\nu\ grad(U)) - \left[\frac{\partial(\overline{u'w'})}{\partial \mathrm{x}} + \frac{\partial(\overline{v'w'})}{\partial y} + \frac{\partial(\overline{w'^2})}{\partial z}\right] \qquad (3.07)$$

where U, V and W are mean velocities, $\widetilde{U}$ is the velocity vector, P is the mean pressure, $\overline{u'^2}, \overline{u'v'}, \overline{u'w'}, \overline{u'v'}, \overline{v'^2}, \overline{v'w'}, \overline{u'w'}, \overline{v'w'}$ and $\overline{w'^2}$ are the Reynolds stresses.

Equations (3.05 to 3.07) are called the RANS equations. Extra terms ($\overline{u'_\iota v'_J}$) appear in the RANS equations due to the interactions between various turbulent fluctuations. To close the system, there must be enough equation (s) to solve the Reynolds stress. Based on Reynolds averaging, many turbulence models were developed such as one equation model of Spalart and Allmaras (1994), and two equation models (an example being the standard $k-\varepsilon$ turbulence model) of Launder and Spalding (1974) etc. In this research, wind effects over full scale buildings are investigated using the standard $k-\varepsilon$ turbulence model to calculate the mean pressure distribution and velocity fields. In the next section, the standard $k-\varepsilon$ turbulence model is described briefly.

3.2.2 The Standard $\kappa-\varepsilon$ Turbulence Model

The standard $k-\varepsilon$ turbulence model is a very popular and common turbulence model in CFD fields. It is a two equations model which accounts for history effects like convection and diffusion of turbulent energy. One equation is for the turbulent kinetic energy (k) and another is for the rate of dissipation of turbulent kinetic energy (ε). It is a validated turbulence model used for industrial and environmental flow applications as discussed in chapter two. In this section, the equations of the standard $k-\varepsilon$ turbulence model are written and the values of the model constants are given. The transport equations of the standard $k-\varepsilon$ turbulence model are shown below for steady incompressible flow.

$$\rho\, div\left(k\tilde{U}\right) = div\left[\frac{\mu_t}{\sigma_k} grad\ k\right] + 2\mu_t S_{ij}.S_{ij} - \rho\varepsilon \tag{3.08}$$

$$\rho\, div\left(\varepsilon\tilde{U}\right) = div\left[\frac{\mu_t}{\sigma_\varepsilon} grad\ \varepsilon\right] + \frac{C_{1\varepsilon}\varepsilon}{k} 2\mu_t S_{ij}.S_{ij} - \frac{C_{2\varepsilon}\rho\varepsilon^2}{k} \tag{3.09}$$

where, $C_\mu, \sigma_k, \sigma_\varepsilon, C_{1\varepsilon}$ and $C_{2\varepsilon}$ are model constants and μ_t is the turbulence eddy viscosity. The values of these model constants are shown in Table 3.1. The constants were arrived at by comprehensive data fitting for a wide range of turbulent flow. This is one of the simplest turbulence model and commonly used for industrial purposes. According to the literature (such as Rodi (1997)), the computational cost of this model is lower than other turbulence models. Therefore, the standard $k-\varepsilon$ turbulence model is chosen for the building simulations.

Table 3.1: Model constants for the $k-\varepsilon$ turbulence model (Jones and Launder (1972))

Model constants	Value
C_μ	0.09
σ_k	1.00
σ_ε	1.30
$C_{1\varepsilon}$	1.44
$C_{2\varepsilon}$	1.92

3.3 Finite Volume Method

In this section, the finite volume method for solving the RANS equations is described briefly. The finite volume method is used to transform scalar transport equations into linear algebraic relations. For example, consider a simple steady state diffusion equation with source term.

$$div(\Gamma\ grad\ \phi) + S_\phi = 0 \tag{3.10}$$

where, Γ is diffusion coefficient, ϕ is the conservative form of a typical fluid flow (properties) and S_ϕ is the source term.

The finite volume method divides the domain into discrete control volumes. Then, the governing equations are discretized for every nodal point (P) and integrated over a control volume. Figure 3.1 shows typical control volumes and nodal points for a one-dimensional domain. For a control volume, equation (3.10) is integrated at nodal point P and it gives

$$\left(\Gamma A \frac{d\phi}{dx}\right)_e - \left(\Gamma A \frac{d\phi}{dx}\right)_w + \bar{S}\Delta V = 0 \tag{3.11}$$

where A is cross-sectional area of the control volume face, ΔV is volume, $\bar{S}$ is average value of source S, e and w are the control volume faces (or east and west faces).

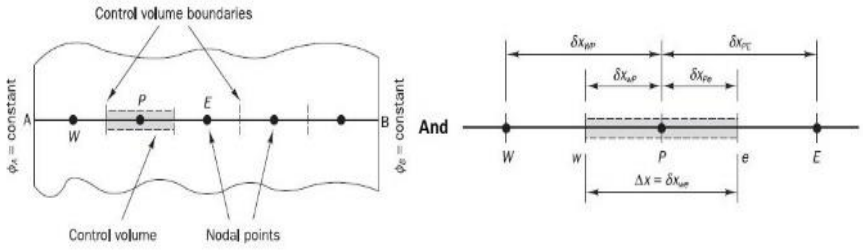

Figure 3.1: Control volumes and nodal points (Versteeg and Malalasekera (2007))

Calculating the gradient of property fluxes requires an assumption for the variation between the nodal points. Consider central differencing which is used to discretize the diffusion terms (the first two terms in the left hand side of equation (3.11)). The central differencing scheme is 2nd order accurate based on truncation of a Taylor series expansion. To explain this scheme, the property flux terms in equation (3.11) are given by interpolating for uniform grid:

$$\left(\Gamma A \frac{d\phi}{dx}\right)_e = \Gamma_e A_e \left(\frac{\phi_E - \phi_P}{\delta x_{PE}}\right) \tag{3.12}$$

$$\left(\Gamma A \frac{d\phi}{dx}\right)_w = \Gamma_w A_w \left(\frac{\phi_P - \phi_W}{\delta x_{WP}}\right) \tag{3.13}$$

P, E and W are nodal points. The source term is approximated by means of a linear form, $\bar{S}\Delta V = S_u + S_p \phi_P$

Substituting these into the equation (3.11) and simplifying gives

$$\left(\frac{\Gamma_e A_e}{\delta x_{PE}} + \frac{\Gamma_w A_w}{\delta x_{WP}} - S_p\right)\phi_P = \frac{\Gamma_w A_w}{\delta x_{WP}}\phi_W + \frac{\Gamma_e A_e}{\delta x_{PE}}\phi_E + S_u \tag{3.14}$$

Equation (3.14) is of the form:

$$a_P \phi_P = a_W \phi_W + a_E \phi_E + S_u \tag{3.15}$$

where a_P, a_W and a_E are constants. Therefore, a set of algebraic equations are formed by applying the central differencing scheme, which can be solved by Successive Over Relaxation (SOR) method. SOR is an iterative method and a variant of the Gauss-Seidel method for solving a linear system of equations. The method is easy to implement and easy to change the relaxation factor to maintain stability. In this work, the successive over relaxation method was used. The equation for the m^{th} iteration with the relaxation factor (ω) [See the next section] is given by

$$x_i^m = x_i^{m-1} + \frac{\omega\left(b_i - a_{ij}x_i^{m-1} - \sum_{j=1}^{i-1} a_{ij}x_j^m - \sum_{j=i+1}^{n} a_{ij}x_j^{m-1}\right)}{a_{ii}} \tag{3.16}$$

where x is the fluid properties (ϕ_i) at every point, m is the number of iteration, n is the number of the grid point, a_{ij}, a_{ij} and b_i are constants and ω is the relaxation faction. In OpenFOAM CFD, there are many schemes such as 1st order upwind, 2nd order linear upwind, power law and QUICK (Quadratic Upwind Interpolation for Convective Kinematics) schemes. The central differencing and 2nd order upwind differencing schemes are used because these schemes comparatively give

better agreement and are less time consuming than higher order schemes. Therefore, 2nd order schemes are used for this work.

3.4 SIMPLE Algorithm

The SIMPLE (Semi-Implicit Method for Pressure Linked Equations) algorithm is used to link the pressure and velocity equations. The scalar variable pressure is calculated at nodal points while the velocity components are calculated on staggered grids centred on the cell faces (Versteeg and Malalasekera (2007)). This algorithm is basically a predictor-corrector procedure to calculate the pressure on the grid. Predictor-corrector has two steps: first is the prediction of the quantity and the second is the correction of that quantity. First the pressure is guessed in order to solve the discretized velocity equations, then a corrector pressure is used to correct the velocity components and to satisfy the continuity equation. For the SIMPLE algorithm, the under relaxation factor ($0 < \omega < 1.0$) requires for all equations because the pressure correction equation is susceptible to divergence during the iterative process. A detailed study of the SIMPLE algorithm can be found in Versteeg and Malalasekera (2007).

3.5 Wind Flow around a Cube Building

In this section, wind flow around a cube building is studied as a test and validation case by checking the effects of choices of boundary conditions, computational volume and mesh independence. Then, the cube results are compared with previous experimental data and other CFD simulations.

3.5.1 Boundary and Initial Conditions

Boundary conditions represent the influence of the boundaries that are the edge of the computational domain. Initial conditions are the distribution of flow variables that needs to be specified at the inlet. These conditions are very important in CFD simulation. CFD practice guidelines for using CFD were reviewed. And the set of parameters used in this thesis were extracted from that guidelines (Franke and Miles (2002), WINEUR (2007), Blocken et al. (2011)). The top, front and back boundaries use a slip condition (where the viscous effects are negligible and the velocity along the boundary can be non-zero). The ground and cube building boundaries use a no-slip wall ($u = v = w = 0$).

For the standard $k - \varepsilon$ turbulence model, the inlet conditions are (Versteeg and Malalasekera (2007))

$$u^* = \frac{u}{u_\tau} = \frac{1}{K}\ln(Ey^+), \qquad k = \frac{u_\tau^3}{\sqrt{C_\mu}}, \qquad \varepsilon = \frac{u_\tau^3}{Ky} \tag{3.17}$$

where u^* is the dimensionless velocity, u is the mean velocity, u_τ is the friction or shear velocity, K is von Karman's constant (0.41), E is the wall roughness parameter, y^+ is the dimensionless wall distance for a wall-bounded flow, k is the turbulent kinetic energy, ε is the turbulent dissipation rate and y is the co-ordinate direction normal to a wall (y axis).

Figure 3.2 shows a simple computational domain with different boundary conditions. The logarithmic wind velocity (log law) profile was used at the inlet and outlet was zero pressure gradient (Franke and Miles (2002)). The log law only holds for the inner $10 - 15\%$ of a boundary layer, after which there is a smooth distribution towards the free stream in a wind tunnel

experiments, or towards the flow above the surface layer in the atmospheric boundary layer. Note that turbulent kinetic energy (k) is constant because there is no dependent variable (y) in equation (3.17) and a requirement of the $k-\varepsilon$ model.

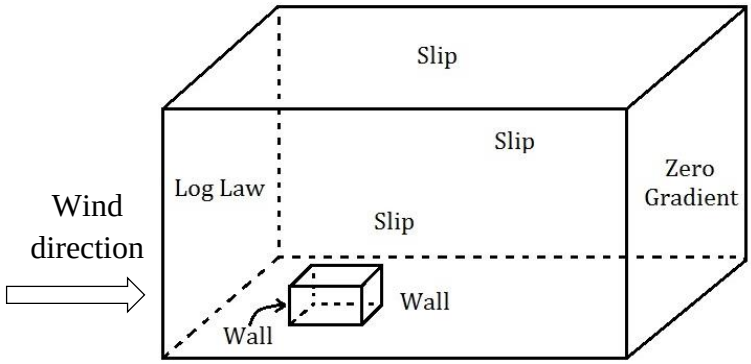

Figure 3.2: Simple computational domain with boundary conditions

To compare the present cube results with experimental data, the initial conditions were taken from the Richards and Hoxey (2001) field data. The initial value of k was calculated ($1.2\ m^2/s^2$) from Equation (3.17). Equation (3.17) can be rewritten by (Richards and Hoxey (1993))

$$u(y)=\frac{u_\tau}{\kappa}ln\left(\frac{y+z_0}{z_0}\right), k=\frac{u_\tau^3}{\sqrt{C_\mu}}, \varepsilon=\frac{u_\tau^3}{K(y+z_o)} \tag{3.18}$$

where z_0 is the aerodynamic roughness length. In this cube simulation, Silsoe Institute data were used to construct the profiles and calculate the turbulent kinetic energy. Table 3.2 shows the Silsoe Institute data.

Table 3.2: Velocities at different heights (z) from the ground (Richards and Hoxey (2001))

Properties of the full-scale approach flow

z (m)	U (m/s)
1	6.97
3	8.65
6	9.52
10	10.13

3.5.2 Numerical Setup

The SIMPLE algorithm and SOR are used with the relaxation factors (ω): 0.7 for velocities (U), the turbulent kinetic energy (k), the turbulent dissipation rate (ε) and 0.3 for pressure (p). These relaxation factors were recommended by the OpenFOAM user guide and best CFD guidelines (Franke and Miles (2002), WINEUR (2007), Tominaga et al. (2008), Blocken et al. (2011)). It is impossible to predict the value that gives optimum convergence for each problem. Thus it is common to rely on values used for similar simulation. Convergence was assumed when the residuals (a measure of the error in the solution) used 10^{-7} for U, k, ε and 10^{-4} for p. More precisely, the residual is evaluated by substituting the current solution into the equation and taking the magnitude of the difference between the left and right hand sides. It is also normalized to make it independent of the scale of the problem being analyzed (OpenFOAM (2014)).

3.5.3 Computational Domain

Several cases were created for checking the flow effects of the computational blockage ratio, which is the ratio of the frontal area of the cube building and the cross-sectional area of computational domain normal to the wind direction, namely, Case-I, Case-II, Case-III, Case-IV and Case-V. Figures 3.3, 3.4, 3.5, 3.6 and 3.7 show the computational domains with dimensions, where the height of the building (H) is 6.0 m. Franke et al. (2007) recommended that the blockage ratio should be less than 3%. The distance from the inflow and sidewalls boundaries to the building should be more than 5H. Similar recommendations were found in Baetke et al. (1990), Franke and Miles (2002), and Blocken et al. (2011). The outlet boundary should be placed more than 15H from the building. To verify the boundaries and blockage ratio effects on the results, three cases

(Case-I, Case-II, Case-III, Case-IV and Case-V) were carried out. The OpenFOAM (2014) mesh tools were used to generate the meshes for cube building. The total number of cells for every case is shown in Table 3.3. Case-VI, Case-VII, Case-VIII and Case-IX are discussed in the next section.

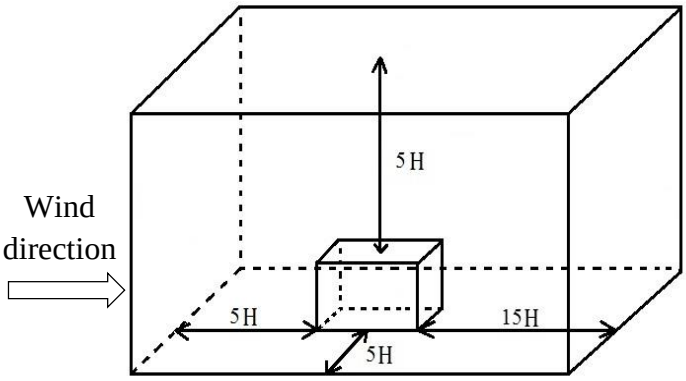

Figure 3.3: Computational domain with the cube (Case-I)

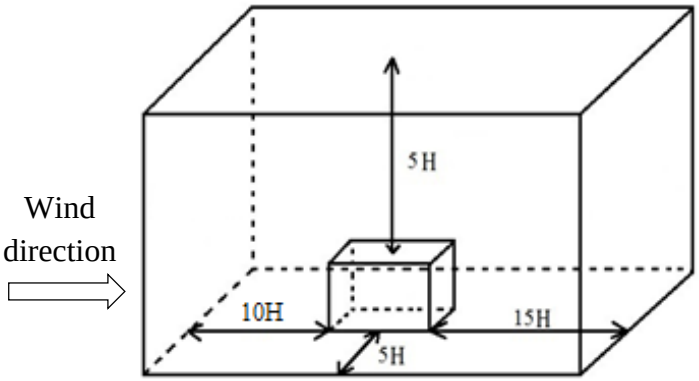

Figure 3.4: Computational domain with the cube (Case-II)

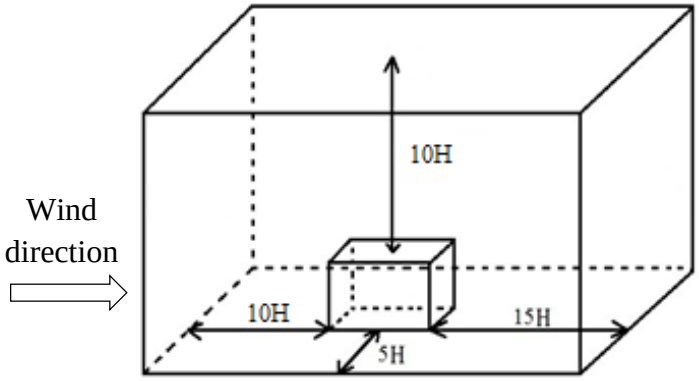

Figure 3.5: Computational domain with the cube (Case-III)

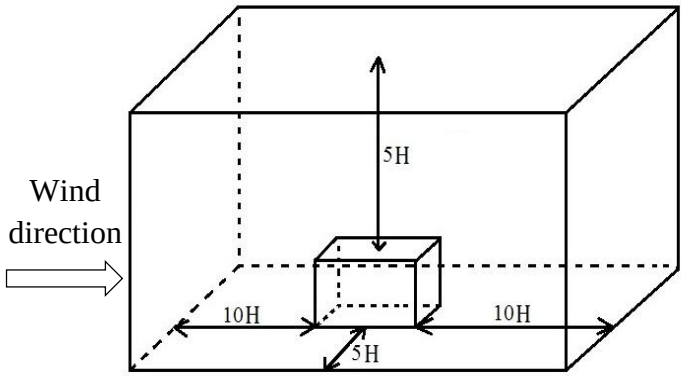

Figure 3.6: Computational domain with the cube (Case-IV)

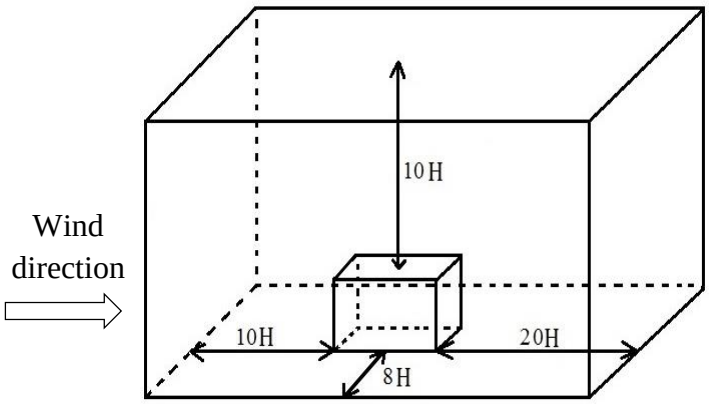

Figure 3.7: Computational domain with the cube (Case-V)

Table 3.3: Total number of cells for all cases

Case	I	II	III	IV	V	VI	VII	VIII	IX
Total number of cells (million)	4.65	1.13	1.53	5.28	16.20	2.60	6.12	1.65	6.60

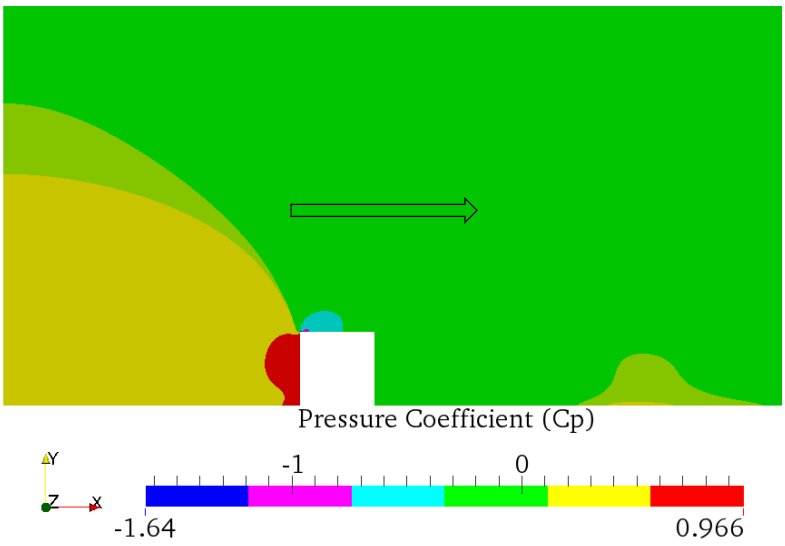

Figure 3.8: Pressure contour along the central section of the computation domain parallel to the wind direction for Case-I (Black arrow shows the wind direction)

The pressure contour and velocity fields were computed to check the effects of boundaries and blockage ratio. Figure 3.6 shows the pressure contour for Case-I. This contour indicates that the initial conditions influenced by boundaries of the cube building. It should be noted that the reference pressure was set to 0 Pa at the inlet. Similar results were found for Case-II, Case-III and Case-IV. The pressure coefficient (C_p) plots, Figure 3.7, should be very close to each other. There are significant differences between Case-IV and Case-V on the front face. According to Abohela et al. (2013) and Richards and Hoxey (2001), the maximum pressure coefficient occurs close to 0.8 H from the ground. The position of maximum pressure coefficient (0.8 H) is close to that for the Case-V. It is also close to the position of maximum pressure coefficient for most of the cases. There are no obvious effects of boundaries and blockage ratio for Case-V. It can be argued that the Case-V has a sufficiently large domain, which does not affect the present results. Therefore, the Case-V was selected for the cube simulation.

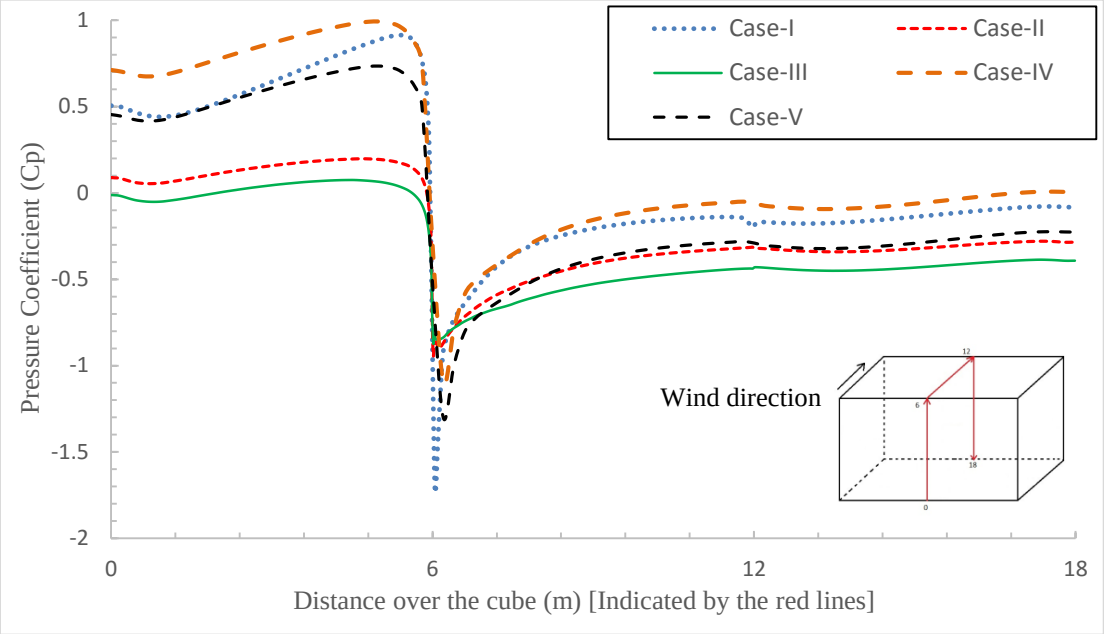

Figure 3.9: Pressure coefficient along the windward centreline over the cube (Indicated by the red line)

3.5.4 Mesh Independence

In this work, the hexahedral structured mesh was generated to discretize the computational domain using the OpenFOAM "blockMesh" tool. A tetrahedral unstructured mesh was constructed around the cube building using the "snappyHexMesh" tool (OpenFOAM (2014)). A further four cases were created namely, Case-VI, Case-VII, Case- VIII, Case-IX to check the mesh independence and compare the structured grid and unstructured mesh results using OpenFOAM CFD software. The mesh resolution (between two nodal points) for Case-VI was $0.33m, 0.25m$ for Case-VII (Case-VI and Case-VII are structured mesh) and $0.03125m$ for Case-VIII, $0.0156m$ for unstructured mesh Case-IX near the $6m \times 6m \times 6m$ cube. The mesh for Case-VII is shown in Figure 3.8. Note that the total cells of cases were shown in Table 3.3.

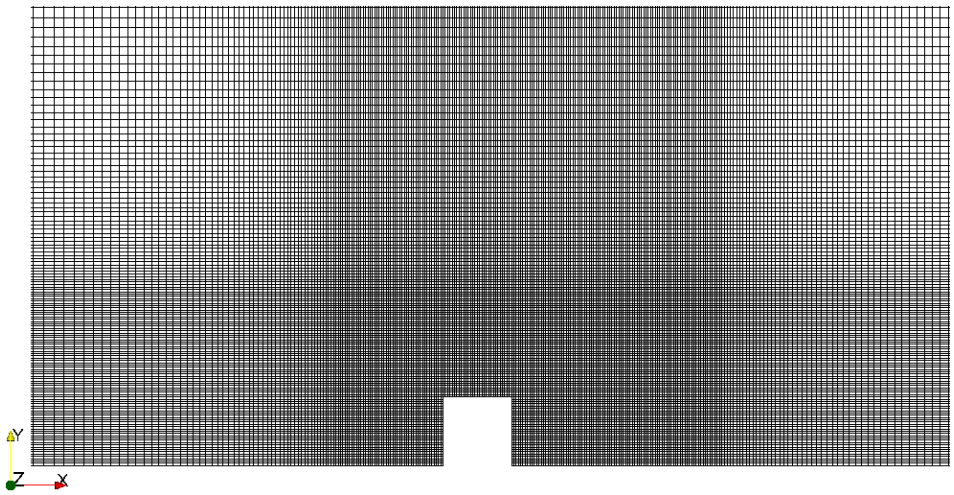

Figure 3.10: Mesh resolution around the cube for Case-VII

For grid convergence study, Richardson extrapolation (Richardson and Gaunt (1927)) is used to calculate a higher order estimate of the flow fields from a series of lower order discrete values $(f_1, f_2 \dots, f_n)$. This estimated value is the value that would results if the cell grid size tended to zero, $(h \to 0)$. The extrapolation is evaluated from the results of at least two different grid solutions. For the p^{th} order methods, Richardson extrapolation gives

$$f_{exact} \approx f_1 + \left[\frac{f_1 - f_2}{r^p - 1}\right] \tag{3.19}$$

Roache (1994), where the grid refinement ratio $(r = 2)$ is, the ratio of the cell area of two different grid refinements, constant in this research. f_1 (fine grid solution) and f_2 (coarse grid solution) are the flow field from two different grids. p is the order of accuracy.

In this study, $p = 2$ (second order accurate) is used to estimate the extrapolated value. The Grid Convergence Index (GCI) is a measure of convergence for grid refinement studies (Roache (1994)). It is based upon a grid refinement error estimator derived from the generalization of Richardson extrapolation. The GCI for the fine grid solution is defined as:

$$GCI_{i+1,i} = F_s \frac{|\varepsilon_{i+1,i}|}{f_i(r^p - 1)} \tag{3.20}$$

$$\varepsilon_{i+1,i} = f_{i+1} - f_i \tag{3.21}$$

where F_s is the safety factor and 1.25 for this study. To check the convergence error (accuracy of the solution), the simulation results on several different grids (Case-VI to Case-IX) were obtained to investigate the effect of grid independence. Table 3.4 summarizes the GCI values for the area-averaged pressure coefficient ($C_{p(avg)}$) for the roof of the cube for Case-VII, Case-VIII and Case-IX. From Table 3.4, the GCI ($GCI_{2,1}$) for finer grid is very low, indicating that the dependency of the solution on the cell size was reduced. And the GCI value was decreased with increasing the mesh resolution ($GCI_{3,2} > GCI_{2,1}$). Similarly, it can be said that the GCI value is high (less accuracy of the solution) for the other cases than $GCI_{2,1}$. Further refinement of the grid will not give much changes in the simulation results. For more detailed of the grid solutions, the results of different grids are compared to each other in Figures 3.11 and 3.12.

Table 3.4: Grid Convergence Index for three integration variables. Subscripts 3, 2 and 1 represent Case-VII, Case-VIII and Case-IX.

	$\varepsilon_{3,2}$	$\varepsilon_{2,1}$	p	$GCI_{3,2}$	$GCI_{2,1}$
$C_{p(avg)}$	9.96×10^{-3}	9.94×10^{-3}	2.0	0.906 %	0.886 %

Figure 3.9 shows the C_p results for all cases. The curves were found very similar. Very small discrepancies on the top of the roof were noticed in the C_p plot. Small differences were also found between the structured and unstructured grid solutions. The velocity profiles are shown in Figure 3.10 for the different cases (U_x is the velocity in the wind direction). These profiles are better agreement than the C_p plots. Thus, it can be concluded that the $0.03125m$ (32 nodes in every

metre near the cube) mesh resolution between two nodal points (Case-VIII) is sufficient for obtaining a mesh independence cube simulation.

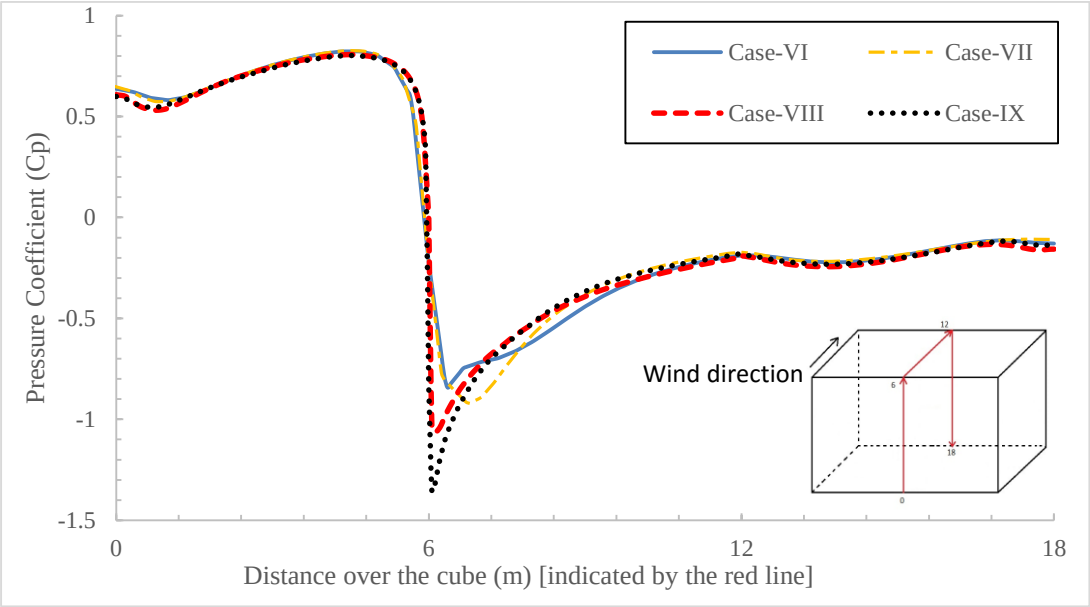

Figure 3.11: Pressure coefficient along the windward centreline over the cube building (Indicated by the red line)

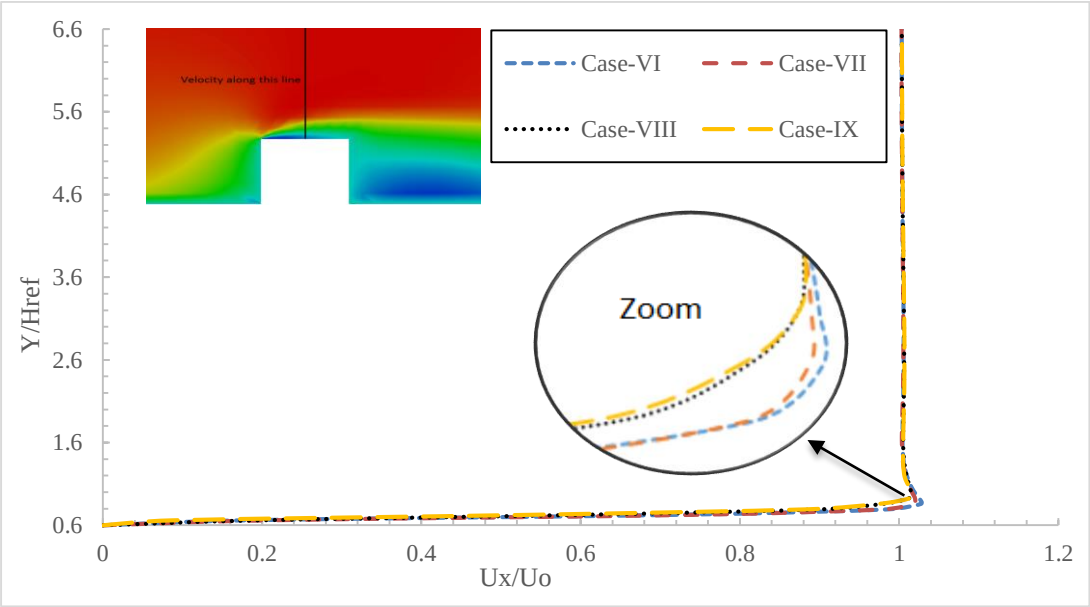

Figure 3.12: Velocity profiles at the indicated position (the centreline of the cube building)

3.6 Results and Comparison

In this section, the details of the flow simulation around the cube building are presented and compared with the previous experimental data to validate the OpenFOAM results. All the results are presented along the centerline of the cube parallel to the flow direction. The colour scale varies from figure to figure.

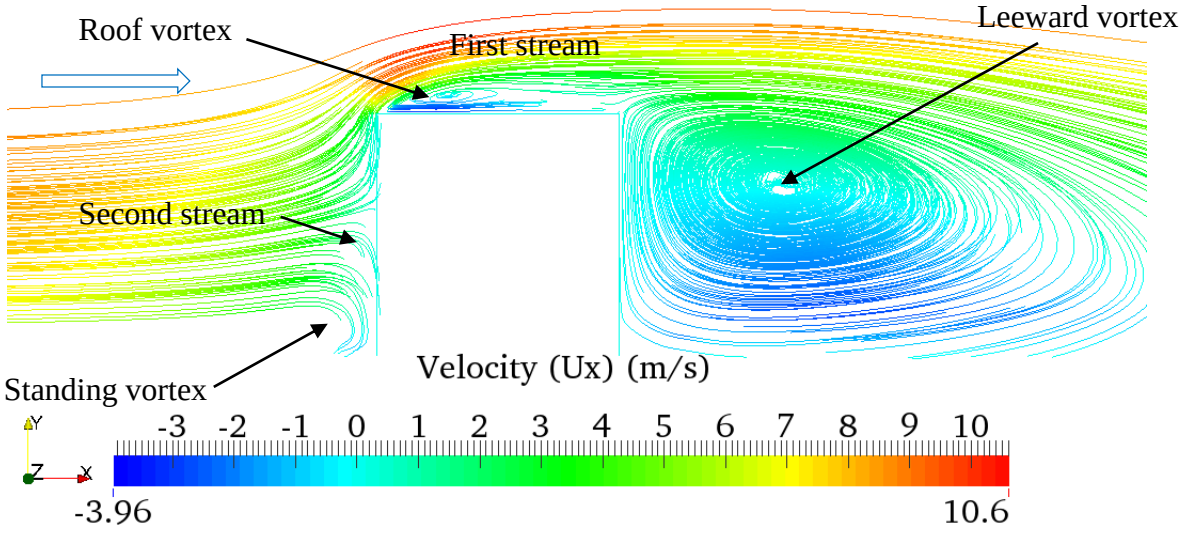

Figure 3.13: Streamlines over the cube (The central section of the cube parallel to the wind direction and blue arrow shows the wind direction)

Murakami and Mochida (1988) and Martinuzzi and Tropea (1993) examined the flow around a surface-mounted cube in a channel flow. They explained that as the flow approaches the cube building it deviates into four main streams: the first stream over the cube, second stream is directed down the front of the windward wall and other two streams are directed to the two sides of the cube. Figure 3.11 shows streamlines over the cube with the important flow features highlighted. The colour scale is shown for the velocity parallel to the wind direction. In the front of windward face, a standing vortex is formed. The present simulations show the correct features. The flow

separates upon hitting the windward roof edge of the cube and reattaches on the top of the roof. Due to flow separation and reattachment, recirculation areas were formed over the cube roof. The first stream also formed a vortex and reattached again in the leeward side.

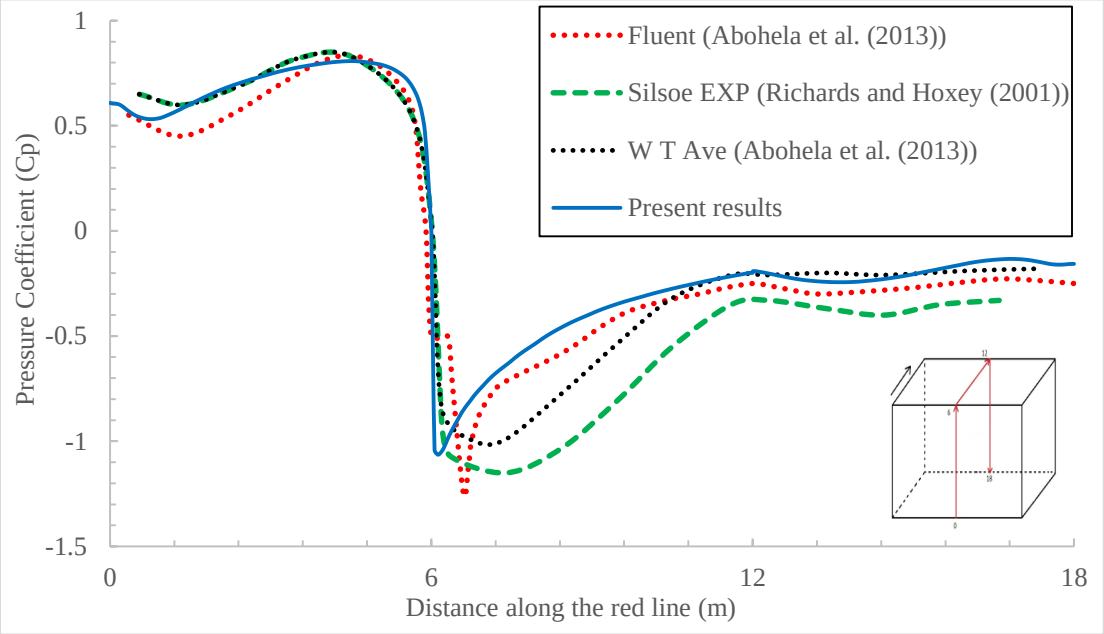

Figure 3.14: Pressure coefficient (C_p) over the cube at a mid-vertical section of the cube. The blue line is the present value, the green dotted line is the Silsoe Institute data (Richards and Hoxey (2001)), the red and black dotted lines are the CFD results-Fluent and the averaged wind tunnel data (Abohela et al. (2013)) [Black arrow shows the wind direction]

The comparison between the present results and previous works focused on the pressure coefficients because of available experimental and CFD results. Richards and Hoxey (2001) and Rodi (1997) observed that the maximum pressure occurred between $0.67\,H\ to\ 0.92\,H$ in most wind tunnel experiments. The maximum pressure coefficient (stagnation point) was calculated at 0.8 H, which falls in the measured range of 0.67 H to 0.92 H, on the windward face in this present cube simulation. In Figures 3.12 and 3.13, the pressure coefficient plots (C_p) are compared with

the averaged wind tunnel data (WT Ave), and the measurements of Castro and Robins (1977), the Silsoe field data, and Abohela et al. (2013) CFD simulation results. These plots are very close to each other except near the roof edge (around 8 m).

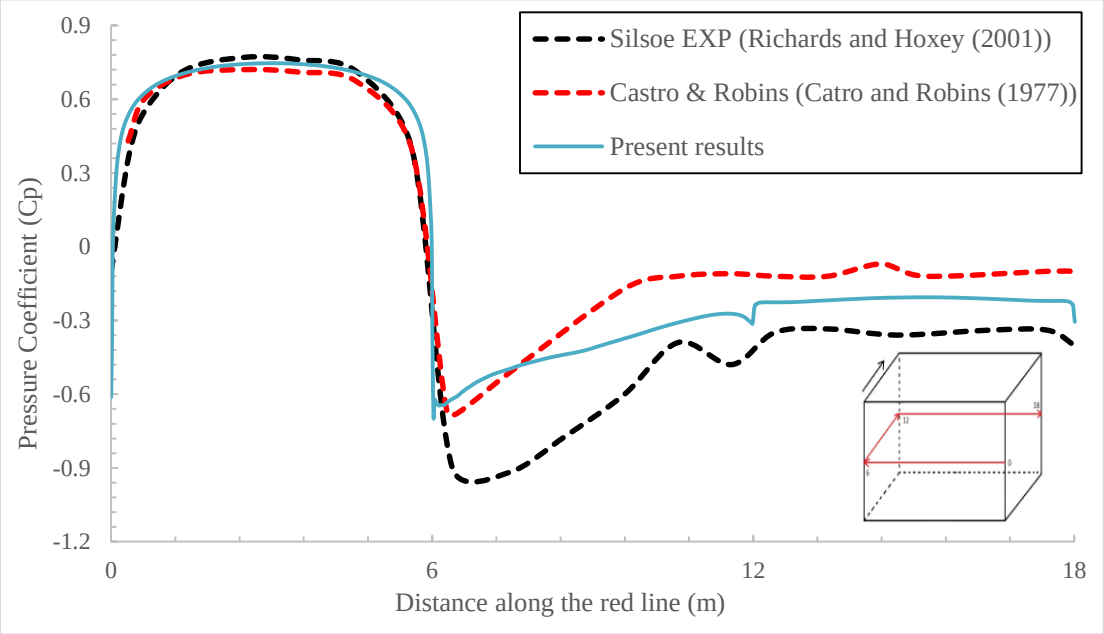

Figure 3.15: Pressure coefficient (C_p) around a cube at a mid-horizontal section of the cube. The blue line is the present value, the black dotted line is the Silsoe Institute data (Richards and Hoxey (2001)) and the red dotted line is the wind tunnel data of Castro and Robins (1977) [Black arrow shows the wind direction]

Most significant differences between experiments and CFD results occurred on the roof, but the basic shape of the C_p plots are similar. The minimum pressure coefficient was -1.07 on the centre of the roof edge. According to Rodi (1997), Abohela et al. (2013), the minimum pressure coefficient is between -0.85 to -1.56 near the roof edges for the cube building. These values vary from one turbulence model to another one. Therefore, it can be concluded that the present results are consistent with experimental data as they fall within the measured range of experimental

and other CFD results. In general, the CFD model can be applied for new simulations using OpenFOAM CFD software.

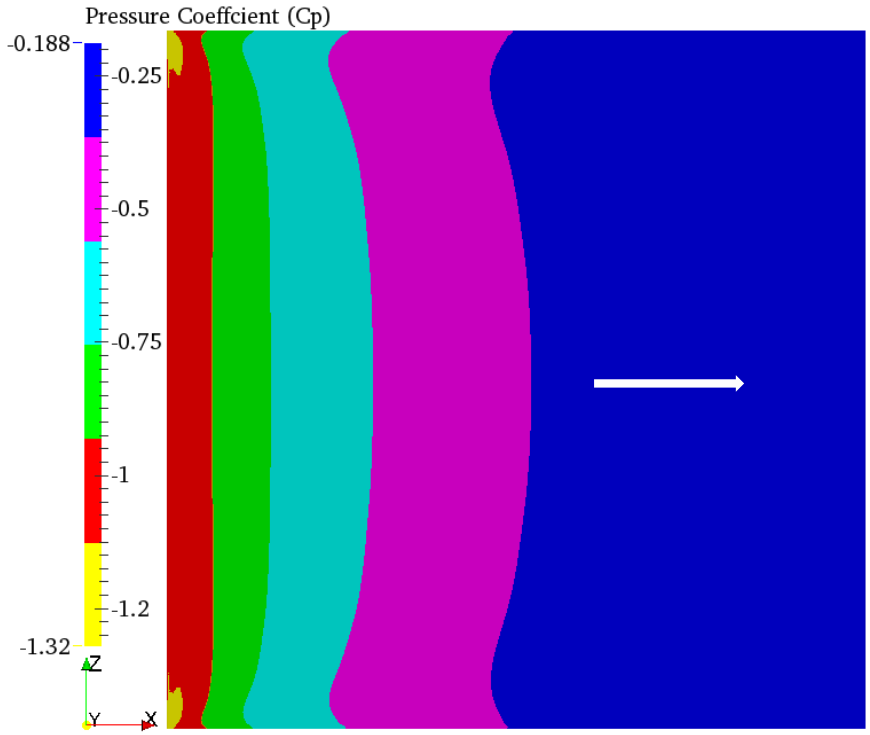

Figure 3.16: Pressure coefficient contour on the cube roof (White arrow shows the wind direction)

In addition, the pressure coefficient contours were calculated for the cube roof (Figure 3.14). Note that the colour scale varies from figure to figure. The minimum pressure coefficients (suction coefficient) were found at the windward edges and roof corners. Figure 3.15 shows the turbulent kinetic energy contour, where the maximum turbulent kinetic energy was $14\,\frac{m^2}{s^2}$ near the windward roof edge. Hence, it can be recommended that the near of the roof edges, corners should be avoided in locating PV modules for the cube building.

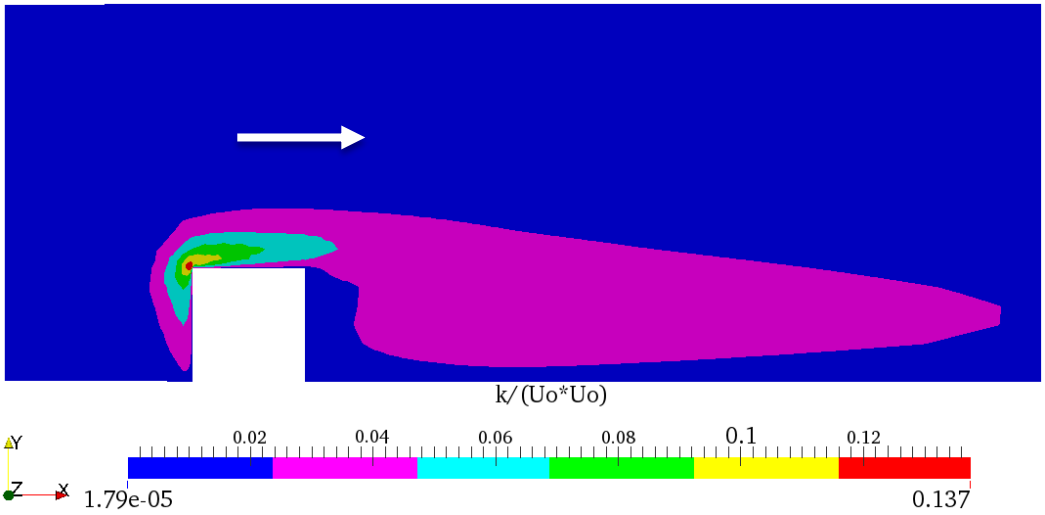

Figure 3.17: Turbulent kinetic energy contour though the vertical central plane of the computational domain (White arrow shows the wind direction)

3.7 Conclusion

To assess the CFD model, wind flow around the Silsoe cube building in the atmospheric boundary layer was investigated with several computational domains using the standard $k-\varepsilon$ turbulence model. The boundary and blockage ratio effects were checked using three cube building cases. Then, the mesh independence was checked with four different computational domains including structured and unstructured meshes. Finally, the present cube results were presented and compared with the previous experimental and other CFD results to assess the boundary conditions and numerical setup.

The present pressure coefficients were compared with wind tunnel tests, field data and CFD results. By analyzing and comparing with the previous experimental data, better agreement was found in the C_p plots than other CFD results (Figure 3.12 and Figure 3.13). The stagnation point

was at 0.8H, which falls in the measured range of 0.76H to 0.92H (Richards and Hoxey (2001), Abohela et al. (2013)). The minimum pressure coefficient was -1.07 at the cube edge and -1.32 at the cube corners, which also falls in the measured range (Rodi (1997), Abohela et al. (2013)). Therefore, it can be concluded that the present simulation of the flow over the cube building were consistent by comparing with the experimental and CFD (Fluent) results. The similar CFD model can now be used for Karoleena and Sprung building simulations with confidence that it will produce results with accuracy typical of similar simulations.

Chapter Four: **KAROLEENA BUILDING SIMULATION**

4.1 Introduction

The Karoleena building, Figure 1.2, is a low-rise building with a mono-slope roof. In this Chapter, the flow over the Karoleena building is investigated to examine the extreme wind load effects using the standard $k-\varepsilon$ turbulence model. In order to examine the extreme wind loads on the Karoleena building, a similar numerical procedure to the cube simulation is used to obtain consistent results. The present results are also compared with the general provisions of NBCC (2010) for the wind loads on mono-slope roof buildings. As explained in Chapter two, there is limited information for the extreme wind loads on this type of building. The analysis aims to provide wind loading data to minimize the structural cost of mounting PV modules to the Karoleena building.

The following objectives of the extreme wind load effects around the Karoleena building are explored.

- Investigate the extreme wind load effects around the Karoleena building for different wind directions
- Calculate the mean pressure distribution on the roof of the Karoleena building
- Compare between the present results and NBCC values for roof pressure coefficients
- Find the best location of PV modules on the roof, where the minimum wind load occurs than other location (s)

4.2 Wind Flow over the Karoleena Building

In this section, the numerical procedures are discussed in detail for the Karoleena building simulations. Then, wind flow over the Karoleena building is numerically simulated and presented in Section 4.3.

4.2.1 Boundary and Initial Conditions

In this Karoleena building simulation, the ground and Karoleena building are specified as a wall boundary condition and the top, front and back of the boundaries were slip boundaries. The log law profile is used at the inlet boundary for the mean wind and zero pressure gradient at outlet boundary. The boundary conditions are the same as for the cube building simulation, which was shown in Figure 3.2.

According to the Alberta Building Code (ABC (2010)), the extreme wind velocity is $28\,m/s$ in Calgary, AB, Canada. The maximum wind speed is set to $30\,m/s$ in this present work. The reference height of this velocity profile is assumed to be standard meteorological measurement height of $10\,m$ and the roughness length is set to $0.3\,m$ for many trees (Wood (2011)). The atmospheric boundary layer velocity and turbulent dissipation rate (ε) profiles have the same functional form as for the cube simulation (Equation (3.18)), but different in magnitude. These profiles provide the inlet conditions. The shear velocity (u_τ) was calculated $2.665\,m/s$ for the reference velocity ($30\,m/s$) and reference height ($10m$). Then, the turbulent kinetic energy (k) was calculated $23.677\,m^2s^{-2}$.

4.2.2 Numerical Methodology

First, three cases of the Karoleena building were created with different mesh resolutions in OpenFOAM CFD. Then, the results of these cases are compared for checking the mesh independence. Further, two Karoleena cases were created for simulating with different wind directions. The SIMPLE algorithm and SOR method were used to solve the set of algebraic equations. The relaxation factors (ω) are set to 0.3 for pressure and 0.7 for other variables (U, k and ε) and tolerance is 10^{-8}. For convergence, the initial residual controls are set to 10^{-4} for pressure and 10^{-7} for other variables. The convergence of the solution was checked by monitoring the residual of flow variables and the flow variables of a point in the domain.

4.2.3 Computational Domain

Figure 4.1 shows the Karoleena building geometry (right), provided by Karoleena Homes, with major dimensions. It is assumed the six PV modules would be installed at the middle of the roof, and the size of the PV module is $1.954 \times 0.982 \times 0.040m$ (Canadian Solar Company). The maximum building height (H) is $7.328m$ and the angle of the roof is 4.7°. This building was designed for an uneven ground, which is included in this simulation. Three different mesh resolutions (namely, Karoleen-1, Karoleena-2 and Karoleena-3) were created to investigate the grid independence. Table 4.1 shows the total number of cells for different cases. To avoid boundaries and blockage ratio effects, the boundaries of the computational domain used similar distances from the building as for the cube computational domain. The outlet boundary distance from leeward face of this building was made large (40H) to visualize the flow effects at far field (Figure 4.1 (left)).

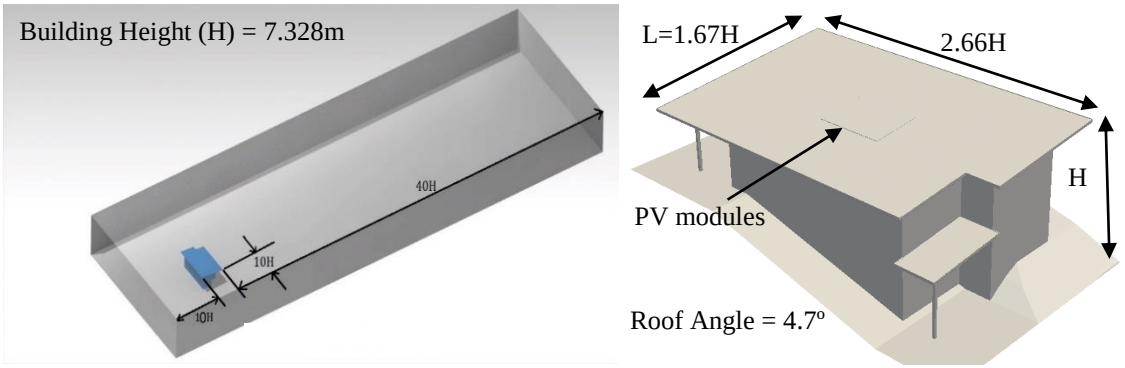

Figure 4.1: The computational domain with the Karoleena building (left) and detailed view of the Karoleena building (right) with major dimensions

Table 4.1: Karoleena building cases

Cases	Mesh resolution near the Karoleena building (m)	Total number of cells (million)
Karoleena-1	0.03	7.6
Karoleena-2	0.015	13.3
Karoleena-3	0.0075	37.8

4.2.4 Mesh Independence

A mesh independence test was carried out. For the Karoleena building simulation, similar blockage ratio and mesh resolutions (Table 4.1) were used as for the cube simulation. Thus, it can be said that the GCI calculations will be given similar values as for the cube simulation. For more detailed, the simulated velocity and pressure coefficient of the three cases were compared with each other. Similar agreement of the cube building simulation was noticed in the velocity profiles and pressure coefficient plots (Figures 4.2 and 4.3). Small differences occurred on the roof edges (top edges).

Therefore, it can be concluded that Karolineea-2 (0.015 m mesh) is sufficient to provide the simulation results that are reasonably grid independent.

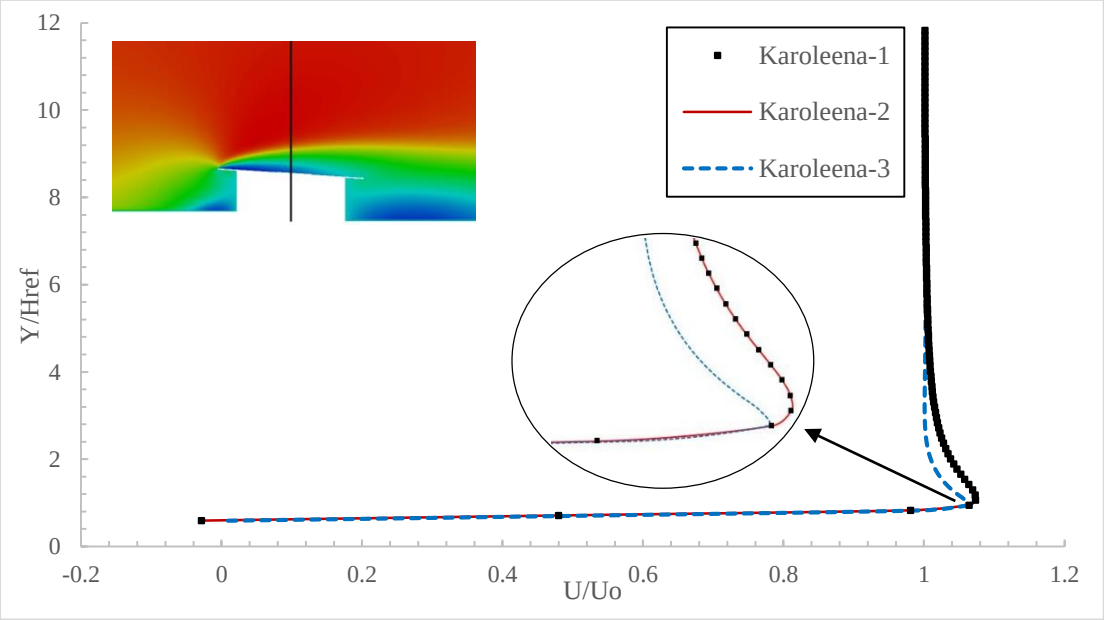

Figure 4.2: Velocity profiles along the indicated black line [Central section of the building (or computational domain) parallel to the wind direction]

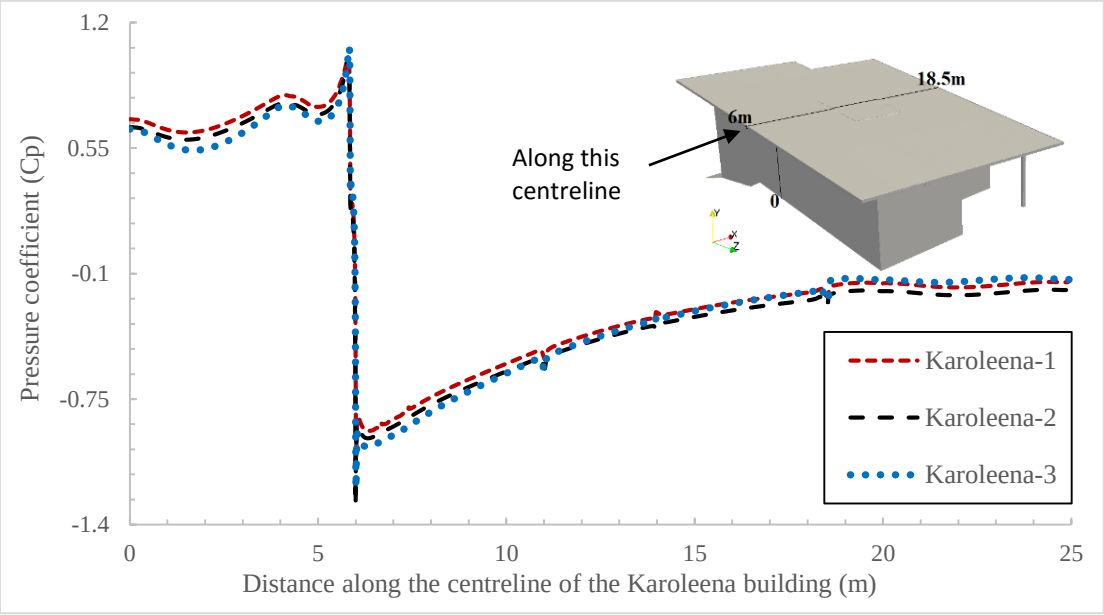

Figure 4.3: Pressure coefficient along the centreline over the Karoleena building

4.3 Results and Discussion

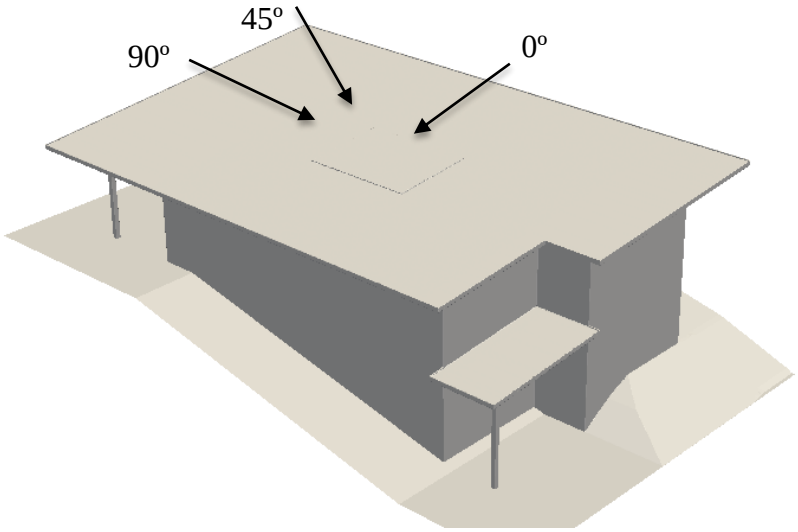

Figure 4.4: Karoleena building with wind directions

Simulations were carried out with different wind directions. The investigated wind directions are shown in Figure 4.4. The assumption is that the roof slope upward from the south to north is because this will miximize the PV output. The prevailing wind around Calgary is from the west so this will be taken as defining 0°. In the next sections, the flow variables around the Karoleena building are presented for the three wind directions. The pressure coefficients on the Karoleena roof are also compared with general wind provisions of the NBCC (2010). All the results are presented along the centreline of the computational domain parallel to the wind direction.

4.3.1 Wind Normal to the Karoleena Building Face (0º)

In Figure 4.5, the flow features are shown in detail. The colour scale is shown for U_x. As for the cube, the flow deviates four ways from the stagnation point. The upward flow separated from the top edge of the roof. Due to the flow separation, the roof vortex was formed. The flow reattached

on the top of the roof. The downward flow (Second stream) formed a standing vortex in the front of windward face. Due to the flow separation and reattachment, recirculation areas were formed at those locations. The flow also formed a vortex and reattached in the leeward side of the building.

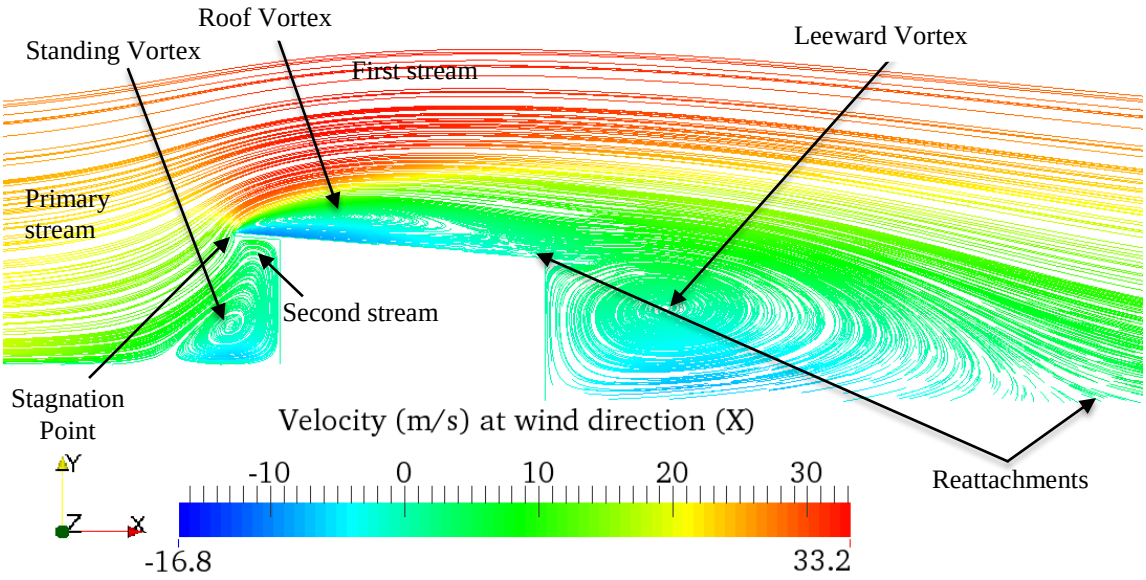

Figure 4.5: Streamlines passing through the vertical central plane (0° wind flow)

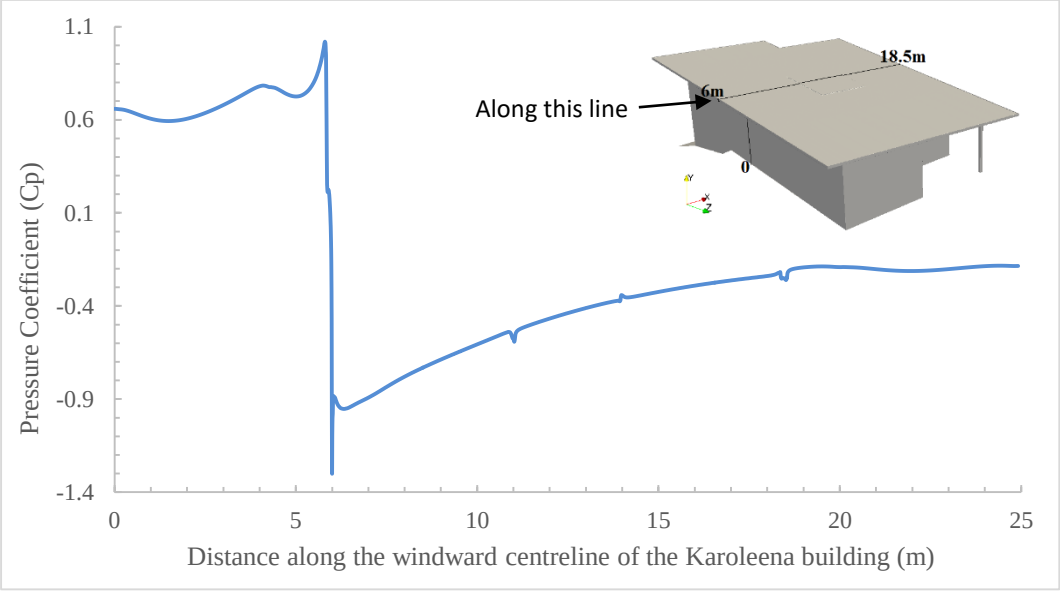

Figure 4.6: Pressure coefficient along the indicated line (The centreline section of the Karoleena building parallel to the wind direction) (0° flow)

The location of maximum mean pressure was near the lower edge of the roof on the windward wall. At this location (0.98H), the maximum pressure coefficient was 1.02, shown in Figure 4.6. In this plot, the pressure suddenly dropped at the windward edge of the roof (around 6m). Reynolds stresses are zero at a surface so it is unlikely to be due to turbulence model defects. In the middle of the roof (around 11 m and 14 m), the pressure coefficient is little changed by the PV modules.

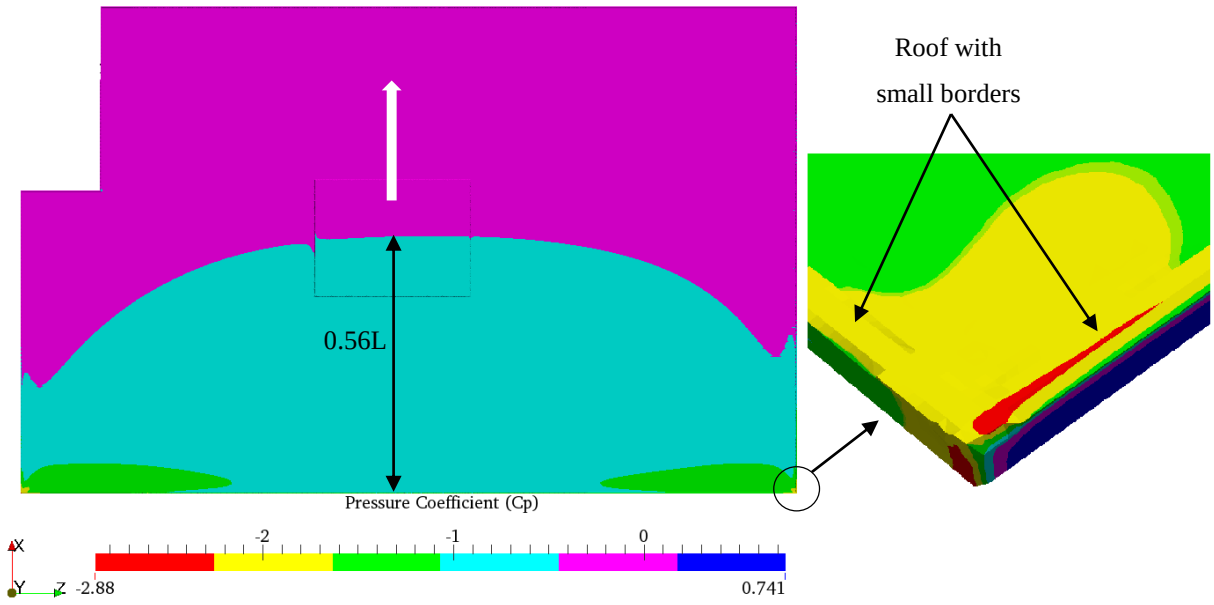

Figure 4.7: Pressure coefficient contour on the roof (White arrow shows the wind direction and black circle indicates zoom of roof's corner) (0° wind flow)

In Figure 4.7, the pressure coefficients for a corner of the roof are shown in the right side, where the minimum pressure coefficients near the edges and corners of the roof are indicated by the red and yellow coloured regions. The raised region is the PV modules, included in earlier simulation, in the centre of the roof. The minimum pressure coefficients were respectively, -1.82 and -2.88 (roof without and with small borders) at the roof corners. For this direction, the maximum length of the cyan region was approximately 0.56L from the windward face. Note that L is the total length of the Karoleena building along the wind direction, 12.2 m (Figure 4.1). In the magenta region,

the pressure coefficients vary from $-0.4\ to\ 0.2$ on the roof except near the roof edges and corners where the C_p is affected by the asymmetry of the building.

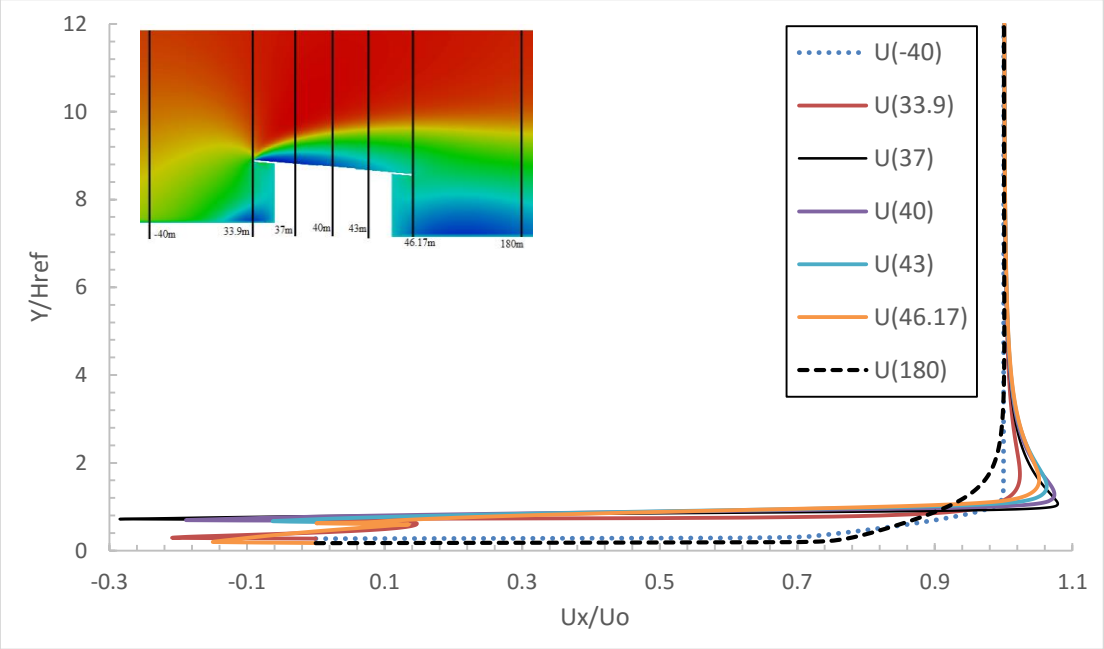

Figure 4.8a: Velocity profiles at the indicated locations for 0° flow [The origin for Y at -40 m and 180 m is different to the other locations and U_0 is the reference velocity $(30m/s)$. $U(-40), U(33.9)$ …. and $U(180)$ are the velocities (U_x) along the vertical lines at the indicated locations $(-40, 33.9, \ldots.$ and $180)$.]

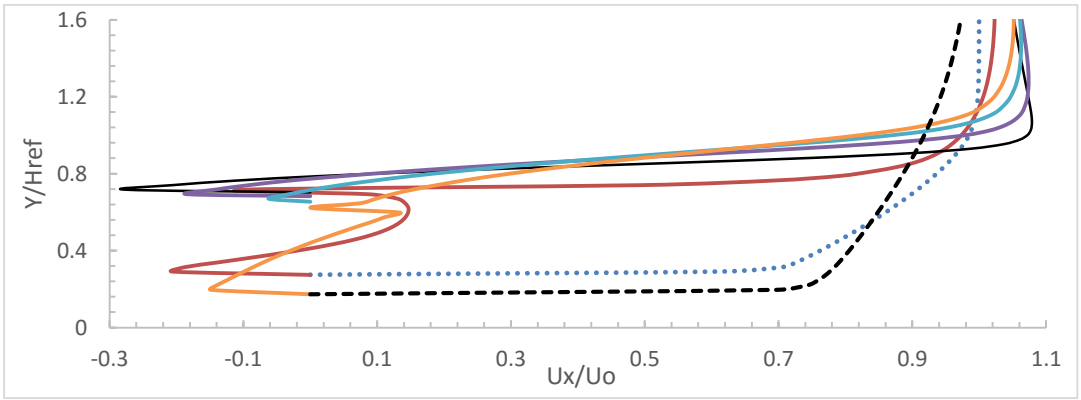

Figure 4.8b: Enlarged view of the lower part of Figure 4.8a (0°)

Figure 4.8a shows the wind speeds for different indicated locations, where U_x is the mean velocity in the wind direction (x axis). An enlarged view of region immediately above the roof is given in Figure 4.8b. Note that the velocity profiles start from different heights because of uneven ground (see Figure 4.4 or 4.18). Far away from the building, the velocity profile (black dotted line labelled U(180) in Figure 4.8) is very similar to the log law profile. Along the wind direction, the maximum velocity was $1.08U_0$ at 1.48H and 0.3L. This height (1.48H) of the maximum velocity falls in the simulated range of general CFD guidelines for most general buildings such as WINEUR (2007), Franke and Miles (2002).

In addition, the maximum value of k was 122 $\frac{m^2}{s^2}$ near the stagnation point (Figure 4.9). The second region of high k occurred above the roof after flow separation from the front of the roof. The maximum distance of the second region of high k was $y = 1.2H$ from the ground ($y = 0$).

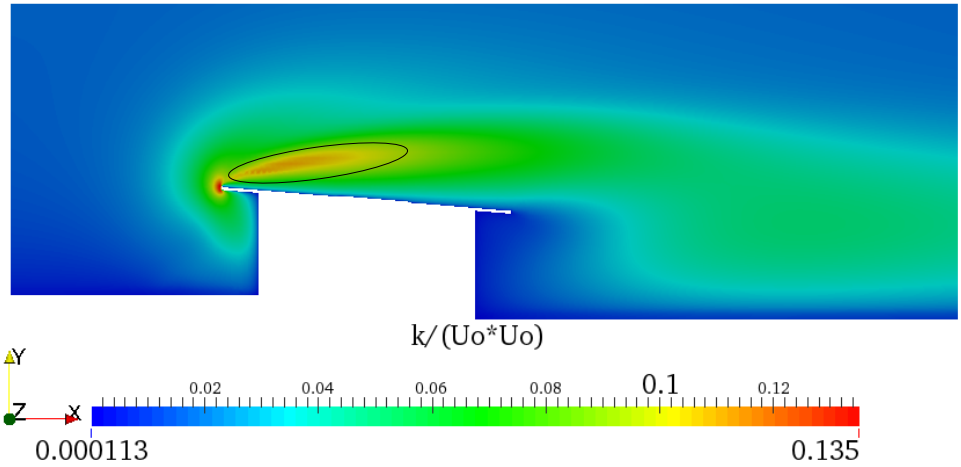

Figure 4.9: Turbulent kinetic energy contour $\left(k/{U_0}^2\right)$ (Oval indicates the second region of higher k and the x axis is the flow direction)

4.3.2 Wind at 45º and 90º

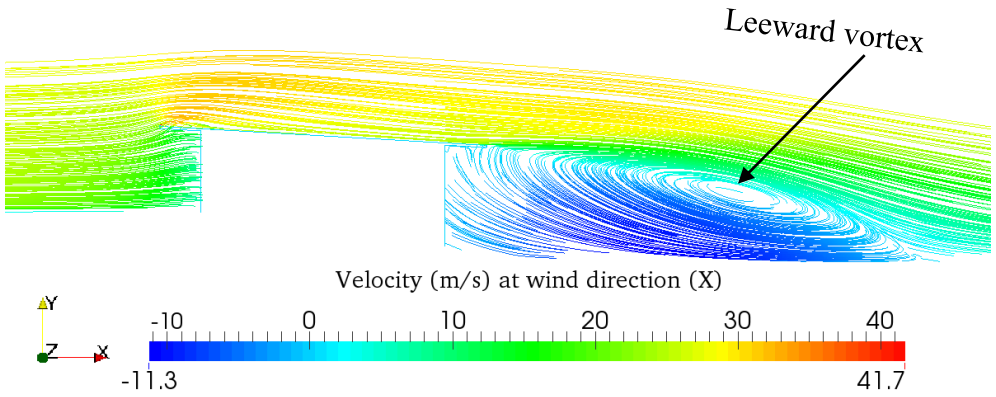

Figure 4.10: Streamlines passing through the vertical central section parallel to the wind direction (45º flow direction)

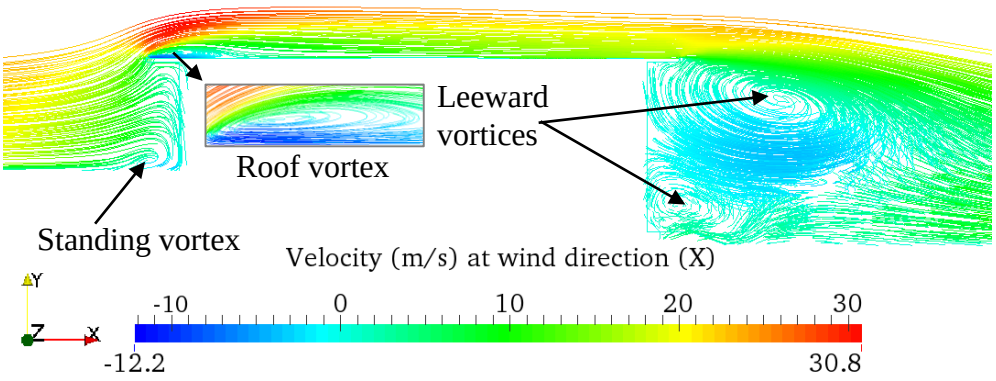

Figure 4.11: Streamlines passing through the vertical central section parallel to the wind direction (90º flow direction)

The streamlines for 45º wind direction (Figure 4.10) were substantially different from those for 0º. A standing vortex was not found in the front of the building. The length of the leeward vortex was larger than the 0º case. For 90º wind direction (Figure 4.11), the streamlines are similar to those for 0º case. The only quantitative difference between them is that there are two leeward vortices because of the building geometry effects particularly the uneven ground. It is clear that the flow

around a building is highly dependent on the orientation and geometry of the building. Note that the colour scale is shown for U_x.

Figure 4.12 shows the C_p plot over the Karoleena building for 45° wind flow. The pressure coefficient decreased significantly after the the roof corner (around 6.6m). Then, it only varied between -0.4 to -0.1 over the rest of the roof. This may due to a larger region of flow separation. It should be noted that the mean suction C_p (close to -1.5) for 45º flow over the cube was lower than the 0º case (close to -1.12) in the experiments of Castro and Robins (1977) and Richards and Hoxey (2001). For 90º, the C_p plot (Figure 4.13) had significant difference from the C_p plot for 0º flow epecially near the roof edge. The C_p was 1.34 near the roof edge (around 5.1 m). This is due to the higher stream velocity (accelerated velocity) than the reference velocity. The minimum C_p was -1.1 at the windward roof edge on the roof.

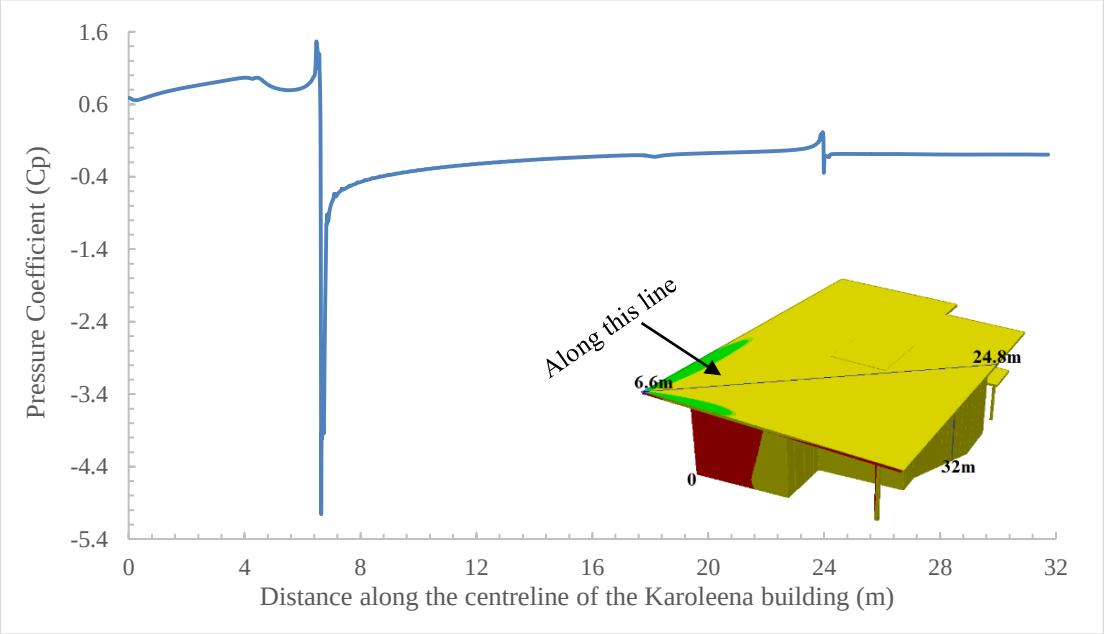

Figure 4.12: Pressure coefficient along the windward line over the Karoleena building (45º flow)

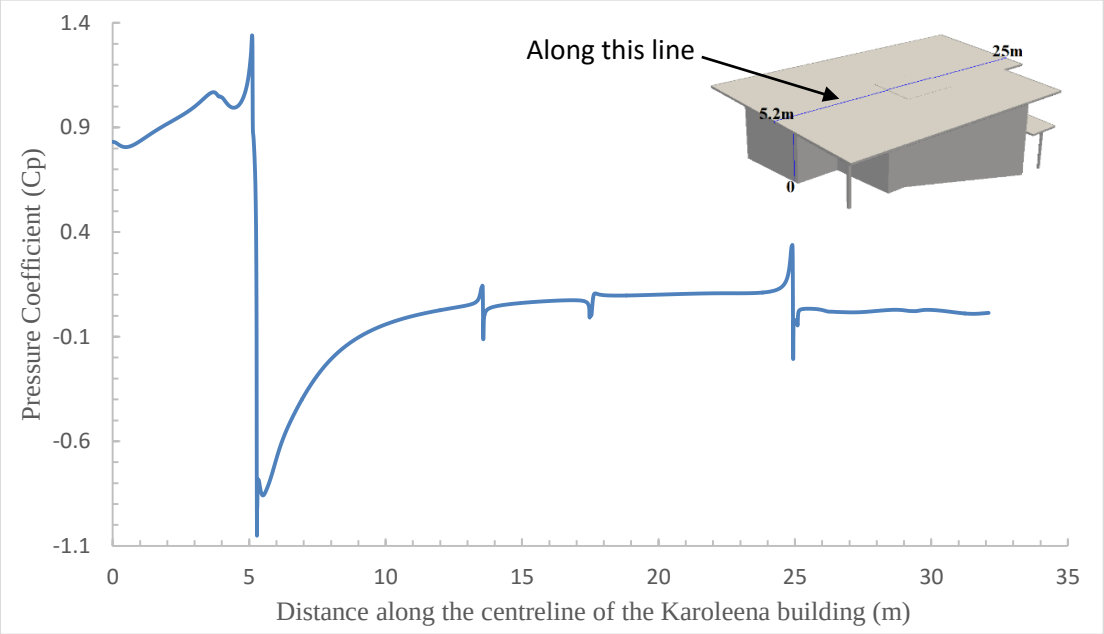

Figure 4.13: Pressure coefficient along the indicated line over the Karoleena building (90º flow)

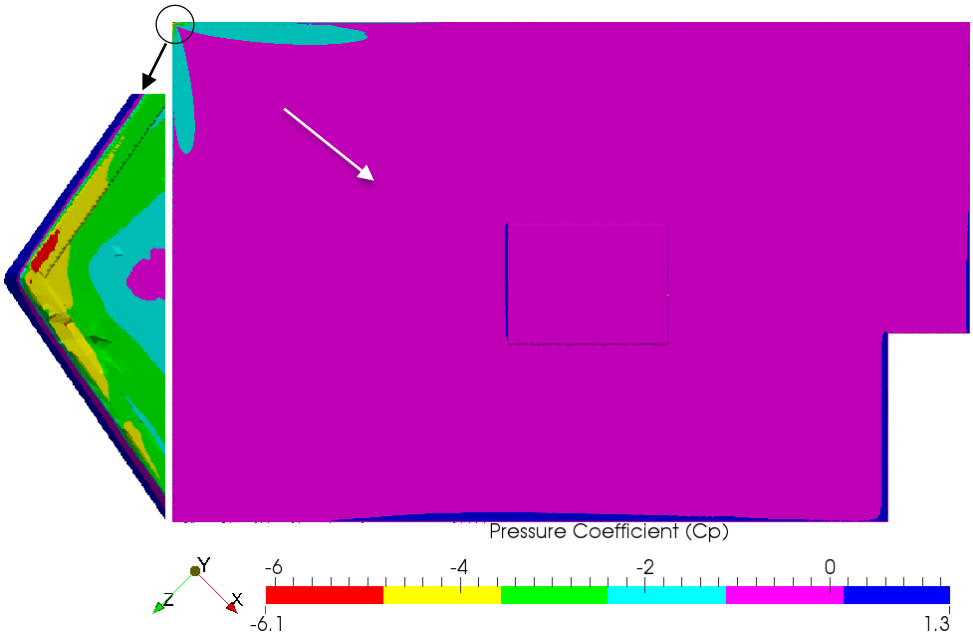

Figure 4.14: Pressure coefficient contour on the roof (White arrow shows the wind direction and black arrow shows the region of the roof's corner for expanded contour on the left) (45º flow)

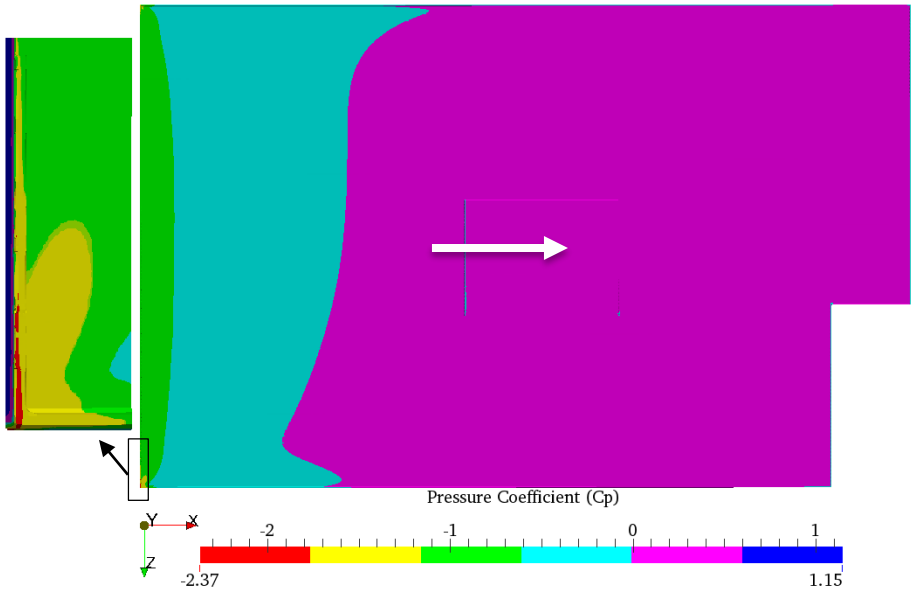

Figure 4.15: Pressure coefficient contour on the roof (White arrow shows the wind direction, black arrow shows zoom of roof's windward edge and circle shows highest lower C_p) (90º flow)

The C_p for an enlarged section of the roof's corner (left) is shown in Figure 4.14. The overall pressure coefficients are similar to those for 0º wind direction except at the roof edges and corners. The maximum C_p was 1.3. This is caused by separated streamlines generated by the building geometry. The stagnation streamline does not directly come from the inlet streamlines. Note that the C_p was calculated using equation (2.1). The C_p was very low at the roof edges, which may be due to the presence of the strong vortices and partly influenced by turbulence modeling defects. Figure 4.15 shows the C_p contours for 90° flow direction. In this contour, the cyan region are less than the 0º wind flow. But the C_p contour is close to the 0º flow. For the rest of the roof (magenta region), the C_p varies from $0\ to\ 0.6$ except near the roof edges and corners. The C_p was in the range of $-2.37\ to\ 1.15$. Note that the colour scale varies from figure to figure.

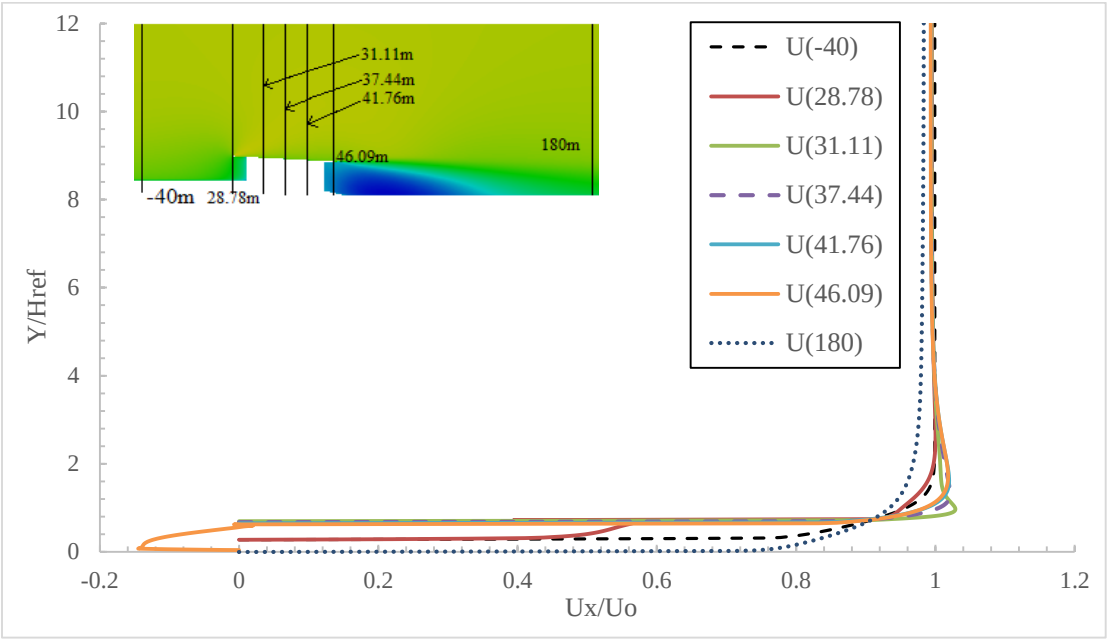

Figure 4.16a: Wind velocity (U_x) along indicated lines (45º) [The origin for Y at -40 m and 180 m is different to the other locations). $U(-40), U(33.9)$ …. and $U(180)$ are the velocities (U_x) along the vertical lines at the indicated locations $(-40, 33.9, \ldots. \text{and } 180)$.]

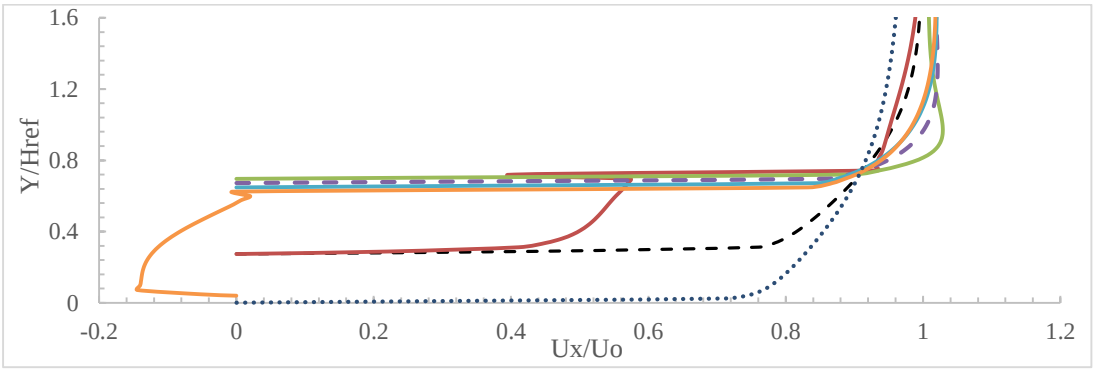

Figure 4.16b: Enlarged view of the lower part of Figure 4.16a (45º flow direction)

Moreover, the velocity plots are shown in Figures 4.16a and 4.16b for 45º wind direction. They are different from the velocity plots for 0º case in Figure 4.8. This is due to the larger recirculation region. The flow formed a smaller roof vortex than those for 0° and reattached. The maximum velocity was $1.39U_0$. Figures 4.17a and 4.17b show the velocity profiles for 90º wind direction.

In comparison to the velocity plots for 90° case, there is a significant difference between the U(-40) and U(180) profiles. This may be caused by the effects of vortices, generated by the building and uneven ground. For more detailed building geometry and the ground, Figure 4.18 is shown a cross-section view of the computational doamin for 90° flow direction. The maximum velocity was 2.6% higher from the reference velocity (U_0) at 1.26H for 90º.

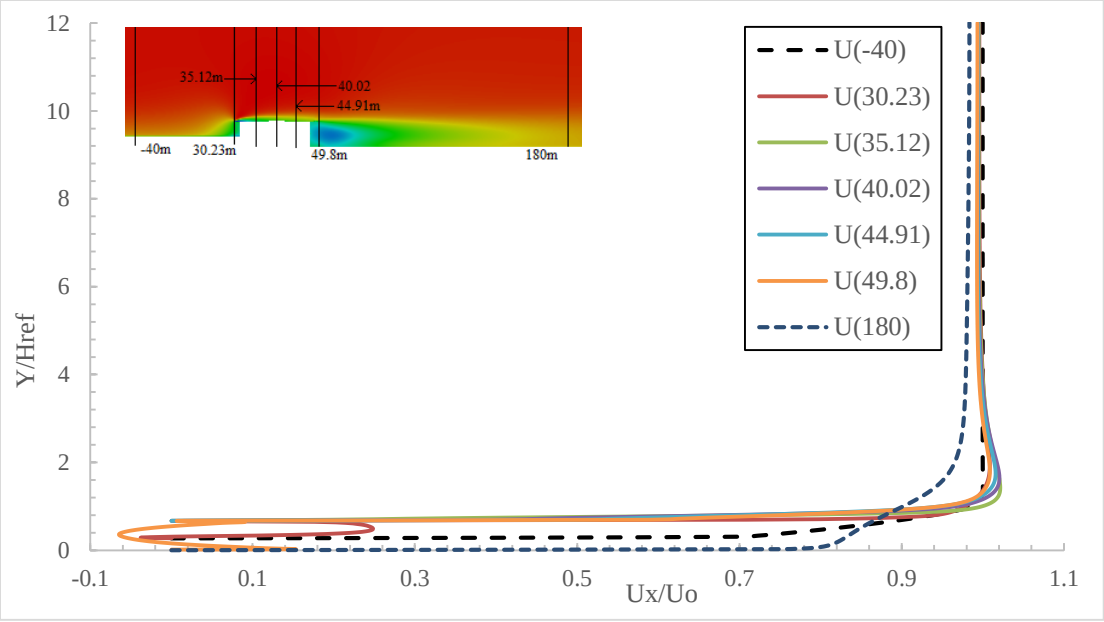

Figure 4.17a: Wind velocity profiles at indicated lines (90º) [The origin for Y at -40 m and 180 m is different to the other locations). $U(-40), U(33.9)$ …. and $U(180)$ are the velocities (U_x) along the vertical lines at the indicated locations $(-40, 33.9, \ldots . \text{and } 180)$.]

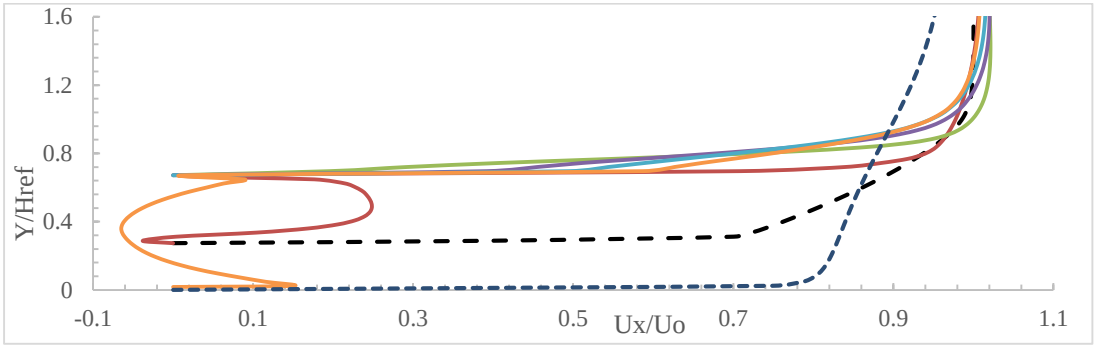

Figure 4.17b: Enlarged view of Figure 4.17b (90º)

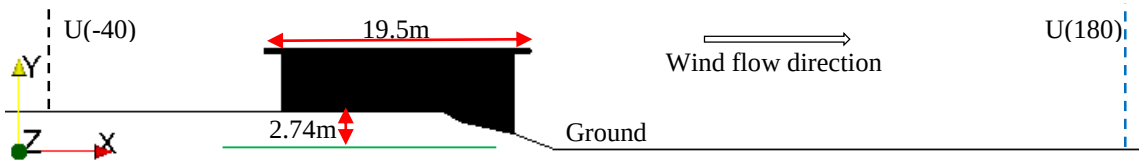

Figure 4.18: A cross-section view of the Karoleena building and the ground (90°)

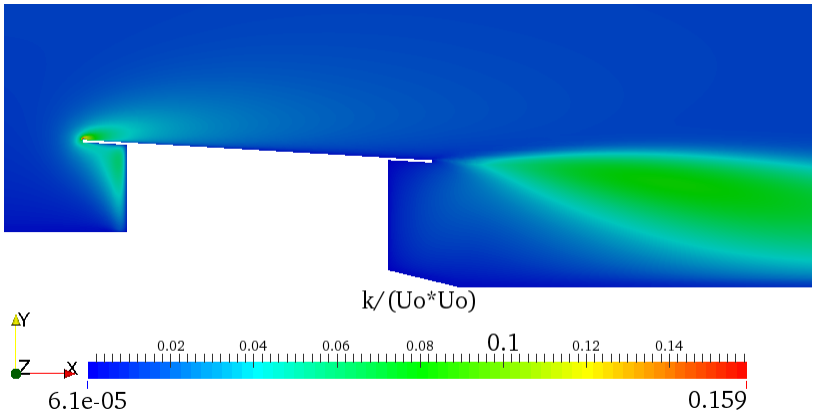

Figure 4.19: Turbulent kinetic energy contour $\left(k/{U_0}^2\right)$ (45º flow)

The k contour is shown for 45º in Figure 4.19, where the maximum value of k is less than other cases except near the roof corners and edges. The turbulent kinetic energy for other cases, including 90º (Figure 4.20), showed higher values near the stagnation point. The maximum value of k was 139 $\frac{m^2}{s^2}$ near the leading edge of the roof.

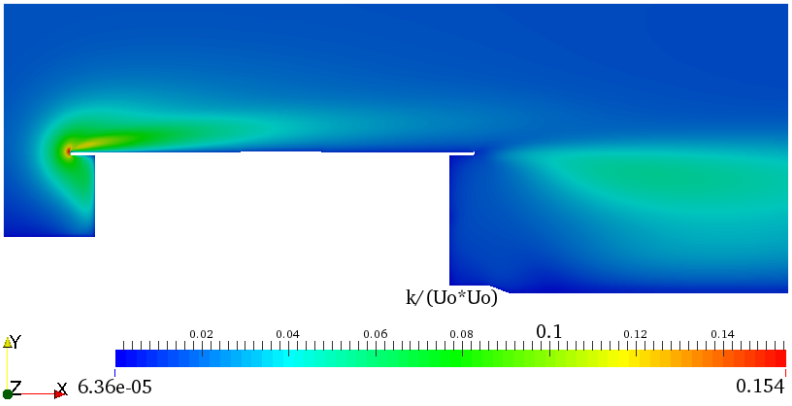

Figure 4.20: Turbulent kinetic energy contour $\left(k/{U_0}^2\right)$ (90º flow)

4.3.3 Comparison between the NBCC Specifications and Present results

Most critical regions (where the peak negative C_p occurs) were identified by following the NBCC (2010) instructions, are shown in Figure 4.21. $\mathrm{C}, \mathrm{C}', \mathrm{S}, \mathrm{S}'$ and R are the most critical regions (or zones) in the roof, the end-zone width (z) is not less than 4% of the least horizontal dimension of the roof or 1 m (NBCC (2010)) and θ is the roof angle. The Karoleena building is different from the generic NBCC (2010) mono-slope roof building shown in Figure 4.22. The NBCC (2010) provides the gust pressure coefficients ($C_{p(avg)}C_g$), obtained from a number of wind tunnel experiments and field data, for mono-slope roof buildings with roof angles $3° < \theta \leq 10°$. $C_{p(avg)}$ is the area averaged pressure coefficient for every critical region that is indicated in Figure 4.21. The gust factor (C_g) is the ratio of the peak wind speed to the mean wind speed. $C_g = 2.0$ as specified by NBCC is used to compare between the present numerical results and the NBCC specifications.

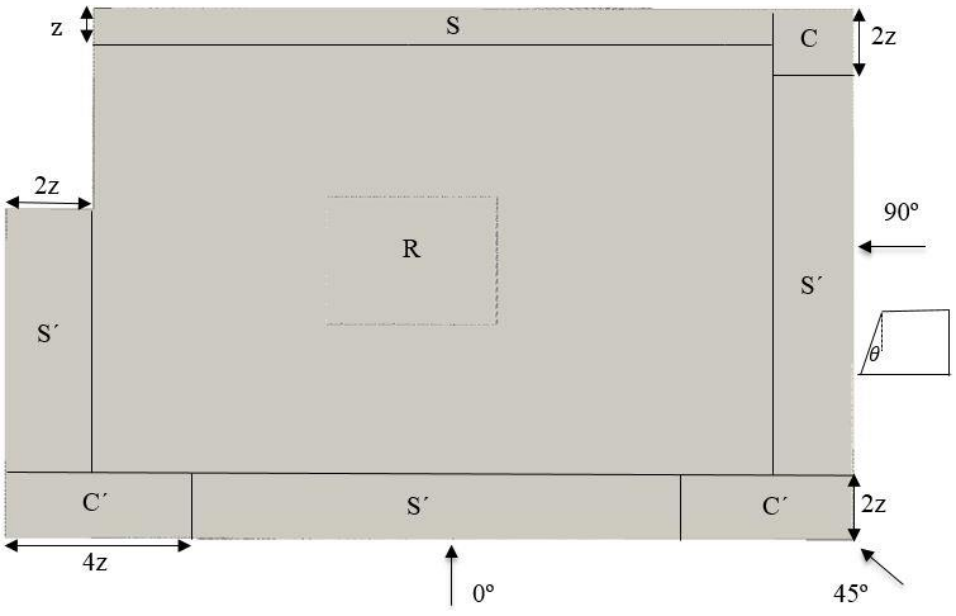

Figure 4.21: Critical regions on the roof (z = 1 m, is end-zone width and θ is 4.7º)

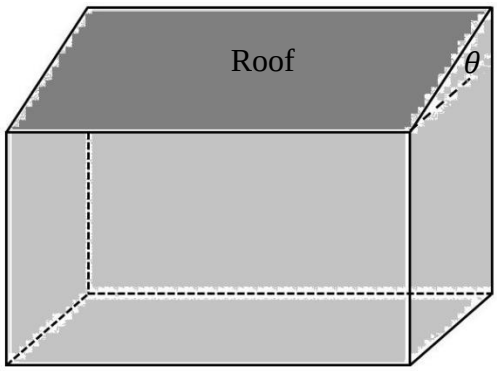

Figure 4.22: Hand drawing of the NBCC building with mono-slope roof [$3° < \theta \leq 10°$]

For each flow direction and every region, the area-averaged pressure coefficients ($C_{p(avg)}$) were calculated from the simulated results. Then, the worst negative $C_{p(avg)}$ was chosen for every region. Table 4.2 shows the comparison between the present results and the NBCC (2010) values for a simple mono-slope roof. From Table 4.2, the present values indicate similar trends to the NBCC (2010), but significant differences in magnitude. These results are significantly lower in magnitude than the NBCC values. Therefore, the present results suggest lower cost installations.

Table 4.2: NBCC Design pressure coefficients and the present pressure coefficients

NBCC Value		Present Value		
Zone	$C_{p(avg)}C_g$	Zone	$C_{p(avg)}$	$C_{p(avg)}C_g$
C´	-3.0	C´	-0.95	-1.9
S´	-3.0	S´	-0.88	-1.76
R	-2.0	R	-0.43	-0.86
C	-2.5	C	-0.55	-1.1
S	-2.5	S	-0.21	-0.42

To find the region of the extreme wind load on PV modules mounted on the roof, the roof was divided onto the zones shown in Figure 4.23. The area-averaged pressure coefficients were calculated for every zone for the three wind direction cases that are simulated. Then, the peak negative $C_{p(avg)}$ was chosen for every region from all wind directions and tabulated in Table 4.3. From Table 4.3, the suction averaged coefficients for first three locations (1, 2 and 3) are lower than -0.60 (the areas of low pressure), which indicates that the areas should be avoided when locating PV modules on the roof. The best locations were 7, 8 and 9, where the suction averaged coefficients are close to -0.30. Note that 6 PV modules (region 5) were placed for earlier simulations.

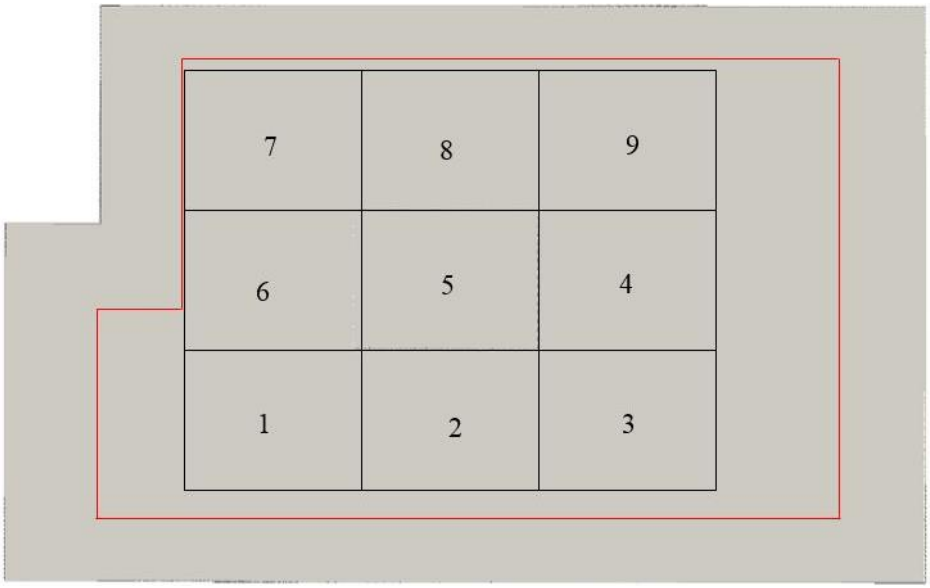

Figure 4.23: Possible locations of six PV modules on the Karoleena roof indicated by numbers. The red line indicates the boundary of critical regions.

Table 4.3: Pressure coefficients for possible locations

Location	1	2	3	4	5	6	7	8	9
$C_{p(avg)}$	-0.623	-0.64	-0.634	-0.43	-0.434	-0.4	-0.27	-0.3	-0.3

4.4 Conclusion

In this work, wind loads over the Karoleena building were estimated using the standard $k-\varepsilon$ turbulence model. Three simulations were used to check the mesh independence. Then, the flow over the building was calculated and presented for three different wind directions. The pressure coefficient plots and contours were discussed in detail by presenting Figures 4.6, 4.7, 4.12, 4.13, 4.14 and 4.15. The stagnation point was calculated at 0.98H for the wind direction at 0° that direction was defined in Figure 4.4. The velocity profiles were plotted for different locations (Figures 4.8, 4.16 and 4.17). Also, the present results were compared with the (NBCC (2010)) wind loading provisions for mono-slope roofs. The present $C_{p(avg)}$ values were shown in Table 4.2. These values had similar trends to the (NBCC (2010)) wind provisions. The present values were approximately found 30% less than the NBCC (2010) values.

To minimize the wind load on the Karoleena roof, the area-averaged pressure coefficients were calculated for possible locations (Figure 4.23). Table 4.3 shown the pressure coefficient results for those locations. The best locations were regions 7, 8 and 9, where the peak negative $C_{p(avg)}$ is close to -0.30. Note that 6 PV modules could be installed in every location. The first three locations (1, 2 and 3) had high suction $C_{p(avg)}$ (lower than -0.60). These areas should be avoided in placing PV modules. Therefore, it can be recommended that locations 7, 8 and 9 are the best and will minimize the cost of installing roof-mounted PV modules. It can also be concluded that the flow over the building is highly dependent on the building orientation and geometry.

Chapter Five: **SPRUNG BUILDING SIMULATION**

5.1 Introduction

In this chapter, wind flow over the Sprung building, which is a tent roof building (Figure 5.1 (left)), is investigated using OpenFOAM CFD. There are very few relevant researches in the literature as discussed in chapter two. It should be noted that there is no wind provision for this type of building in the NBCC (2010). In this research, the flow over the Sprung building is investigated using the standard $k-\varepsilon$ turbulence model to obtain mean flow and turbulence for different wind directions. The numerical procedure, mesh independence and the simulated results are discussed in detail in a similar way of the Karoleena building simulation. The main purpose of this building simulation is to predict the flow fields around the gable of the roof for analysis of the performance of a wind turbine (Figure 5.1 (right)) mounted along the gable.

The following objectives of the Sprung building simulation are explored:

- Investigate the flow over the full scaled Sprung building for different wind directions
- Determine the velocity fields and turbulent kinetic energy around the Sprung building for all wind directions
- Predict the flow field along the gable of the roof for future analysis of the turbine performance
- Compare between the present results and field data

5.2 Wind Flow over the Sprung Building

In this section, a systematic numerical procedure is followed for wind modeling over the Sprung building as for the Karoleena simulation. The numerical procedure and calculation for the Sprung building are discussed in detail.

5.2.1 Numerical Methodology

The standard $k-\varepsilon$ turbulence model is used to obtain the mean flow and turbulence, similar to that done for the Karoleena building. The boundary and initial conditions are the same as used for the Karoleena building simulation (Figure 3.2). Similar profiles of velocity and turbulent dissipation rate were applied at the inlet (Figure 4.1). Note that the reference velocity was $30\,\frac{m}{s}$, which is the same as used in previous Chapter. The SIMPLE algorithm and SOR method are used with the same relaxation factors. The convergence of the numerical solution was checked by monitoring residuals and the flow variables of a point in the computational domain.

5.2.2 Computational Domain

The geometry of the Sprung building, which was provided by Sprung, is shown in Figure 5.1 (left), where $H = 8.7m$ is the building height, $L = 2.45H$ is the horizontal length and $W = 4.92H$ is the width of the building. The wind turbine is fixed along the gable shown in Figure 5.1 (right), but it is not included in this building simulation. The ground around this building was assumed to be flat and of uniform roughness. With different mesh resolutions, three computational domains were created with the full scaled building: Sprung-1, Sprung-2 and Sprung-3. Sprung-1 is shown the

mesh resolution near the Sprung building in Figure 5.2. The mesh resolution near the building and total cell count are given in Table 5.1. Further, three computational domains were created for different wind directions (see Figure 5.5). From the building, the boundary distances were maintained similar of the Karoleena building simulation. The blockage ratio was less than 3% for all cases.

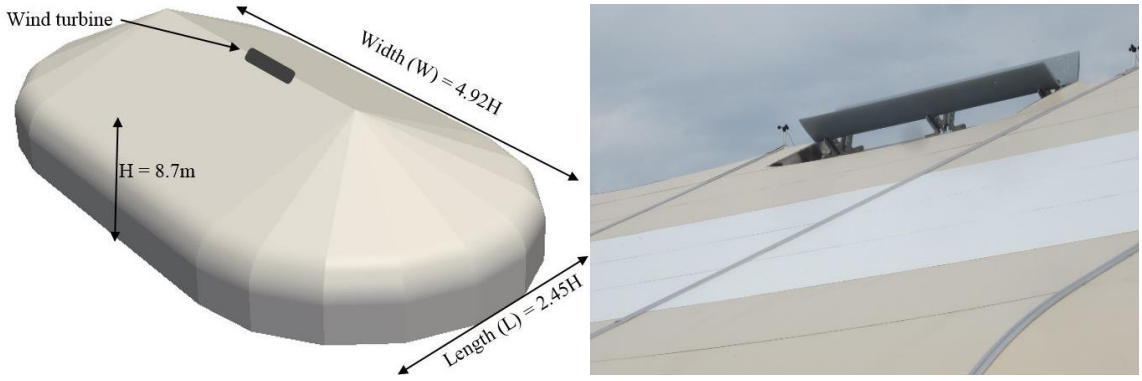

Figure 5.1: Sprung building with major dimensions (Left) and a picture of the wind turbine (right) [Photo provided by Ron Hockin, Sprung Instant Structures Ltd.]

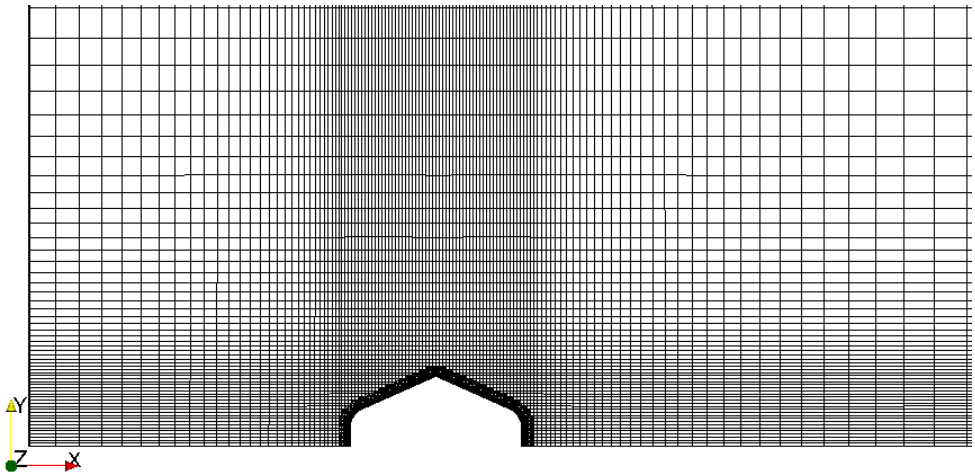

Figure 5.2: Mesh resolution of a computational domain (Sprung-1)

Table 5.1: Sprung building cases

Cases	Mesh resolution near Sprung building (m)	Total cell count
Sprung-1	0.3	5.6 million
Sprung-2	0.15	17.5 million
Sprung-3	0.075	64.8 million

5.2.3 Mesh Independence

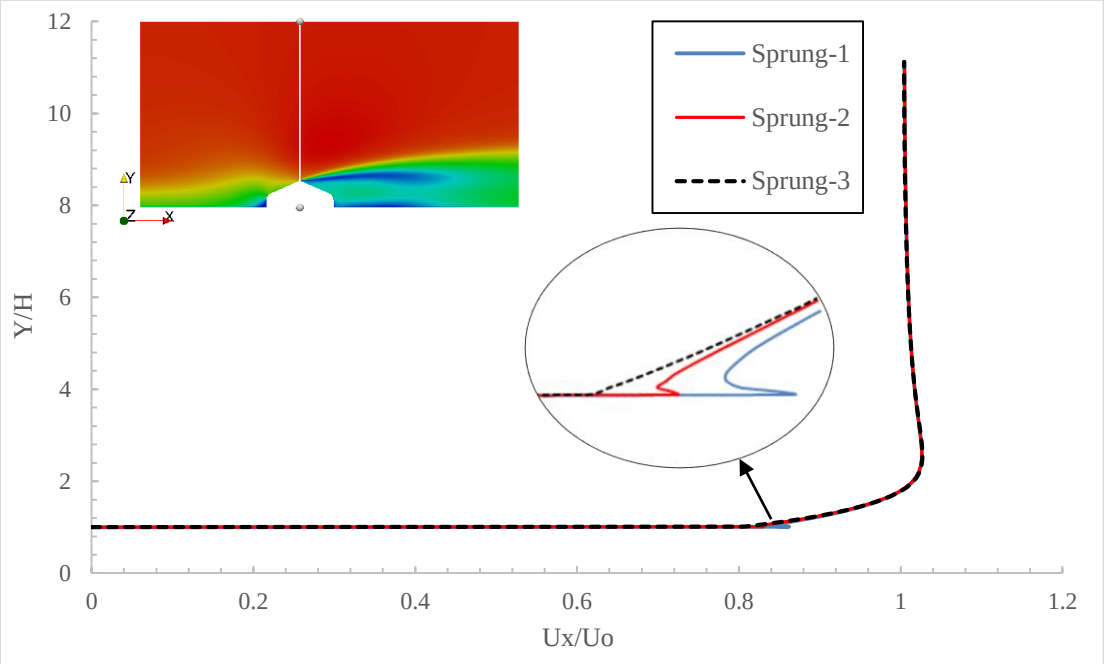

Figure 5.3: Wind velocity profile along the indicated white line

All presented results are along the centreline of the building parallel to the wind direction. The three different meshes are compared to check the dependence of flow variables (i.e. velocity, pressure) on the grid. The velocity and pressure coefficient plots are shown in Figures 5.3 and 5.4. There is little difference between the results from the three meshes, but there are small differences

near the apex of the roof. For the Sprung building, it can be reasonably sure that the GCI calculations will be given lower values (less grid convergence error) than the cube and Karoleena building cases. Because the velocity and C_p curves were very close to each other than the other building cases. Therefore, it was concluded that the Sprung-2 mesh was a good balance between high cell count and ease of post-processing. Note that it is very difficult to visualize and extract the data from Sprung-3 because of the high number of cells.

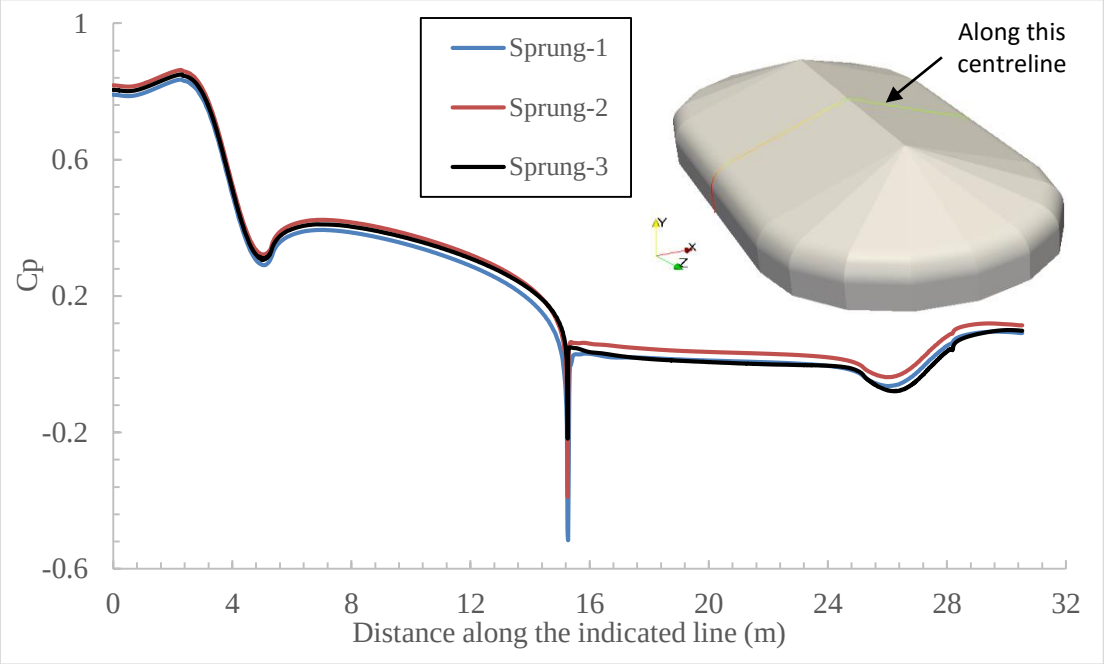

Figure 5.4: Pressure coefficient along the centreline over the Sprung building

5.3 Results and Discussion

In this section, the wind flow over the Sprung building is investigated and presented for different wind directions. The simulated results are mainly focused on the velocity fields. The investigated wind directions are shown in Figure 5.5, where 0° wind direction is perpendicular to the main axis of the building, i.e. along the x axis defined in Figure 5.2.

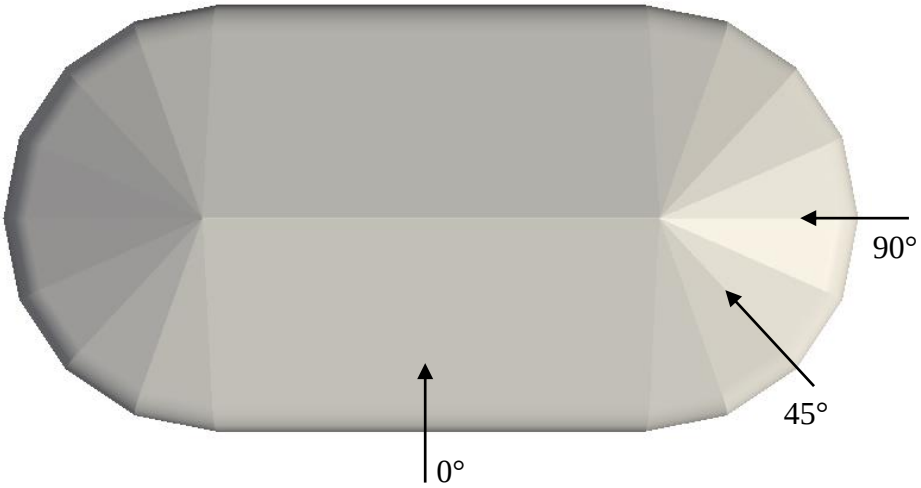

Figure 5.5: Investigated wind directions (Top view of the building)

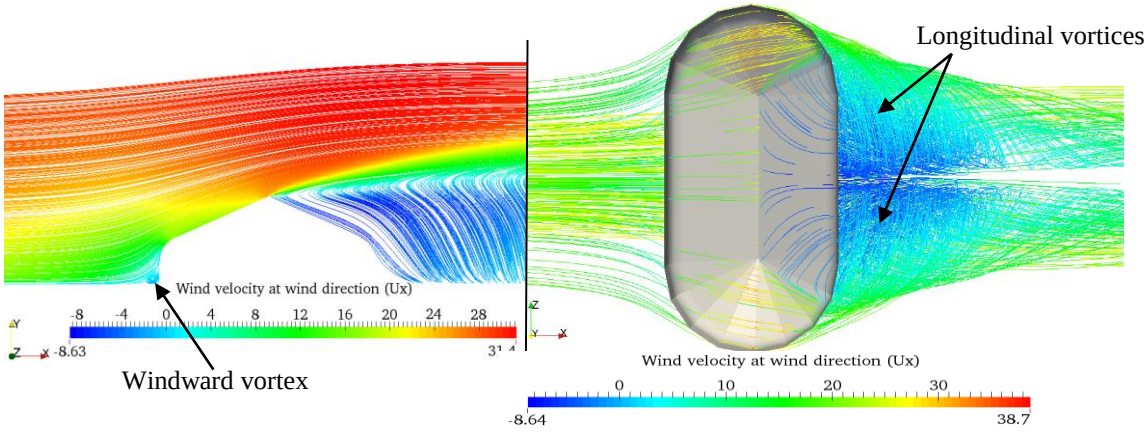

Figure 5.6: Streamlines around the Sprung building (along the central section of the building parallel to the wind direction (left) and bottom view (right)) for 0° flow

As discussed in previous chapters, the flow around the building is highly dependent on the orientation and geometry of the building. The dependence on direction was also found in this building simulation. The windward vortex was formed in the front of the building in this simulation (Figure 5.6). In the leeward side, the flow formed two longitudinal vortices. These vortices are anti-symmetric, as shown in Figure 5.6. Note that the values of the colour legend are different from

figure to figure. As previously, the x axis is the wind direction and y axis is the vertical coordinate (height) for all simulations. Streamlines around the building are shown below for 45° and 90° wind directions in Figures 5.7 and 5.8. The colour scales are shown for U_x.

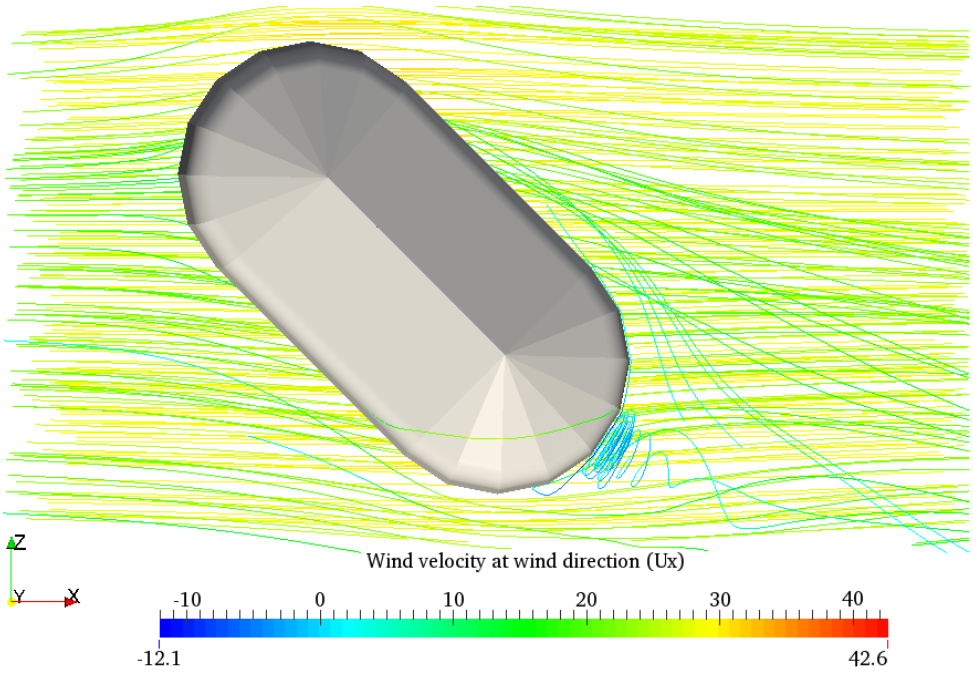

Figure 5.7: Streamlines around the Sprung building for 45° flow (Bottom view)

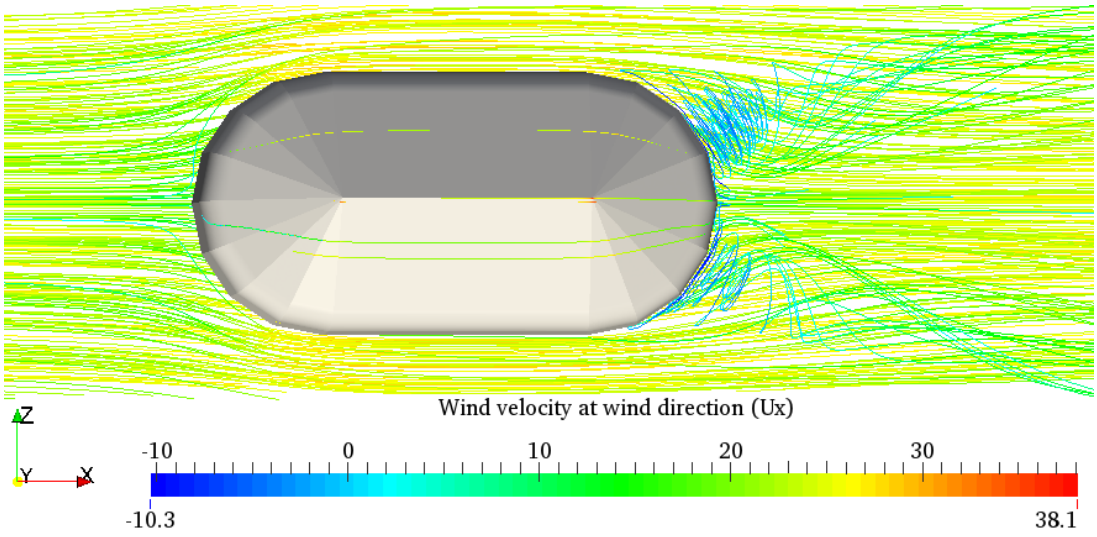

Figure 5.8: Streamlines around the Sprung building for 90° flow (Bottom view)

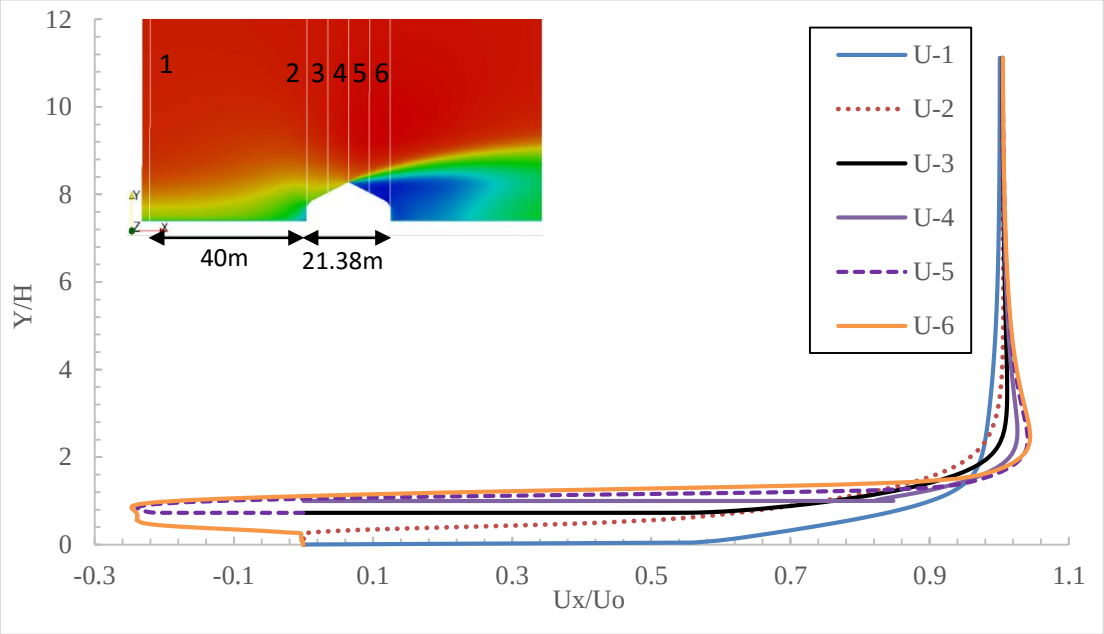

Figure 5.9: Velocity profiles along the indicated white lines (0° flow) [The central ($z = 0$) section of the building parallel to the wind direction. U-1, U-2, …. and U-6 are the velocities (U_x) along the vertical lines at those indicated locations.]

The velocity profiles are plotted for different locations by taking a central section of the computational domain parallel to the wind direction at $z = 0$. Figure 5.9 shows the velocity profiles along the indicated white lines. The horizontal distance between locations (2, 3, 4, 5 and 6) are all 5.35 m. From these plots, U-5 and U-6 profiles indicate that the recirculation occurred on the roof of the leeward side. For this vertical section of the computational domain, the maximum velocity was $1.05U_0$ at $y = 2.47H$ and $x = 0.94L$. Note that L is was defined in Figure 5.1.

For the 45° wind flow, Figure 5.10 shows velocity profiles at different locations. The maximum velocity was somewhat higher near the gable of the roof ($1.77U_0$) [U-4 profile]. In the 90° case,

there was no vortex on the roof or at the front of the building (Figures 5.11). The maximum velocity was found near the gable of the roof ($1.28U_0$) [U-5 profile].

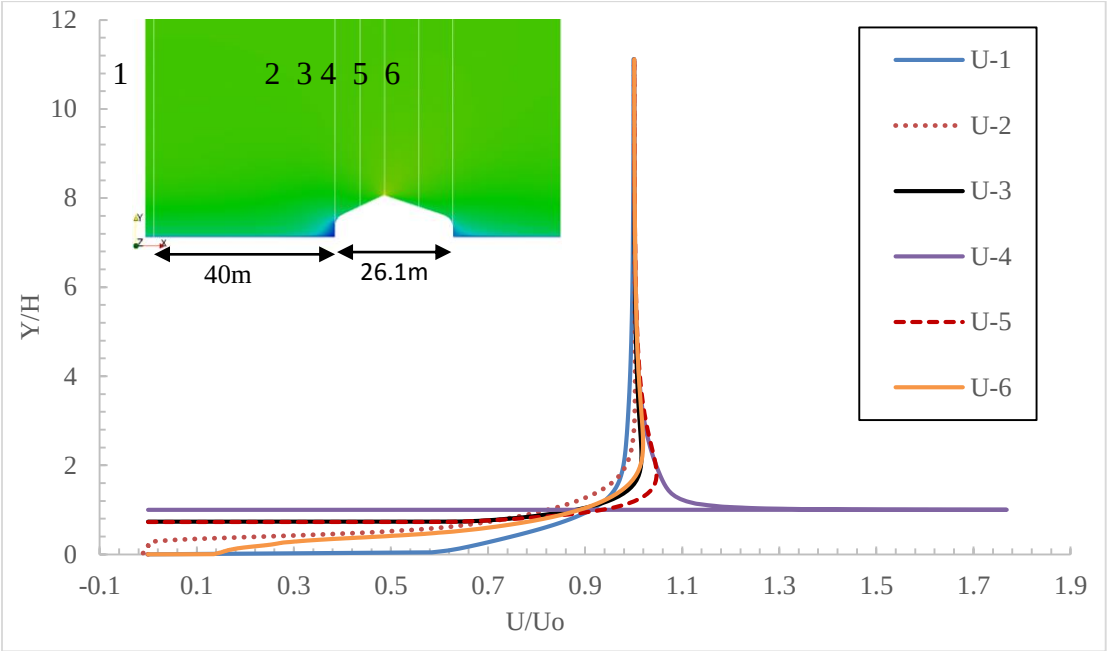

Figure 5.10: Velocity profiles along the indicated white lines (45° flow)

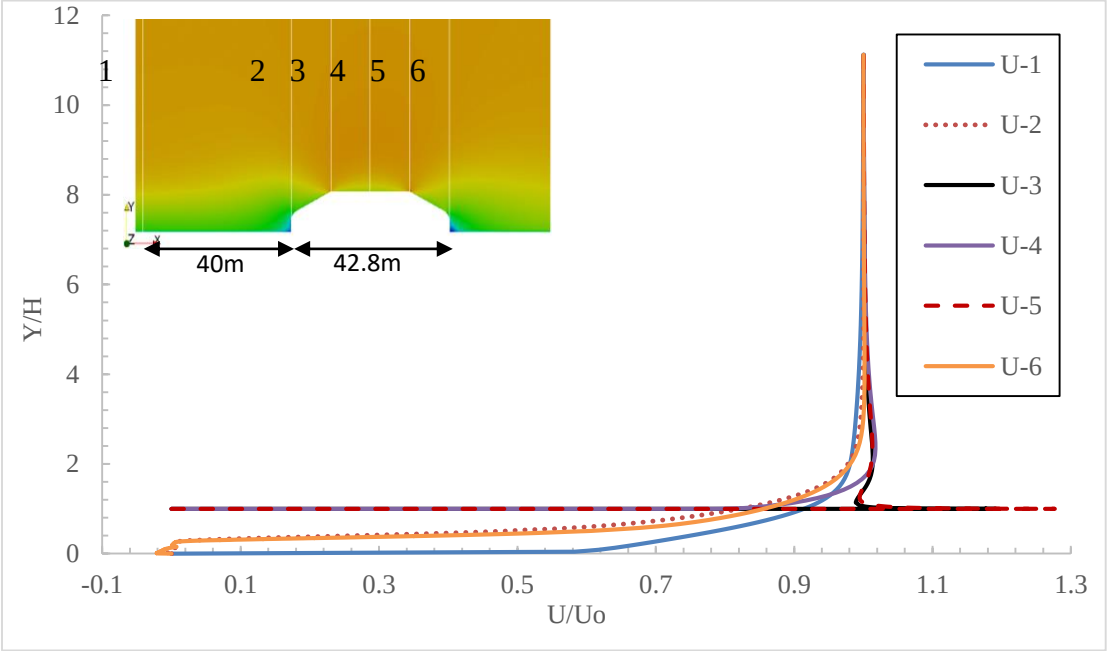

Figure 5.11: Velocity profiles along the indicated white lines (90° flow)

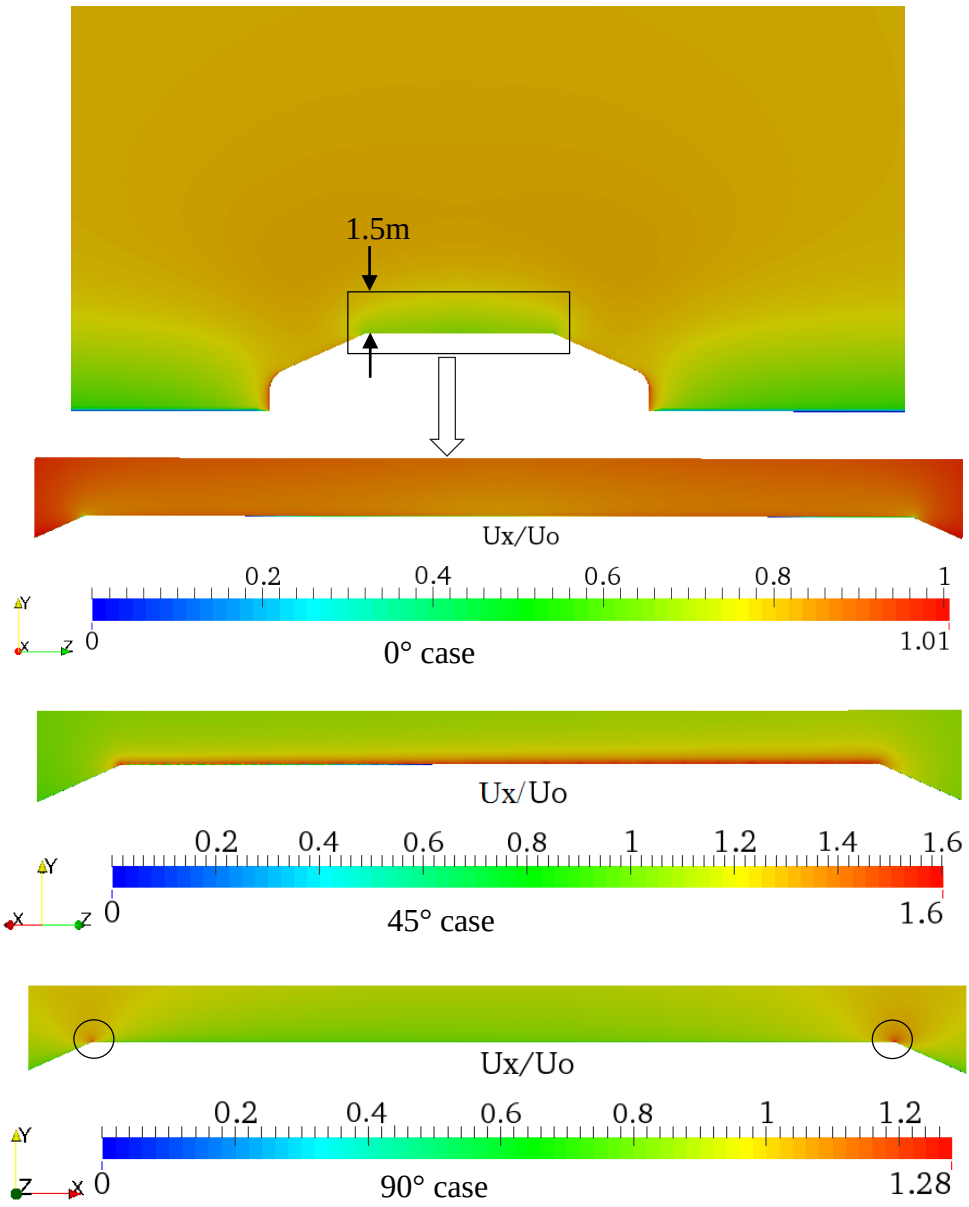

Figure 5.12: Velocity fields along the gable of the roof for all wind directions

For more detailed flow fields along the gable, a central section of the building was taken along the gable of the roof for all cases. Note that the x axis is the wind direction and $z = 0$ is at the centre point of the building for all cases. The velocity fields are shown for the indicated region (top picture) in Figure 5.12. The colour scales are different from figure to figure. The maximum

velocity was $1.28U_0$ for the 90° case. It should be noted that the 90° wind flow is parallel to the turbine axis and therefore would produce negligible power. It was included for consistency. In all cases, the maximum velocity was higher in the circled regions than elsewhere above the gable (including the location of the turbine).

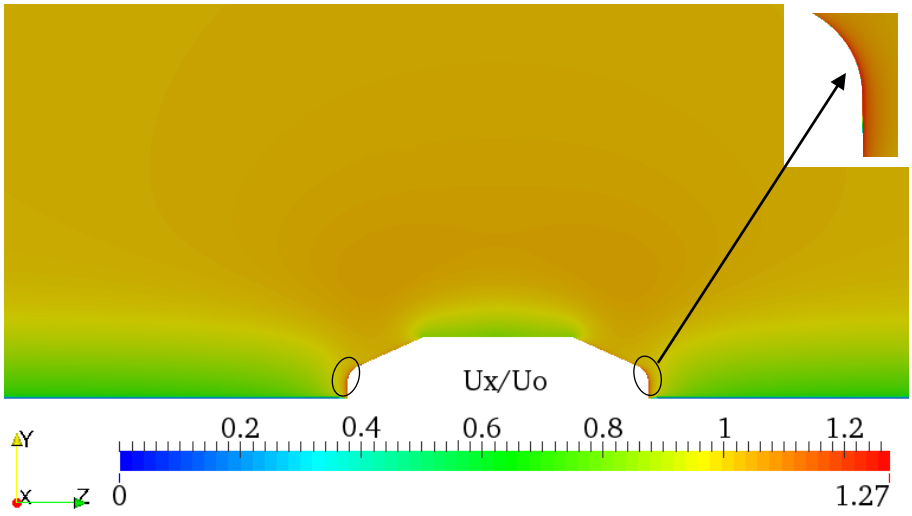

Figure 5.13: Velocity field around the building for 0° case

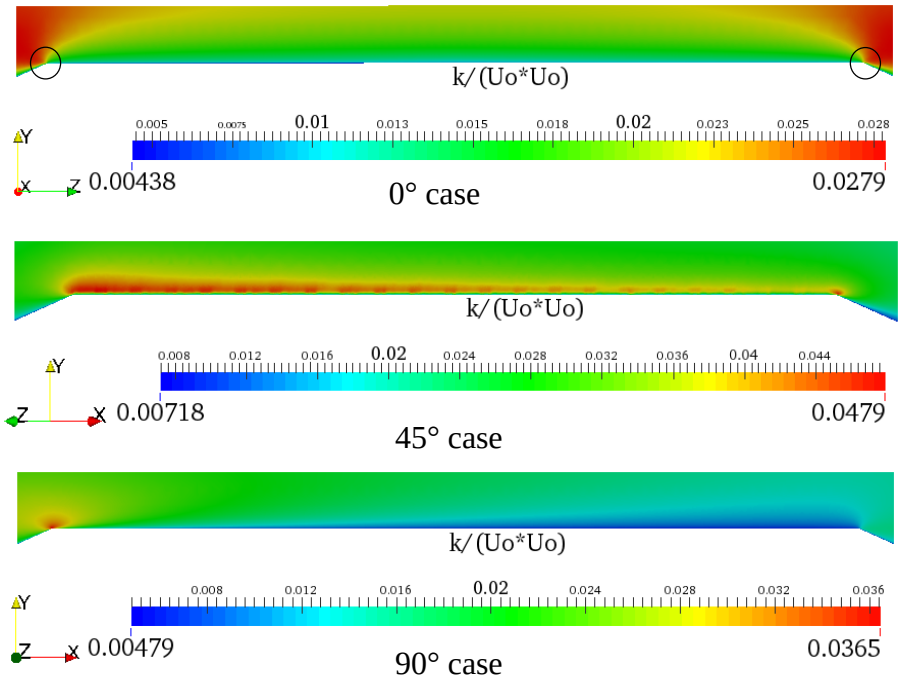

Figure 5.14: Turbulent kinetic energy contour along the gable of the roof for all cases

For the 0° case, the maximum velocity was $1.27U_0$, occurring in the region indicated by the oval in Figure 5.13. This is probably due to the lateral straining of the flow and acceleration around the building (Figure 5.6). Figure 5.14 shows the turbulent kinetic energy contours ($\frac{k}{U_0^2}$) for the region indicated by the rectangle in Figure 5.12. k was also higher in the circled region than elsewhere. However, the key result is the increase in U for 0º degree case over the gable. The other flow directions (45º and 90º) would produce less turbine power. More details of the flow over the gable are shown in Figure 5.15. The velocity profiles plotted at different height (0.1 m, 0.3 m, 0.5 m and 1m) from the gable. Those heights cover the range of blade radius of most wind turbines (Figure 5.1 (Right)). The velocity was significantly higher at the beginning and end (around 0 and 22m) of the gable than elsewhere. But those locations also had higher turbulence (Figure 5.14), which can reduce wind turbine performance. The locations indicated by green circles in Figure 5.15 are the positions of maximum energy content in the wind.

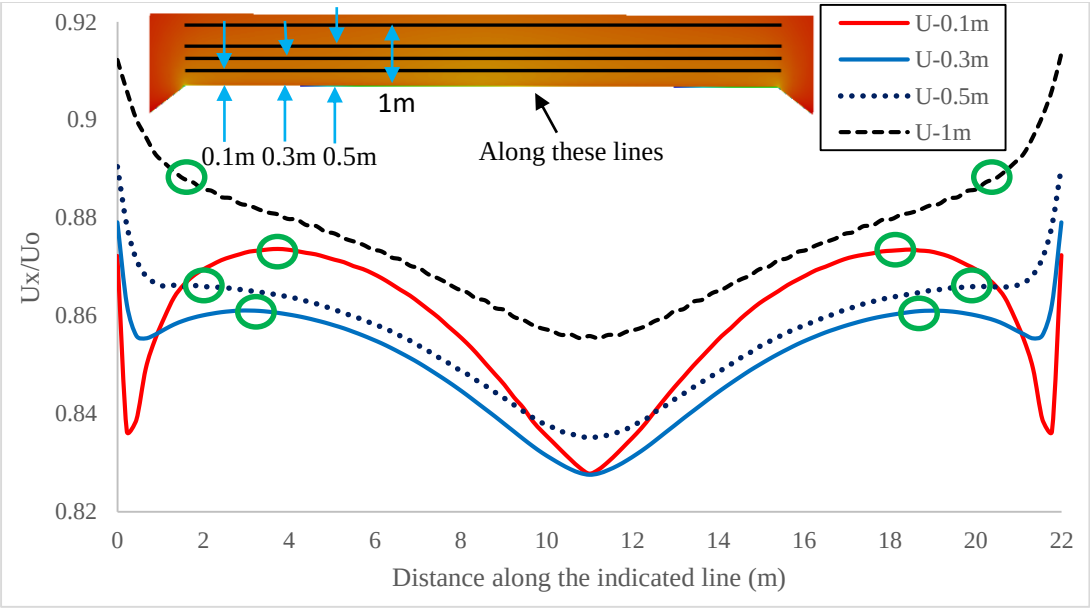

Figure 5.15: Velocity profiles above the gable at different height (0º wind flow)

In addition, C_p is plotted for all wind directions in Figure 5.16. In these C_p plots, C_p varies smoothly except near the roof edge and corners. The maximum C_p was 0.863 at 0.26H for 0º wind flow.

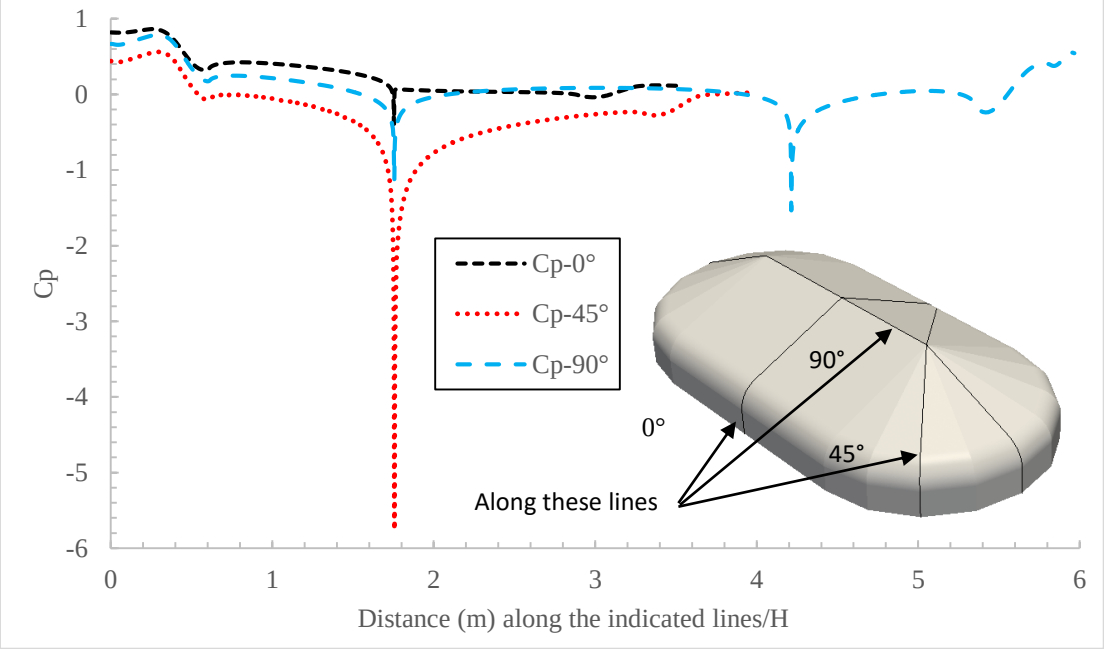

Figure 5.16: Pressure coefficients over the Sprung building for all wind directions [Parallel to the wind direction]

5.3.1 Comparison between the Present results and Experimental data

A Sprung employee measured the wind speed using anemometers at the south and west pole locations defined in Figure 5.17. The heights of the south and west pole anemometers are H and 1.21H from the ground. And the horizontal distances are same (10.70m) from the centre of the wind turbine for both anemometers. They also measured the wind directions for different times in a day. The wind directions vary from $-4°\ to\ 56.5°$ shown in Figure 5.18. The geometry of this

experimental building is somewhat different from the simulated building geometry (Figure 5.17 (right)), but the height (H) and length (L) are the same for both buildings.

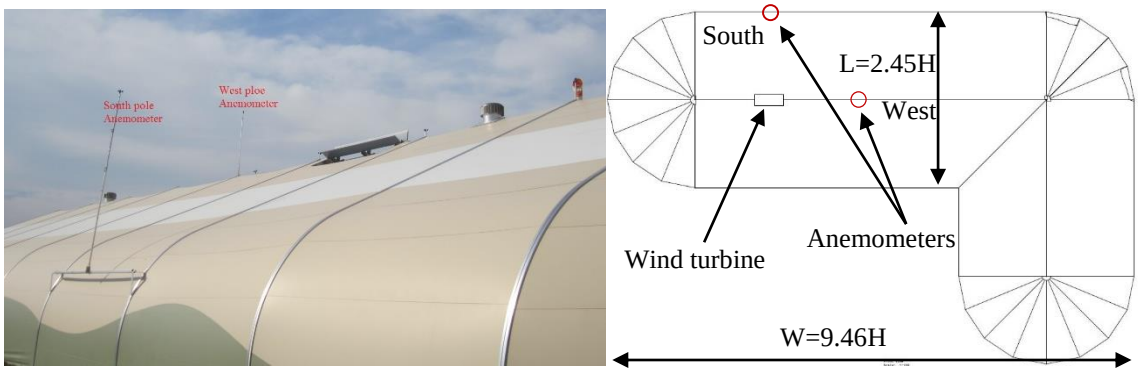

Figure 5.17: Locations of the anemometer (left) and the top view of the experimental building (right) [Photo provided by Ron Hockin, Sprung Instant Structures Ltd.]

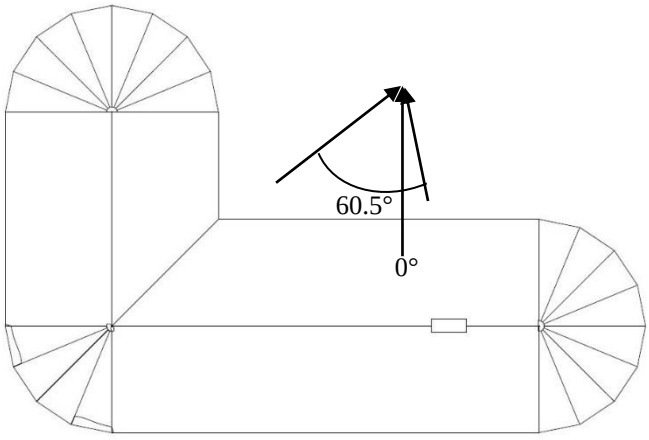

Figure 5.18: Measured wind directions (varies from $-4°\ to\ 56.5°$)

From the field data, the ratio of speeds for the south and west locations $\left(\frac{U_{south}}{U_{west}}\right)$ was calculated and plotted with respect to wind directions. For those locations, the numerical results were extracted and plotted for three wind directions (0°, 45° and 90°). Figure 5.19 shows the comparison between the present results and the experimental data. The velocity fluctuation, which is the difference between the measured velocity and averaged velocity

(19.33 and 15.19 m/s for west and south), is plotted with respect to time in Figure 5.20. The simulated results show approximately the average of the field data.

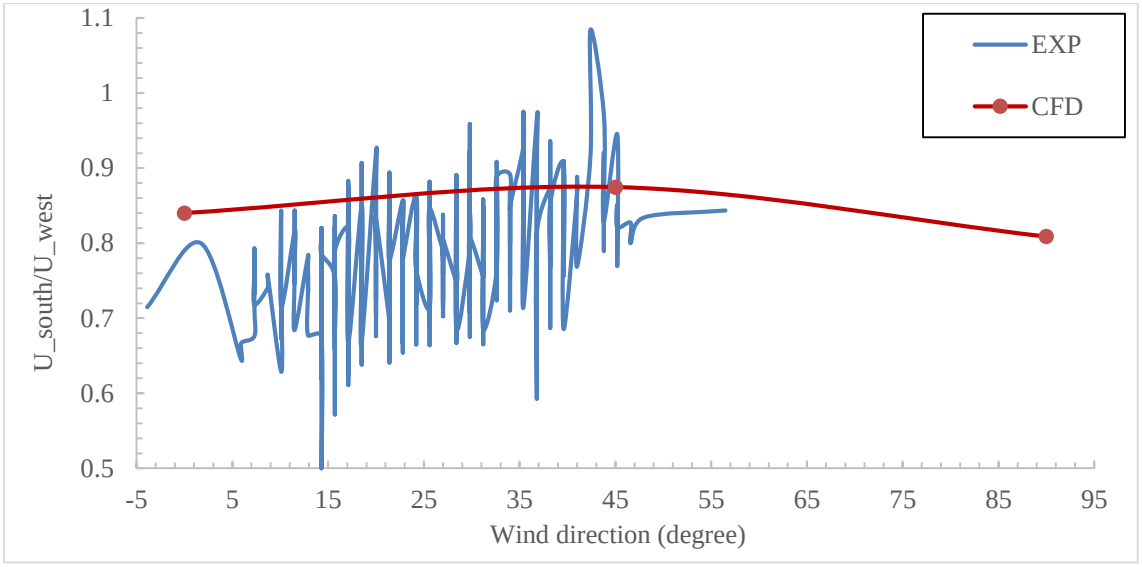

Figure 5.19: Comparison between the present results and field data

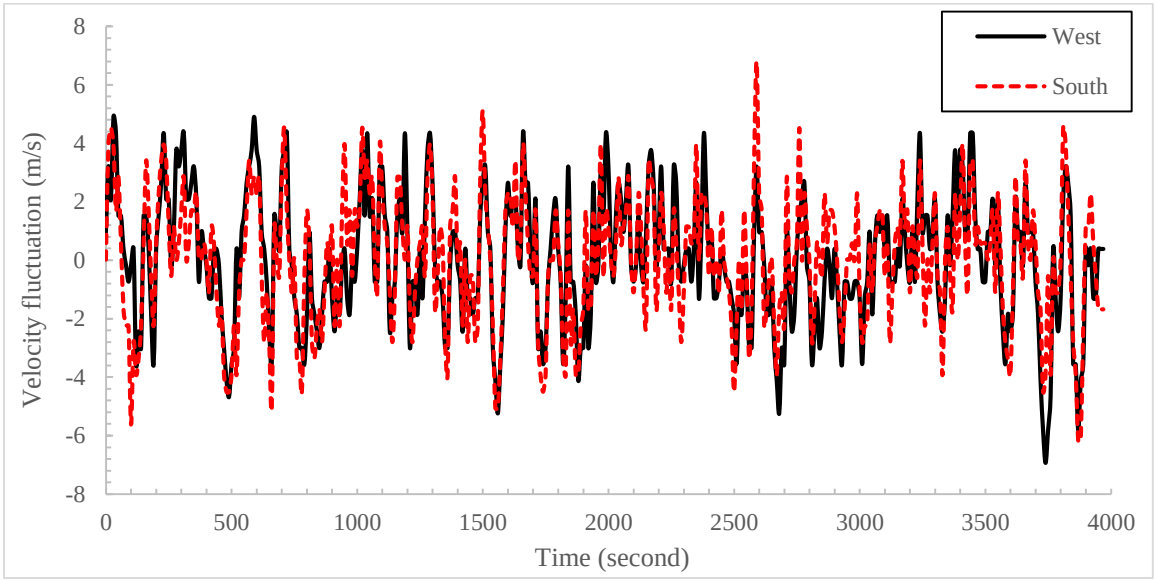

Figure 5.20: Time series of velocity fluctuation at west and south locations

The turbulence intensity was calculated as

$$\text{Turbulence intensity}, I = 100 \times \frac{u'_{rms}}{U}(\%) \tag{5.1}$$

where U is the mean (or averaged) velocity and u'_{rms} is the root mean square velocity fluctuation. I was 11.45% and 14.53% for the west and south locations. The Boussinesq approximation is given by

$$-\rho\overline{u'_\iota u'_\jmath} = 2\mu_t S_{ij} - \frac{2\rho k\delta_{ij}}{3} \tag{5.2}$$

where δ_{ij} is the kronecker delta. It should be noted that the Boussinesq approximation is used to calculate the Reynolds stress $\left(\rho\overline{u'_\iota u'_\jmath}\right)$ in the standard $k-\varepsilon$ model. To calculate the turbulence intensity, the equation (5.2) can be rewritten for x-component of k:

$$-\overline{u'^2} = 2C_\mu \frac{k^2}{\varepsilon}\frac{\partial U_x}{\partial x} - \frac{2k}{3} \tag{5.3}$$

where $\mu_t = \rho C_\mu \frac{k^2}{\varepsilon}$ for the standard $k-\varepsilon$ model and $\delta_{ij} = 1$ for $i = j$. $I = (100 \times u')/U$ % was 12.53% and 14.74% at those locations from the CFD results. These CFD results are very close to the calculated values from the field data. Therefore, it can be concluded that the simulated results were very close in comparison with the field data.

5.4 Conclusion

In this research, the wind flow over the Sprung building was simulated using the standard $k-\varepsilon$ turbulence model for different wind directions. A similar CFD model to that used for the Karoleena building simulation was used. The goal of these simulations was to predict the flow fields for analysis of a transverse axis wind turbine mounted along the gable. Firstly, three cases were created to check the mesh independence. Then, the flow over the building investigated for different wind directions defined in Figure 5.5.

The velocity fields and turbulent kinetic energy were computed and presented for three flow directions (Figures 5.9 to 5.14). The maximum velocities near the roof edges were $1.27U_0$ for 0° case, $1.42U_0$ for 45° case and $1.28U_0$ for 90° case. Figure 5.15 shows the increase in U over the gable. The present results were also compared to the field data in section 5.3.1. Those results were consistent with the field data. The velocity field over the gable was predicted for future analysis of the wind turbine performance (Figure 5.15). The locations indicated by the green circles in Figure 5.15 have the maximum turbine power density. In addition, the streamlines (Figures 5.6 to 5.8) and pressure coefficient (Figure 5.16) were calculated for different wind directions.

Chapter Six: **CONCLUSIONS AND RECOMMENDATIONS**

This research had two main aims: one is to predict the air flow to minimize the cost of installing the roof-mounted PV modules for the Karoleena building and second is to predict the flow fields along the gable of the roof of the Sprung building for future analysis of the performance of a wind turbine mounted along the gable (Figure 5.1). The extreme wind loads on those buildings were simulated and presented for different wind directions. The standard $k-\varepsilon$ turbulence model was chosen to calculate the flow fields around buildings in this research. This model was selected because of its simplicity and its common use in wind assessment. OpenFOAM was used because it is a free, open source CFD software. It has an extensive toolbox to solve complex fluid flows including turbulence, heat transfer etc.

First, a number of the literature and CFD guidelines were reviewed to estimate on the approximation of the flow over the building in chapter two. The numerical procedure, RANS equations, the standard $k-\varepsilon$ turbulence model, boundary and initial conditions were explained in detail in chapter three. To validate and prepare a CFD model for new simulations, the flow over a cube (Silsoe cube) building was simulated and presented. The effects of boundaries, blockage ratio and mesh independence (including the Grid Convergence Index calculation) were investigated to check the accuracy of the simulations. Then, the present results were compared with the previous works and other CFD results and shown to be in good agreement (Figures 3.12 and 3.13). The maximum pressure coefficient was at $0.8H$, which agreed well with the measured range of the previous works. On the roof, the minimum pressure coefficient was -1.32 (Figure 3.14), which also agreed well with the previous works. Therefore, the present investigation of the flow over the

cube building was consistent in comparison with the previous experimental data and other CFD results. In addition, the turbulent kinetic energy contour was determined with a central section of the cube building parallel to the wind direction to provide more information.

To investigate the flow over the Karoleena building (Figure 4.1), a similar CFD model to that for the cube building simulation was applied. For checking the mesh independence, three cases were simulated and compared to each other and found in good agreement. Those comparisons were indicated the independence of the results on the grid. Then, the selected cases were simulated and presented for three wind directions (Figure 4.5). The streamlines, pressure coefficients and contours, velocity profiles and turbulent kinetic energy over the Karoleena building were explained in detail (Figures 4.7 to 4.18). Also, the present results were compared with the NBCC (2010) wind provision for general mono-slope roof building (Table 4.2). The present values (area-averaged pressure coefficients) had similar trends to the NBCC (2010) specifications, but were approximately 30% lower in magnitude. To find the minimum wind load (minimum cost) regions on the roof, the roof was divided into several possible locations (Figure 4.22). The area-averaged pressure coefficient was calculated for those locations (Table 4.3). By examining the suction $C_{p(avg)}$ for all wind directions, the best regions were locations 7, 8 and 9, where $C_{p(avg)}$ was close to -0.30. For three locations (1, 2 and 3), a large negative $C_{p(avg)}$ was found (more negative than -0.60). These regions should be avoided when installing PV modules on the roof. So, this research recommended that the locations (7, 8 and 9) have the minimum wind load. In this work, the flow over the building was found to be highly dependent on the building orientation and geometry.

For the Sprung building simulation, the CFD model of the Karoleena building simulation was used to predict the flow fields along the gable of the roof. Three cases were simulated and compared to each other for checking the mesh independence. There were very little differences which demonstrates the independence of the results on the grid. Then, the flow over the Sprung building was investigated for three different wind directions. Along the gable of the roof, the velocity profiles, velocity fields and turbulent kinetic energy were examined (Figures 5.6 to 5.13). The maximum velocity was approximately $1.27U_0$ for 0° case, $1.42U_0$ for 45° case and $1.28U_0$ for 90° case. The velocity profiles above the gable were shown in Figure 5.15. The simulated results were also compared with the field data. Those results were accurate and consistent with the field data. So, the velocity fields over the gable were accurately predicted for future analysis of the wind turbine performance. It can be recommended that the locations indicated by green circles in Figure 5.15 have the maximum wind energy content. The flow over the building had also highly dependent on the building geometry and flow direction as for the Karoleena building. Some differences were found in the flow fields particularly in the regions highlighted by the oval in Figures 5.13. To find out more detail about those differences, further investigation is required.

REFERENCES

ABC (2010). Alberta Building Code 2010. National Research Council, Ottawa, Canada.

Abohela, Islam., Hamza, Neveen and Dudek, Steven (2013). Effect of roof shape, wind direction, building height and urban configuration on the energy yield and positioning of roof mounted wind turbines. Journal of Renewable Energy, 50, 1106-1118.

Aly, A. M. and Bitsuamlak, G. (2013). Aerodynamic loads on solar panels. Structures Congress, London, ON, Canada, 1555-1564.

Aly, A. M. and Bitsuamlak, G. (2014). Wind-Induced Pressures on Solar Panels Mounted on Residential Homes. Journal of Architectural Engineering, 20(1), 04013003-04013012.

Aly, Aly Mousaad., Bksuamlak, Girma and Crepel, Vincent (2013). Wind loads on ground-mounted solar panels: A multi-scale computational and experimental study. 12th Americas Conference on Wind Engineering, Seattle, Washington, United States.

Baetke, Frank., Werner, Heinrich and Wengle, Hans (1990). Numerical simulation of turbulent flow over surface-mounted obstacles with sharp edges and corners. Journal of Wind Engineering and Industrial Aerodynamics, 35(1), 129-147.

Blocken, Bert., Stathopoulos, Ted., Carmeliet, Jan and Hensen, Jan L. M. (2011). Application of computational fluid dynamics in building performance simulation for the outdoor environment: An overview. Journal of Building Performance Simulation, 4(2), 157-184.

Castro, I. P. and Robins, A. G. (1977). The flow around a surface-mounted cube in uniform and turbulent streams. Journal of Fluid Mechanics, 79(2), 307-335.

Cermak, J. E. (1975). Applications of fluid mechanics to wind engineering - a freeman scholar lecture. Journal of Fluids Engineering, Transactions of the ASME, 97 Ser I(1), 9-38.

Cook, N. J. (1985). The designer's guide to wind loading of building structures. [Garston, Watford]; London; Boston, Building Research Establishment, Dept. of the Environment ; Butterworths.

Cui, Bo (2007). Wind effects on monosloped and sawtooth roofs. PhD's Dissertation, Clemson University, USA.

Frank, W. (1996). Three-dimensional numerical calculation of the turbulent flow around a sharp-edged body by means of large-eddy-simulation. Journal of Wind Engineering and Industrial Aerodynamics, 65(1-3), 415-424.

Franke, J., Hellsten, A., Schlünzen, H and Carissimo, B (2007). Best Practice Guideline for the CFD Simulation of flows in the Urban Environment. COST Action 732. COST office, 52 pp.

Franke, J., Sturm, M and Kalmbach, C (2012). Validation of OpenFOAM 1.6.x with the German VDI guideline for obstacle resolving micro-scale models. Journal of Wind Engineering and Industrial Aerodynamics, 104-106, 350-359.

Franke, J., C. Hirsch, A.G. Jensen, H.W. Krüs, M. Schatzmann, P.S. Westbury, S.D. and Miles, J.A. Wisse, and N.G. Wright (2002). Recommendations on the use of CFD in wind engineering. In: COST Action C14, Impact of wind and storm on city life built environment, von Karman Institute, pp C1.1–C1.11.

Fromm, J. E. and Harlow, F. H. (1963). Numerical solution of the problem of vortex street development. Physics of Fluids, 6(7), 975-982.

Gadilhe, A., Janvier, L and Barnaud, G (1993). Numerical and experimental modelling of the three-dimensional turbulent wind flow through an urban square. Journal of Wind Engineering and Industrial Aerodynamics, 46-47, 755-763.

Hanson, T., Summers, D. M and Wilson, C. B (1986). Three-dimensional simulation of wind flow around buildings. International Journal for Numerical Methods in Fluids, 6(3), 113-127.

Jing, Xiao-Kun and Li, Yuan-qi (2013). Wind Tunnel Tests for Wind Pressure Distribution on Gable Roof Buildings. The ScientificWorld Journal, 2013(11).

Jones, W. P. and Launder, B. E. (1972). The prediction of laminarization with a two-equation model of turbulence. International Journal of Heat and Mass Transfer, 15(2), 301-314.

Kopp, G. A., Farquhar, S. and Morrison, M. J. (2012). Aerodynamic mechanisms for wind loads on tilted, roof-mounted, solar arrays. Wind Engineering and Industrial Aerodynamics, 111, 40-52.

Kopp, G. A., Surry, D. and Chen, K. (2002). Wind loads on a solar array. Wind and Structures, An International Journal, 5(5), 393-406.

Launder, B. E. and Spalding, D. B. (1974). The numerical computation of turbulent flows. Computer Methods in Applied Mechanics and Engineering, 3(2), 269-289.

Martinuzzi, R. and Tropea, C. (1993). The flow around surface-mounted, prismatic obstacles placed in a fully developed channel flow. Transactions of the ASME. Journal of Fluids Engineering, 115(1), 85-92.

Ming, Jie., Liu, Zhizhang and Zhang, Qingzhu (2010). Solar photovoltaic panels wind load testing and analysis. Mechanic Automation and Control Engineering, MACE2010, Wuhan, China, IEEE Computer Society, 1632-1635.

Murakami, Shuzo and Mochida, Akashi (1988). 3-D numerical simulation of airflow around a cubic model by means of the k-ϵ model. Journal of Wind Engineering and Industrial Aerodynamics, 31(2–3), 283-303.

NBCC (2010). National Building Code of Canada 2010. National Research Council, Ottawa, Canada.

OpenFOAM (2014). OpenFOAM CFD UserGuide.

Patankar, S. V., Spalding, D. B. and Pratap, V. S. (1974). Prediction of laminar flow and heat transfer in helically coiled pipes. Journal of Fluid Mechanics, 62(Part 3), 539-551.

Patankar, S.V. (1980). Numerical Heat Transfer and Fluid Flow. Textbook.

Paterson, D. A. and Apelt, C. J. (1989). Simulation of wind flow around three-dimensional buildings. Building and Environment, 24(1), 39-50.

Rakai, A and Kristóf, D. G. (2010). CFD Simulation of Flow over a Mock Urban Setting. 5th OpenFOAM Workshop, Chalmers, Gothenburg, Sweden.

Richards, P. J., Hoxey, R. P. and Short, L. J. (2000). Spectral models for the neutral atmospheric surface layer. Journal of Wind Engineering and Industrial Aerodynamics, 87(Issues 2–3), 167–185.

Richards, P. J. and Hoxey, R. P. (1993). Appropriate boundary conditions for computational wind engineering models using the k-e turbulence model. Proceedings of the 1st International Symposium on Computational Wind Engineering (CWE 92), 08/21 - 23/92, Tokyo, Japan, Publ by Elsevier Science Publishers B.V., 145-145.

Richards, P. J. and Hoxey, R. P. (2001). Wind pressures on a 6 m cube. Journal of Wind Engineering and Industrial Aerodynamics, 89(14-15), 1553-1564.

Richards, P. J. and Hoxey, R. P. (2006). Flow reattachment on the roof of a 6 m cube. Journal of Wind Engineering and Industrial Aerodynamics, 94(2), 77-99.

Richardson, Lewis F. and Gaunt, J. Arthur (1927). The Deferred Approach to the Limit. Part I. Single Lattice. Part II. Interpenetrating Lattices. Philosophical Transactions of the Royal

Society of London A: Mathematical, Physical and Engineering Sciences, 226(636-646), 299-361.

Roache, P. J. (1994). Perspective: a method for uniform reporting of grid refinement studies. Transactions of the ASME. Journal of Fluids Engineering, 116(3), 405-413.

Rodi, W. (1997). Comparison of LES and RANS calculations of the flow around bluff bodies. Journal of Wind Engineering and Industrial Aerodynamics, 69-71, 55-75.

Shademan, Mehrdad and Hangan, Horia (2009). Wind loading on solar panels at different inclination angles. 11th Americas Conference on Wind Engineering, June 22, 2009 - June 26, 2009, San Juan, Puerto Rico.

Sousa, J. M. M. and Pereira, J. C. F. (2004). DPIV study of the effect of a gable roof on the flow structure around a surface-mounted cubic obstacle. Experiments in Fluids, 37(3), 409-418.

Spalart, P. R. and Allmaras, S. R. (1994). One-equation turbulence model for aerodynamic flows. Recherche aerospatiale(1), 5-21.

Stathopoulos, T., Eleni and Zisis, Ioannis (2013). Wind loads on solar collectors and PV panels on roofs, Pittsburgh, PA, United States, American Society of Civil Engineers (ASCE), 1545-1554.

Stathopoulos, T. and Mohammadian, A. R. (1985). Wind loads on low buildings with mono-sloped roofs. Journal of Wind Engineering and Industrial Aerodynamics, 23(1-3), 81-97.

Tominaga, Yoshihide., Mochida, Akashi., Yoshie, Ryuichiro., Kataoka, Hiroto., Nozu, Tsuyoshi., Yoshikawa, Masaru and Shirasawa, Taichi (2008). AIJ guidelines for practical applications of CFD to pedestrian wind environment around buildings. Journal of Wind Engineering and Industrial Aerodynamics, 96(10-11), 1749-1761.

Versteeg, H K and Malalasekera, W (2007). An Introduction to Computational Fluid Dynamics. Textbook.

WINEUR (2007). Wind Energy Integration in the Urban Environment. Report on Resource Assessment. European Commission.

Wood, D H (2011). Small Wind Turbines Analysis, Design, and Application. Springer, London.

Zhou, Ying and Zhang, Qilin (2010). Numerical simulation of wind pressure distribution on structure roofs with suspension solar panels, Guangzhou, China, Trans Tech Publications, 163-167, 3943-3946.

Zhou, Yongsheng (1995). Numerical evaluation of wind effects on buildings. PhD Dissertation, Concordia University, Canada.